The design and optimization of a multi-reflection time-of-flight mass-spectrometer for Barium tagging with nEXO and optimization of the ^{137}Xe veto with EXO-200

Kevin Murray

Department of Physics
McGill University, Montreal

A thesis submitted in partial fulfillment of the requirements for the degree of
Master of Science

Abstract

The mechanism by which neutrino masses arise is still unknown, yet it is clear from neutrino oscillation experiments that they do have mass. One possible solution is through the observation of neutrinoless double beta decay ($0\nu\beta\beta$), a lepton number violating process that is beyond the current Standard Model. The existence of this decay would show that the neutrino is a Majorana particle, meaning that it is its own antiparticle. This would provide a natural explanation for the smallness of the neutrino masses, as well as a measurement of the effective Majorana neutrino mass. The EXO collaboration is searching for $0\nu\beta\beta$ decay with the ^{136}Xe isotope deployed in a time projection chamber. In the first part of this work, a data analysis cut has been developed and implemented to reduce the background created by ^{137}Xe decay in the EXO-200 experiment, which is currently in operation. The cut is called the ^{137}Xe veto and has a rejection efficiency of $21 \pm 4\%$ for Phase-I data and $21 \pm 5\%$ for Phase-II data. In the second part of this work, a multiple-reflection time-of-flight mass-spectrometer has been designed and simulated for use in Ba-tagging. The Ba-tagging project seeks to allow for a background free measurement of double beta decays, by extracting and identifying the daughter Ba ions they produce. This setup will be used in future tonne-scale experiments such as nEXO, where the role of the mass-spectrometer will be to conduct systematic studies of the ion extraction technique, and provide further identification of the Ba ion. Simulations show that the device can achieve a mass resolving-power of $m/\Delta m \approx 70000$, which is sufficient for isobaric separation. Moreover it can operate in a fast turn switching mode, which makes it suitable for broad-range mass spectroscopy.

Résumé

Le mécanisme par lequel la masse des neutrinos survient est encore inconnu. Pourtant, à partir des expériences d'oscillation de neutrinos, il est clair qu'ils en ont une. Une solution envisageable est l'observation de la double désintégration bêta sans émission de neutrino ($0\nu\beta\beta$), un processus au-delà du modèle standard de la physique des particules actuel qui viole la conservation du nombre leptonique. L'existence de cette désintégration montrerait que le neutrino est une particule de Majorana, c'est-à-dire qu'elle est sa propre antiparticule. Cela fournirait une explication naturelle de leurs masse relativement petite, ainsi qu'une mesure de leurs masse effective. La collaboration EXO recherche la désintégration $0\nu\beta\beta$ avec l'isotope ^{136}Xe déployé dans une chambre à projection temporelle. Dans la première partie de ce travail, une coupe d'analyse de données est développée et mise en oeuvre pour réduire le bruit de fond créé par la désintégration du ^{137}Xe dans l'expérience EXO-200, qui est actuellement en cours. La coupe, appelée le ^{137}Xe veto, a une efficacité de rejet de 21±4% pour les données Phase-I et de 21±5% pour les données Phase-II. Dans la deuxième partie de ce travail, un spectromètre de masse à temps de vol multi-réflecteur est conçu et simulé pour être utilisé dans le Ba-tagging. Le projet de Ba-tagging vise à permettre une mesure sans bruit de fond des doubles désintégrations bêta, en extrayant et en identifiant les ions filles du Ba qu'ils produisent. Cette configuration sera utilisée dans de futurs expériences avec une quantitée de ^{136}Xe à l'échelle de tonnes, telles que nEXO, où le rôle du spectrométre de masse sera de mener des études systématiques sur la technique d'extraction d'ions et de raffiner l'identification de l'ion de Ba. Les simulations montrent que le spectromètre peut atteindre une résolution de masse de $m/\Delta m \approx 70000$, ce qui est suffisant pour la séparation d'isobares. De plus, le spectromètre peut fonctionner dans un mode de commutation à virage rapide, ce qui le rend convenable pour un vaste éventail de spectroscopie de masse.

Acknowledgements

First and foremost I would like to thank my supervisor, Dr. Thomas Brunner, without whom none of this work would have been possible. Thanks also to Dr. Caio Licciardi and Dr. Joshua Albert, for their vital role in developing the ^{137}Xe veto, and graciously teaching me data analysis with EXO-200. Thanks to the EXO-200 and nEXO collaborations, through which I have made many friends and contacts. They are a welcoming and helpful community of talented physicists to which I am forever indebted.

I am exceedingly grateful to the TITAN group at TRIUMF, to Yang Lan for supplying important simulation data from the Linear Paul Trap, and to Dr. Moritz Pascal Reiter for important discussions on mass spectrometry. Thanks to Dr. Brad Schultz for all of his invaluable help with the MR TOF design. Thanks also to Dr. Yuta Ito, a postdoc here at McGill, for all of his advice and guidance on the MR TOF. His perpetual enthusiasm is highly contagious. A thanks to Thanh Nguyen, an undergraduate student in our lab, who translated the abstract.

It would be remiss of me not to mention Pascal Bourseguin, the McGill Physics Machine Shop Manager. He never fails to go into gruesome detail on how even the most innocuous machining task could result in serious injury or even death. As a result, I have a healthy respect for the machine shop equipment. His endless patience and willingness to help is greatly appreciated.

Dedicated to my dearest family and friends. My gratitude to you is ineffable.

Preface and Contributions of Authors

All chapters in this thesis have been written by me, the main author.

EXO-200 is a collaborative effort with many people contributing to the maintenance of the detector, calibration and data analysis. I have also contributed by taking on-site maintenance shifts, as well as remote-monitoring shifts.

In Chapter 4, the code used to generate figs. 4.8 and 4.10 was written by Dr. Caio Licciardi, who also helped write the ^{137}Xe software veto scripts. I wrote code that tested the veto algorithm for various parameters. Dr. Caio Licciardi committed the veto algorithm to the EXO analysis software packages. The framework of the algorithm was largely developed by Dr. Joshua Albert and Dr. Caio Licciardi. Studies of the veto rejection efficiency, loss in livetime, increase in sensitivity, and systematic uncertainty were conducted by me.

In Chapter 5, the ion source data used in the MR TOF simulations was supplied by Yang Lan at TRIUMF, as well as the code to generate fig. 5.9. I have created all of the MR TOF drawings, SIMION simulations, and SIMION user scripts. Studies of the MR TOF's mass resolution and mass selector efficacy were conducted by me. The MR TOF drawings are based on a Greifswald design which has been modified by Notre Dame.

Contents

Chapter 1

Introduction

Empirical evidence for neutrino oscillation has confirmed that neutrino flavours are in fact linear combinations of nonzero mass eigenstates [1, 2]. This observation necessitates a modification to the current Standard Model (SM) description of neutrinos [3]. One possible extension to the SM is the inclusion of additional right-handed neutrino fields, which introduces a light and heavy neutrino for each of the three flavours via the seesaw mechanism. This would offer a natural explanation for the smallness of the neutrino masses, relative to other leptons. However, this mechanism requires the violation of lepton number conservation and posits the notion that neutrinos are Majorana particles [4]. This would mean that the neutrino is its own antiparticle, and this could be shown through the observation of neutrinoless double beta decay ($0\nu\beta\beta$), a lepton number violating process. This decay, if it exists, is extremely rare, and can only be observed in an isotope where single beta decay is energetically forbidden or otherwise suppressed. It can occur when the two neutrinos produced by double beta decay ($\beta\beta$) annihilate each other, also known as light Majorana neutrino exchange. If this type of exchange is the dominant contribution to $0\nu\beta\beta$ decay, a measurement of the decay rate would also provide a measurement of the effective Majorana neutrino mass [5]. Chapter 2 explores the underlying theory of massive neutrinos and $0\nu\beta\beta$ decay in greater detail.

The Enriched Xenon Observatory (EXO) collaboration seeks to observe $0\nu\beta\beta$ decay using the isotope ^{136}Xe. The EXO-200 experiment uses $\sim$175 kg of Xe in a time projection chamber (TPC), and is currently in operation at the Waste Isolation Pilot Plant (WIPP) in New Mexico [6]. The nEXO project is a planned multi-tonne scale TPC, that will be used to dramatically enhance the sensitivity to $0\nu\beta\beta$ decay [7]. The EXO-200 experiment is described at length in Chapter 3, along with the prospects for nEXO.

A key ingredient to measuring such a decay is lowering the backgrounds in the signal region as much as possible. This work explores two vastly different techniques to accomplish this. The first is in data analysis, discussed in Chapter 4, where we have developed techniques of identifying a particular background to the signal and mitigating its effect. This is done with EXO-200 data, where we attempt to reduce the background created by ^{137}Xe decay. The identification of neutron capture on ^{136}Xe allows the ^{137}Xe atom, which has a half-life of 3.82 min [8], to be localized to a sub-volume of the TPC. This sub-volume is removed from the analysis for an appropriate length of time such that the ^{137}Xe decay is ignored.

The second is in a project called Ba-tagging, where the daughter nucleus of $\beta\beta$ decay is physically extracted from the active volume and identified. This method of tagging can be combined with a corresponding detector signal for an unambiguous measurement of $\beta\beta$ decay. For the Ba-tagging project, I have designed and simulated a multiple-reflection time-of-flight mass-spectrometer (MR TOF). Chapter 5 gives an overview of mass spectrometry, the MR TOF design, and the methods employed for optimization of the operational voltages. The MR TOF will be used to conduct systematic studies on the ion extraction techniques used to retrieve the Ba ion from the TPC, as well as provide further identification of the Ba ion. The design is based on an existing MR TOF used for ISOLTRAP at ISOLDE/CERN, which is well known for achieving unprecedented mass-resolving powers ($m/\Delta m > 1 \times 10^5$) [9].

Chapter 2

Concerning Neutrinos

The neutrino was originally proposed in 1930 by Wolfgang Pauli to explain the continuous beta decay energy spectrum [10]. He called it the neutron since it appeared electrically neutral and it was originally thought to posses a mass similar to that of an electron.

This idea was taken up by Enrico Fermi, who established the more familiar theory of beta decay in 1934 [11]. He renamed the neutron the neutrino, adding the diminutive Italian suffix -ino, since its rest mass actually appeared to be far smaller than that of the electron. It was so small in fact, that it was thought to be zero. By this time, nuclei were thought of as bound states of neutrons and protons, in which the neutron could decay into a proton, electron and antineutrino

$$n \rightarrow p + e^{-} + \bar{\nu}_e \, . \tag{2.1}$$

Neutrinos were first detected directly in 1956 by the Cowan-Reines neutrino experiment [12]. Cowan and Reines set up two tanks of water next to a nuclear reactor, allowing them to measure the antineutrino flux through inverse beta decay. In 1962, it was shown that there was more than one type of neutrino flavour through detection of the muon neutrino [13]. Energetic protons from a particle accelerator created showers of pi mesons, which decayed into muons and muon neutrinos, the latter of which was subsequently detected with a spark chamber. When the tau lepton was discovered in 1975 [14], it exhibited the same continuous energy spectrum as the electron, hence it was immediately expected to be accompanied by an associated tau neutrino as well. The tau neutrino was detected directly in 2000 at Fermilab with the Tevatron accelerator [15]. Thus it was established that there are three neutrino flavours.

Measurement of the neutrino flux from the sun presented a baffling conundrum, as it was found to be much lower than expected. This came to be known as the solar neutrino problem, and was first discovered in the mid-1960s by the Homestake experiment, which used a chlorine-based detector [16]. The resolution of this discrepancy required a modification to the then accepted Standard Model. Neutrinos aren't massless as previously assumed, but rather, they are mixtures of mass eigenstates. As shall be shown in the following section, this allows a neutrino to change its flavour eigenstate during propagation, in a process known as neutrino oscillation. Solar neutrino oscillation was discovered in 2001 by the Sudbury Neutrino Observatory (SNO) [1], resolving the solar neutrino problem. This was compounded by the earlier discovery of atmospheric neutrino oscillation by Super-Kamiokande in 1998 [2]. As a result, the 2015 Nobel Prize for Physics was awarded to Arthur McDonald and Takaaki Kajita, for the discovery of neutrino oscillation, and confirming that neutrinos have mass.

2.1 Neutrino Oscillation

Neutrino oscillation is the process whereby a neutrino, created with a particular flavor eigenstate, is later detected with a different flavor eigenstate. This process of neutrino mixing is modeled with a unitary transformation U between the flavor and mass eigenstates

$$|\nu_\alpha\rangle = \sum_j U^*_{\alpha j} |\nu_i\rangle \tag{2.2}$$

$$|\nu_j\rangle = \sum_\alpha U_{\alpha j} |\nu_\alpha\rangle \ . \tag{2.3}$$

Where $|\nu_\alpha\rangle$ and $|\nu_i\rangle$ are definite flavor and mass eigenstates, respectively, with α = e (electron), μ (muon), τ (tau) and m_i, $i = 1,2,3$. The mixing matrix U is called the Pontecorvo-Maki-Nakagawa-Sakata matrix (PMNS matrix) [17], it can be parameterized as

$$U = \begin{bmatrix} U_{e1} & U_{e2} & U_{e3} \\ U_{\mu 1} & U_{\mu 2} & U_{\mu 3} \\ U_{\tau 1} & U_{\tau 2} & U_{\tau 3} \end{bmatrix} \tag{2.4}$$

$$= \begin{bmatrix} c_{12}c_{13} & s_{12}c_{13} & s_{13}e^{-i\delta} \\ -s_{12}c_{23} - c_{12}s_{23}s_{13}e^{i\delta} & c_{12}c_{23} - s_{12}s_{23}s_{13}e^{i\delta} & s_{23}c_{13} \\ s_{12}s_{23} - c_{12}c_{23}s_{13}e^{i\delta} & -c_{12}s_{23} - s_{12}c_{23}s_{13}e^{i\delta} & c_{23}c_{13} \end{bmatrix} \begin{bmatrix} 1 & 0 & 0 \\ 0 & e^{i\alpha_1/2} & 0 \\ 0 & 0 & e^{i\alpha_2/2} \end{bmatrix} . \tag{2.5}$$

Where $c_{ij} = \cos(\theta_{ij})$, $s_{ij} = \sin(\theta_{ij})$ with mixing angles θ_{ij}, δ is the Dirac CP-violating phase, and α_i are the Majorana CP-violating phases [18]. The mass eigenstates can be expressed with a plane wave solution

$$|\nu_j(t)\rangle = e^{-i(E_j\, t - \vec{p}_j \cdot \vec{x})} \ . \tag{2.6}$$

Where in the ultra-relativistic limit, energy can be approximated as $E = \sqrt{p_i^2 + m_i^2} \approx E + \frac{m_i^2}{2}$. This approximation combined with a convenient re-parameterization to distance yields

$$|\nu_j(L)\rangle = e^{-i\, m_j^2\, L/2E}\, |\nu_j(0)\rangle \ . \tag{2.7}$$

Hence the oscillation probability is given by

$$P_{\alpha\to\beta} = |\,\langle \nu_\beta(L)|\nu_\alpha\rangle\,|^2 = \left|\sum_j U_{\beta\, j}\; e^{-i\, m_j^2\, L/2E}\; U_{aj}^*\right|^2 = \sum_{j,k} U_{\alpha j}^* U_{\beta\, j} U_{\alpha k} U_{\beta k}^* e^{-i\, \Delta m_{jk}^2\, L/2E}, \tag{2.8}$$

with $\Delta m_{jk}^2 = m_j^2 - m_k^2$ [3]. It is clear from eq. (2.8) that the oscillation probability depends on the difference between the squared neutrino masses. The observation of neutrino oscillation therefore indicates that neutrinos have mass, as discussed in the preamble, although it is still uncertain as to how these masses are generated. In principle, the addition of right-handed neutrinos to the SM allows a Dirac neutrino mass to be generated from a coupling to the Higgs field, in the same manner as other leptons [19]. In this case one would need to explain why the neutrino mass is many orders of magnitude smaller than the other lepton masses. Alternatively, the neutrino could be a Majorana particle. This would push beyond the SM, but could offer a natural explanation for this discrepancy.

2.2 Dirac or Majorana?

In a nutshell, describing the neutrino as a Majorana particle, as opposed to a Dirac particle, simply means that the neutrino is its own antiparticle [19]. This means that the Majorana field must be invariant under charge conjugation up to an arbitrary phase factor, represented mathematically by [20]

$$\xi^c = e^{-i\eta}\xi \ . \tag{2.9}$$

The four component Dirac spinor can be expressed as

$$\Psi = \begin{bmatrix} \psi_R \\ \psi_L \end{bmatrix}, \tag{2.10}$$

with left and right handed projections $\Psi_L = [0\ \psi_L]^T$ and $\Psi_R = [\psi_R\ 0]^T$, respectively. The components ψ_L and ψ_R are eigenstates of the chirality projector $P_{L(R)} = \frac{1}{2}(1 \mp \gamma_5)$ [21]. These fields are described by the Dirac equation

$$i\hat{\sigma}^\mu \partial_\mu \psi_R - m\psi_L = 0\ , \quad i\sigma^\mu \partial_\mu \psi_L - m\psi_R = 0\ , \tag{2.11}$$

where $\hat{\sigma}^\mu = (\sigma^0, \vec{\sigma})$ and $\sigma^\mu = (\sigma^0, -\vec{\sigma})$ are the standard Pauli matrices. In this description the chirality eigenstates are coupled and have a mass m. The Majorana description posits the two component fields, Ψ_L with mass m_L and Ψ_R with mass m_R. They obey the independent equations

$$i\hat{\sigma}^\mu \partial_\mu \psi_L - m_L \psi_L = 0 \quad \text{and} \quad i\sigma^\mu \partial_\mu \psi_R - m_R \psi_R = 0\ . \tag{2.12}$$

From the Lagrangian perspective, this is neatly summarized in the most general Lorentz invariant mass term for the neutrino give by

$$\mathscr{L}_M = -\frac{1}{2} = [\bar{\nu}_L^c \quad \bar{\nu}_R] \begin{bmatrix} m_L & m_D \\ m_D & m_R \end{bmatrix} \begin{bmatrix} \nu_L \\ \nu_R^c \end{bmatrix}\ , \tag{2.13}$$

where m_D is the Dirac mass and m_L, m_R are the Majorana masses [21]. The Majorana mass terms however do not obey lepton number conservation (they are not invariant under the $U(1)$ gauge symmetry). The masses of the Majorana neutrinos are given given by the eigenvalues of the mass matrix (2.13)

$$m_{1,2} = \frac{1}{2}(m_L + m_R) \mp \frac{1}{2}\sqrt{(m_R - m_L)^2 + 4m_D^2}\ , \tag{2.14}$$

as discussed in [22].

2.3 The Seesaw Mechanism

The mechanism offers an explanation for the smallness of neutrino masses through lepton number violation; it reads as follows [22]:

- It is assumed that there is no left handed mass term, $m_L = 0$.
- The Dirac mass is generated by the standard Higgs mechanism, hence it is on the same order as an ordinary lepton mass.

— The right-handed Majorana mass breaks lepton number conservation, at a scale much larger than the weak scale, with the implication that $m_R \gg m_D$.

Under these conditions the Majorana neutrino masses reduce to

$$m_1 \approx \frac{m_D^2}{m_R} , \quad m_2 \approx m_R . \tag{2.15}$$

The masses of m_1 and m_2 can then 'seesaw' depending on the relative strengths of m_D and m_R, hence the name. A heavier partner for the neutrino is introduced through violation of lepton number, and explains the smallness of the observed neutrino mass. For this explanation to be useful, it must first be shown that the neutrino is Majorana. One approach to show this is through the search for a lepton number violating process, such as neutrinoless double beta decay [23].

2.4 Neutrinoless Double Beta Decay

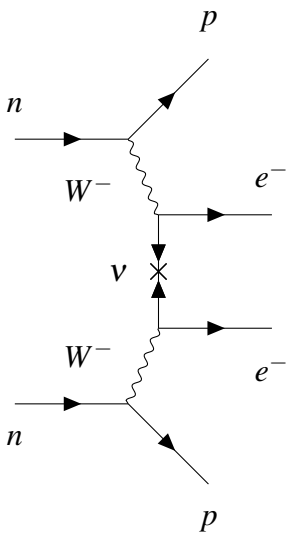

Figure 2.1 Feynman diagram for neutrinoless double beta decay occurring via light Majorana neutrino exchange.

Two-neutrino double beta decay ($2\nu\beta\beta$) is a rare process given by

$$(Z,A) \rightarrow (Z+2,A) + e_1^- + e_2^- + \bar{\nu}_{e_1} + \bar{\nu}_{e_2} , \tag{2.16}$$

which conserves both electric charge and lepton number. This transition typically occurs between nuclear ground states, $0^+ \rightarrow 0^+$. Although, in some cases it is energetically allowable

for the nucleus to decay into an excited state, $0^+ \to 2^+$ [21]. By contrast, $0\nu\beta\beta$ decay, as the name suggests, is given by

$$(Z,A) \to (Z+2,A) + e_1^- + e_2^- \ , \tag{2.17}$$

which violates lepton number conservation, the diagram for this is shown in fig. 2.1. If light Majorana neutrino exchange is the dominant contribution to $0\nu\beta\beta$ decay, the half-life can be expressed as

$$[T_{1/2}^{0\nu}(0^+ \to 0^+)]^{-1} = G^{0\nu}(E_0,Z) \left|M^{0\nu}\right|^2 m_{\beta\beta}^2 \ , \tag{2.18}$$

where $M^{0\nu}$ is the nuclear matrix element and $G^{0\nu}(E_0,Z)$ is a calculable phase space integral [5]. The factor $m_{\beta\beta}$ is the effective Majorana neutrino mass given by

$$m_{\beta\beta} = \left| \sum_j m_j U_{ej}^2 \right|^2 . \tag{2.19}$$

Where U_{ej} are the elements of the mixing matrix given in eq. (2.5) [24]. If the nuclear matrix elements are known and the decay rate is measured, the value of $m_{\beta\beta}$ can then be calculated. Conversely, if an upper limit is set on the half-life for $0\nu\beta\beta$ decay, a corresponding upper limit will then be set for $m_{\beta\beta}$.

The energy spectrum for emitted electrons will differ significantly for the two decay modes. In $2\nu\beta\beta$ decay, the spectrum will be continuous; similar to that of single beta decay. If no neutrinos are emitted, as in the $0\nu\beta\beta$ case, the emitted electrons will carry all of the energy released in the decay. This results in a peak at the end of the $2\nu\beta\beta$ spectrum [25], as shown in fig. 2.2. Thus the Q value is an important quantity to consider when picking an isotope to search for $0\nu\beta\beta$ decay. For $\beta\beta$ decay it is defined simply as

$$Q_{\beta\beta} = M(A,Z) - M(A,Z+2) \ , \tag{2.20}$$

where M is the isotope mass, A is the atomic number and Z is the proton number [26].
A good candidate for $\beta\beta$ decay will typically have an even number of protons, as well as an even number of neutrons [25]. This is because in some cases, pairing forces can make an even-even nucleus more tightly bound than its $(A,Z+1)$ neighbor, as illustrated in fig. 2.3. This has the effect of suppressing beta decay, which is crucial for observing $\beta\beta$ decay. Some examples of isotopes with this quality are given in table 2.1, with their natural abundance and $Q_{\beta\beta}$ value. In this work, ^{136}Xe is the isotope of choice in the search for $0\nu\beta\beta$ decay. The

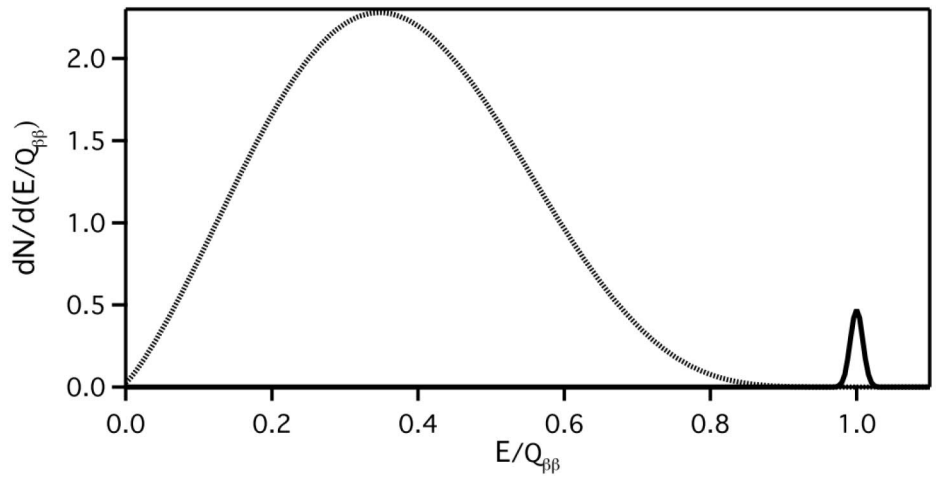

Figure 2.2 The total energy of both outgoing electrons, normalized by the decay $Q_{\beta\beta}$ value. The smaller peak resulting from $0\nu\beta\beta$ decay is exaggerated to increase its visibility, reproduced from ref. [25].

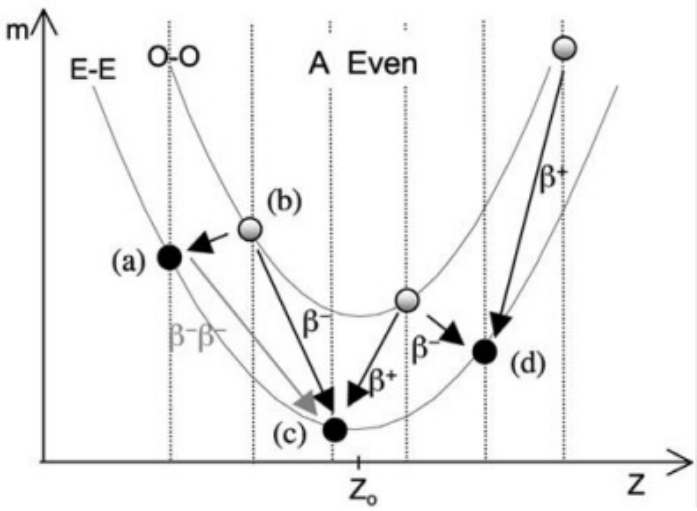

Figure 2.3 Pairing forces energetically forbid the beta decay of (a) to (b), allowing only double beta decay from (a) to (c). Reproduced from ref. [27].

motivation for which shall be discussed in the following chapter, along with the experimental methods used to search for it.

Table 2.1 Examples of double beta decaying isotopes with their relative abundance and $Q_{\beta\beta}$ value, taken from [28].

Isotope	Abundance (%)	$Q_{\beta\beta}(MeV)$
^{48}Ca	0.187	4.263
^{76}Ge	7.8	2.039
^{82}Se	9,2	2.998
^{96}Zr	2.8	3.348
^{100}Mo	9.6	3.035
^{116}Cd	7.6	2.813
^{130}Te	34.08	2.527
^{136}Xe	8.9	2.459
^{150}Nd	5.6	3.371

Chapter 3

Searching for neutrinoless double beta decay in ^{136}Xe

There are multiple reasons why ^{136}Xe is a suitable $0\nu\beta\beta$ decay candidate. For one, it has a natural abundance of 9%, but can be enriched to 80% or higher with centrifuge techniques in large quantities; making the enrichment process easier than that of a solid state isotope like ^{76}Ge [29]. It has a high enough $Q_{\beta\beta}$ value that conveniently places the signal region above most γ backgrounds. Moreover, since it has relatively high Z value, a 2.5 MeV γ will have an attenuation length of ~ 9 cm in liquid Xe (LXe) [30]. These characteristics render a monolithic LXe detector particularly capable of achieving very low backgrounds.

Another important feature is that Xe produces substantial scintillation light [31]. The collection of both scintillation light and ionization charge can be used to enhance the energy resolution and identify certain backgrounds; discussed in greater detail in section 3.2. Lastly, $\beta\beta$ decay in ^{136}Xe produces a stable ^{136}Ba ion, which offers the unique, albeit ambitious opportunity for an unambiguous measurement of $\beta\beta$ decay. This is the domain of Ba-tagging, the subject of section 3.4. First however, it is necessary to discuss the functional dependencies of an experiment's sensitivity to $0\nu\beta\beta$ decay, as it will be critical throughout Chapter 4.

3.1 Sensitivity

The expected number of $0\nu\beta\beta$ events for a given $\beta\beta$-emitting isotope after time t is yielded by the expression

$$N = \log(2)\frac{\varepsilon\, M\, N_A}{W}\frac{t}{T^{0\nu}_{1/2}}\ . \tag{3.1}$$

Where M and W are the mass and molar mass of the $\beta\beta$ emitting isotope respectively, ε is the detector efficiency and N_A is Avogadro's number [32]. The running time of the experiment, also known as livetime, is t and the product $M\,t$ is referred to as the exposure. Combining equations (2.18) and (3.1) an upper limit on $m_{\beta\beta}$ can be expressed as [33]

$$m_{\beta\beta} = A\sqrt{\frac{N}{\varepsilon M t}}\,, \tag{3.2}$$

with

$$A = \left(\frac{W}{N_A \log(2)\, G^{0\nu}\, |M^{0\nu}|^2}\right)^{\frac{1}{2}}\,. \tag{3.3}$$

In the limit of large background, the following approximation can be used

$$N \approx k\sqrt{b}, \tag{3.4}$$

where b is the mean expected background and k is a constant of proportionality [34]. Which means that an upper limit on a light Majorana neutrino mass can be expressed as

$$m_{\beta\beta} = A'\left(\frac{b^{1/2}}{\varepsilon\, M\, t}\right)^{1/2}\,, \tag{3.5}$$

with

$$A' = A\sqrt{k}\,. \tag{3.6}$$

This is an important result to consider when deciding if a background reduction technique is worth the loss of livetime it may cause. It is clear that a large mass of the candidate isotope needs to be deployed in a very low background environment, in order to detect $0\nu\beta\beta$ decay, or set a competitive upper limit on $m_{\beta\beta}$. The following sections will explore the ways in which the EXO collaboration attempts to meet this challenge.

3.2 The EXO-200 Detector Experiment

EXO-200 is an experiment searching for $0\nu\beta\beta$ decay with $\sim$ 200 kg of Xenon, enriched to 80.6% in the isotope ^{136}Xe, with $\sim$ 175 kg in liquid phase. The remaining 19.4% is mainly ^{134}Xe with a low concentration of other isotopes [6]. The experiment is currently in operation at the Waste Isolation Pilot Plant (WIPP) in New Mexico, USA. The detector vessel is a cylindrical Time Projection Chamber (TPC), with a cathode held at a negative high voltage in the mid-plane. Thus the vessel is in fact a double TPC. Energy deposited in LXe produces free ionization charge and scintillation light with a strong anti-correlation [35]. Wire planes

at each end of the TPC serve to collect ionization charge, which drifts under the electric field created by the cathode. Scintillation light is collected by large area avalanche photo-diodes (LAAPDs) positioned behind the wire planes. The cathode is 90% transparent to scintillation light which is detected at both ends of the TPC [6]. The ionization charge on the other hand is only detected in the TPC half it is produced in. The wire planes consist of separate "U" and "V" wires that have a relative angle of 60°.

The V plane is in front of the U plane and biased in such a way that it is transparent to passing electrons, see fig. 3.1 for details. The charge deposition and induction in the U and V planes, respectively, allow for the reconstruction of two of the event coordinates. After being recorded as U and V coordinates they are then converted to X and Y, as shown in fig. 3.2. The third coordinate is reconstructed with the time difference between the arrival of scintillation light and ionization charge. There is a gap of 6 mm between the U and V planes and also between the V plane and LAAPD layer [6]. Plastic-scintillator veto panels surround the experiment on all sides, allowing for the detection of passing muons, which helps to mitigate the backgrounds they create. The muon flux is greatly reduced by the 1624 m of water equivalent overburden shielding [36].

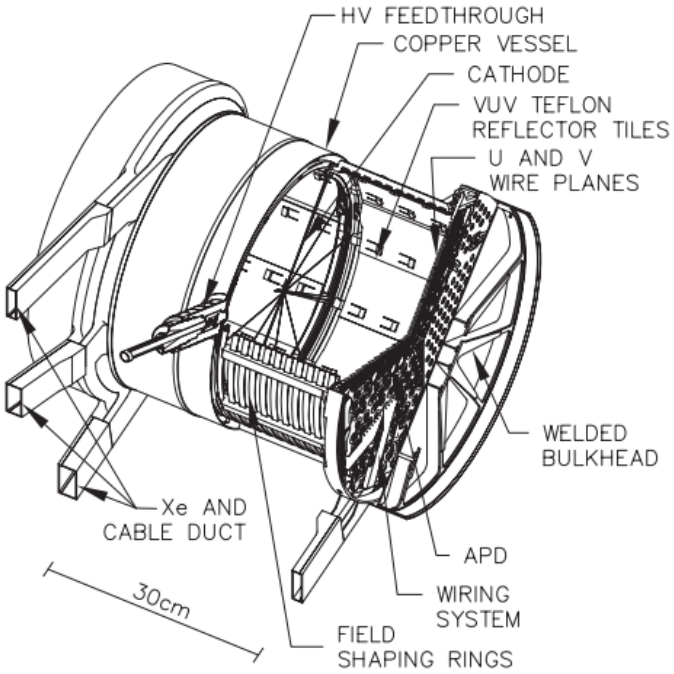

Figure 3.1 The EXO-200 TPC and its main components. Reproduced from [6].

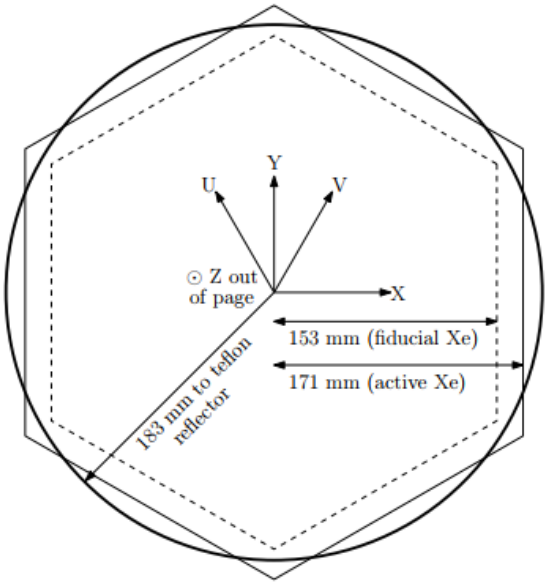

Figure 3.2 View of the EXO-200 cross-section, displaying the U-V and X-Y coordinate systems used, as well as the fiducial and active Xenon volumes. Reproduced from [37].

The $Q_{\beta\beta}$ value for $0\nu\beta\beta$ decay, at 2457.83 $\pm$ 0.37 keV [38], is well above most gamma ray backgrounds, as mentioned in the chapter preamble. However, the attenuation length for gamma rays with energy near the $Q_{\beta\beta}$ value is quite long ($\sim$ 9 cm) relative to the detector dimensions. Thus it is especially important that the experiment is shielded sufficiently, and constructed with radiopure materials. The LXe container is made primarily from copper, with a length of 44 cm and a diameter of 40 cm. Due to their proximity to LXe the cylinder walls are extremely thin, with a thickness of only 1.37 mm [6]. This is also part of the motivation behind using LAAPDs, since they have very low radioactivity. The TPC is contained within a twelve-sided double-walled copper cryostat. The cryostat is surrounded by at least 25 cm of lead shielding, as shown in fig. 3.3.

The data is binned into 2 ms long events, with the scintillation and charge signals grouped into individual energy deposits. If the energy is deposited in one location within the TPC, the event is identified as Single-Site (SS). If there is more than one energy deposit the event is identified as Multi-Site (MS). This distinction helps to discriminate between the gamma ray backgrounds, which are mostly MS, and the $0\nu\beta\beta$ signal, which is mainly SS [39]. The scintillation light is produced with a wavelength of $\lambda = 175$ nm [40], ultra-violet reflective Teflon-PTFE tiles plate the TPC walls to cover the inside of the field shaping rings.

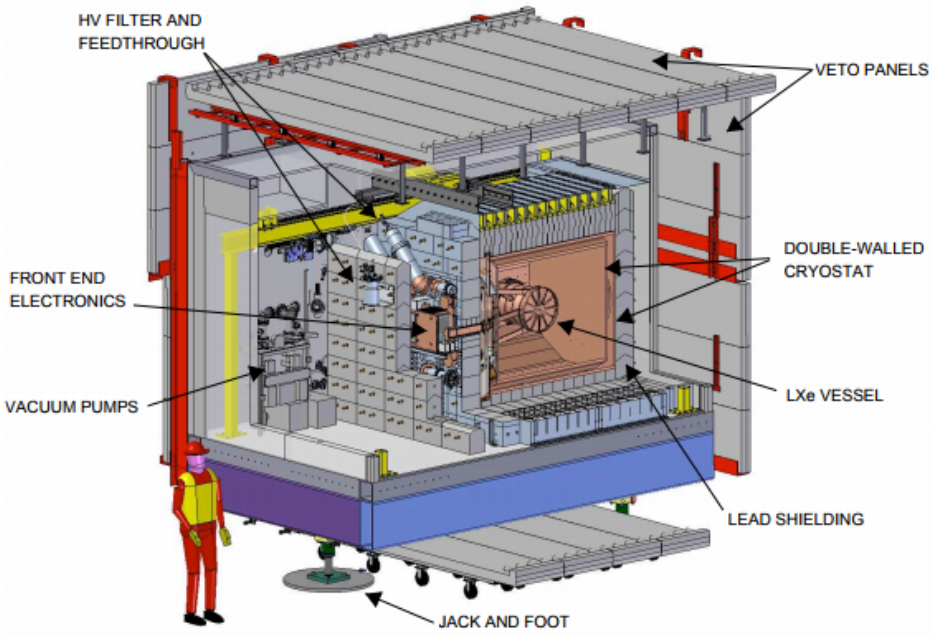

Figure 3.3 Inside the EXO-200 clean room at WIPP. Reproduced from [6].

Phase-I data was recorded between Sep 2011 to Feb 2014 with the cathode biased at -8 kV, after which EXO-200 was forced to suspend activities due to accidents at WIPP. The experiment began taking data again with upgraded electronics in May 2016, with the cathode biased at -12 kV, hereafter referred to as Phase-II data [41]. Both Phase-I+II data were blinded to mask candidate $0\nu\beta\beta$ events. To calibrate the detector energy scale, the sources ^{60}Co, ^{228}Th and ^{226}Ra are regularly positioned 10 cm from the LXe.

The 2D energy spectra are rotated and projected onto a 1D energy variable in a way that minimizes the 2615 keV gamma line [37]. This rotation allows for the optimization of energy resolution. The 2D spectrum also helps remove α backgrounds, as they have a much larger scintillation/ionization ratio. An example 2D energy spectrum is given in fig. 3.4. The energy resolution is parameterized with the following function

$$\sigma^2 = a\sigma_e^2 + bE + cE^2, \tag{3.7}$$

where σ_e is the electronic noise, bE models statistical fluctuations in the ionization and scintillation signals, cE^2 models higher order position and time dependent broadening [37]. At the $Q_{\beta\beta}$ value, it is found that $\sigma/E(Q_{\beta\beta}) = 1.38\%/1.23\%$ for Phase-I and Phase-II data, respectively [41]. Probability density functions (pdfs) are created for the expected SS and MS spectra using GEANT4 simulations. The charge depositions are transported to the U V

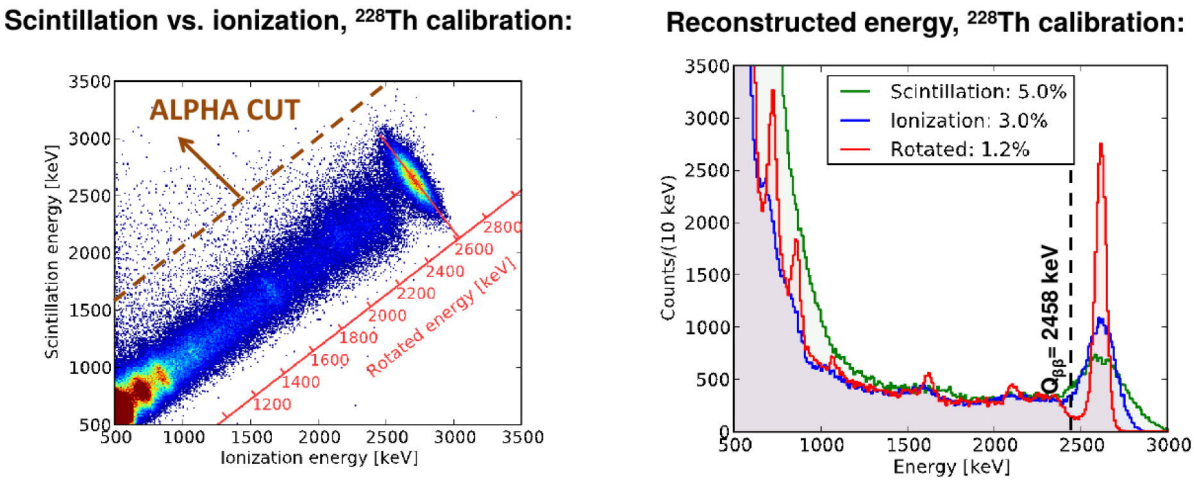

Figure 3.4 (left) A 2D plot of the scintillation and ionization energy recorded for SS events from a ^{228}Th source. Alpha backgrounds can be identified by their larger scintillation to ionization ratio. (right) Comparison of SS energy spectra plotted using scintillation, ionization and a linear combination of the two (rotated), for ^{228}Th. Reproduced from [42].

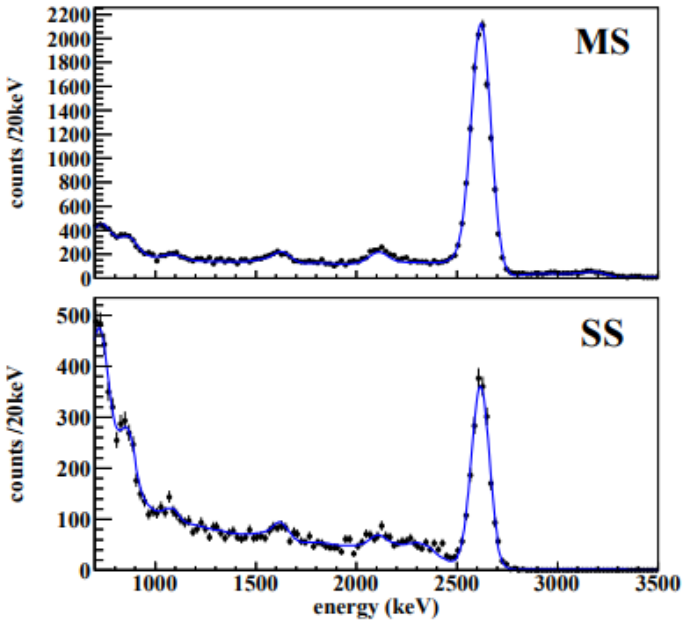

Figure 3.5 A comparison between a Monte-Carlo produced pdf and data, for SS and MS events from a ^{228}Th calibration run. Reproduced from [39].

wires, where a signal is generated with a model of the electronics. The pdfs are broadened with the resolution function and their normalizations are obtained with a fit to the data, an example of which is shown in fig. 3.5.

Once all of the expected backgrounds have been generated, the combined pdf is then fitted to low background data, as shown in fig. 3.6. In the most recent $0\nu\beta\beta$ search both Phase-I+II have been unblinded and fit using a Maximum Likelihood (ML) method. As of yet no statistically significant evidence for $0\nu\beta\beta$ decay has been observed. However a lower limit on the half-life sensitivity has been set at $T_{1/2} > 1.8 \cdot 10^{25}$ yr, which corresponds to an upper limit on the light Majorana neutrino mass of $m_{\beta\beta} < (147 - 398)$ meV [41]. The range of $m_{\beta\beta}$ results from the uncertainty that arises in the model dependent nuclear matrix element calculation.

EXO-200 was the first experiment to observe $2\nu\beta\beta$ decay in ^{136}Xe [43]. It has also been used to search for $2\nu\beta\beta$ decay in ^{134}Xe [44], however no statistically significant evidence has yet been found. To increase the sensitivity to $0\nu\beta\beta$ decay, more ^{136}Xe is needed, a tonne-scale experiment is required to push up the half-life lower limit.

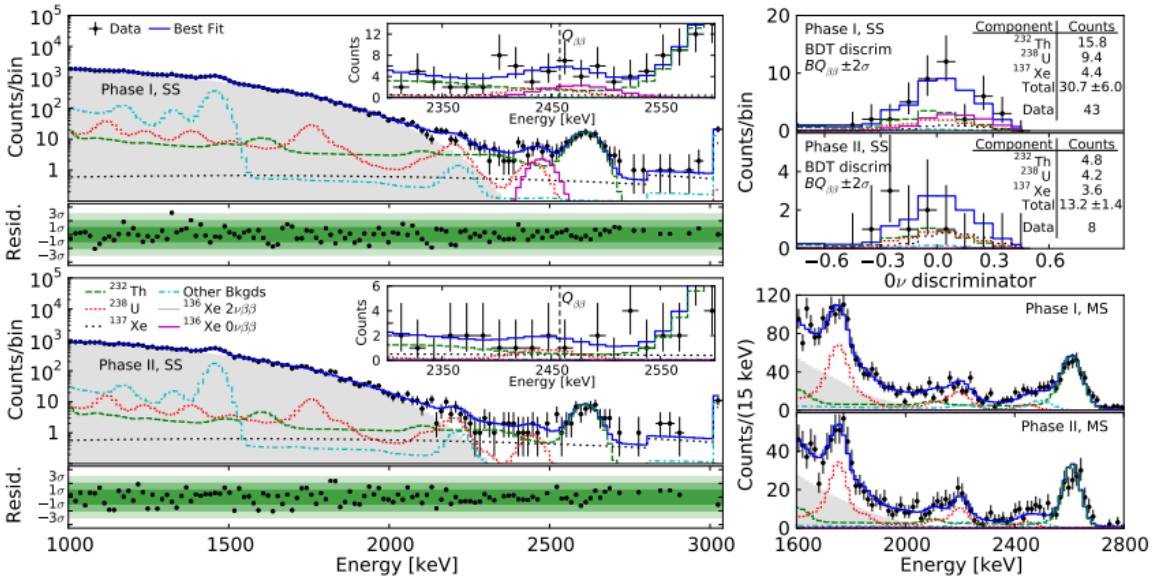

Figure 3.6 The fit of Monte-Carlo generated pdfs to Phase-I+II low background data. Reproduced from [41].

3.3 The nEXO Project

nEXO is a planned experiment that will contain ∼5 tonnes of LXe enriched to 90% in the isotope ^{136}Xe. Instead of having a cathode in the mid-plane like EXO-200, the cathode will be placed at the bottom of the TPC, as a mid-plane cathode would introduce more radioactivity to the fiducial volume. The walls of the TPC will be lined with field shaping rings that

will provide a uniform electric drift field of about 400 V/cm. Silicon photomultipliers will be placed behind the field shaping rings and mounted onto the barrel of the TPC, they will be used to collect the scintillation light. The ionization charge is to be collected by arrays of 10x10 cm^2 dielectric tiles, which will be positioned at the top of the TPC [45]. The signal will then be read out by ASIC chips installed on the reverse side of each charge collection tile.

The TPC will be placed within a double walled cryostat, which will be filled with approximately 33 tonnes of HFE-7000. The inner and outer cryostat walls have been modeled as spheres with radii of $\sim$ 340 cm and $\sim$ 450 cm respectively. The double wall provides insulation for the cryostat and the large amount of HFE fluid provides shielding from external radiation, and radiation from the HFE itself. This configuration is to be mounted from the roof of a water tank which is about 10 m in height and 9 m in diameter. The water acts both as shielding and an active muon veto. The location of nEXO is still undecided, however, simulations have been conducted under the assumption that it will be based at the Sudbury Neutrino Observatory Laboratory (SNOLAB), in the existing cryopit. This location provides an overburden of 6010 m water equivalent [46], which is a significant increase compared to EXO-200. This increase will provide a massive reduction to muon induced backgrounds.

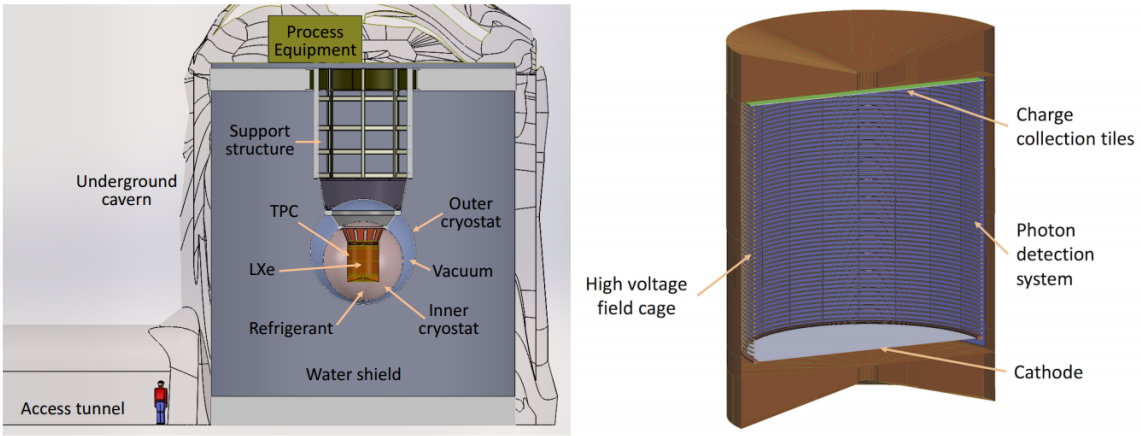

Figure 3.7 An overview of the planned nEXO experiment, to be located at SNOLAB. Reproduced from [7].

It is not without the realm of possibility that nEXO can reach a sensitivity to ^{136}Xe $0\nu\beta\beta$ decay of 10^{28} years, with a livetime of 10 years [7], as shown in fig. 3.8. Even in a monolithic detector such as this, efficient background rejection will play a crucial role in the search for

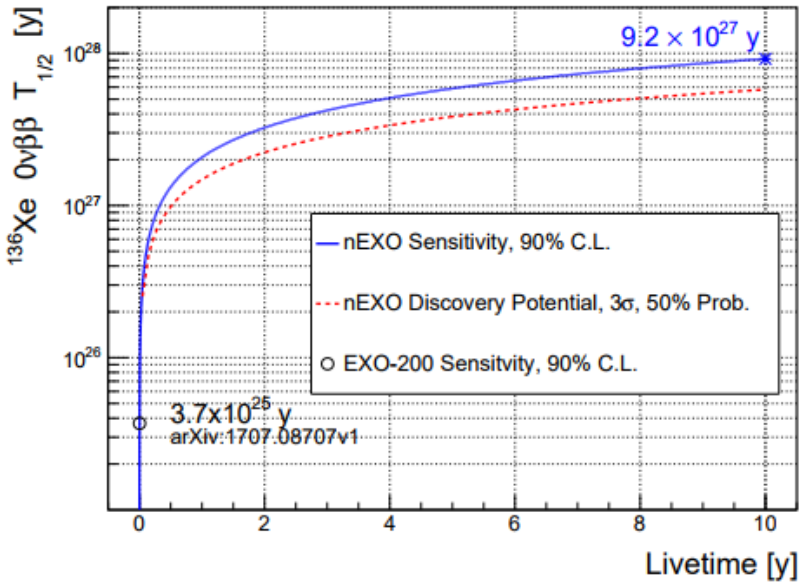

Figure 3.8 The median sensitivity for nEXO at 90% CL and 3σ discovery potential. Reproduced from [7].

$0\nu\beta\beta$ decay. Ba-tagging is a background rejection method that will not only increase the sensitivity, but can also to verify the signal.

3.4 Ba-tagging for $\beta\beta$ decay verification

The $\beta\beta$ decay process of Xe produces a Ba^{++} ion, which is expected to reduce to Ba^{+} in LXe. This presents a unique opportunity; since the daughter ion is stable it can potentially be located, extracted and identified. If this is done successfully, it would allow for a background free and unambiguous measurement of $\beta\beta$ decay in ^{136}Xe. Thus, reliable extraction and transport to the tagging apparatus is required for the final Ba-tagging process. This tagging process can significantly boost the experiment's sensitivity, even if it is not 100% efficient. It will also serve as a direct verification of the $0\nu\beta\beta$ signal. Multiple methods of Ba tagging are currently being explored by the nEXO collaboration, some have been developed for gaseous Xe and others for liquid.

3.4.1 Ba-tagging in the World

One method of extracting the Ba ion, which is being researched at Colorado State University, is to move a cold probe near the reconstructed $\beta\beta$ decay candidate event, and freeze some of the surrounding LXe onto it [47]. The Ba ion, now trapped in Xe, can then be removed from the TPC and detected with matrix isolation spectroscopy. Laser light can be passed through an optical fiber within the probe to excite the single Barium ion/atom. The fluorescent light produced by the Ba is focused onto a CCD chip, for identification.

At Stanford University, a similar approach is being taken in which the Ba ion is attracted electrostatically to a substrate, which is mounted onto a probe, and absorbed by it [48]. The substrate is then transported to a vacuum environment by the probe, where the Ba atom is removed by laser induced thermal desorption. The Ba atom is then re-ionized and identified by resonance ionization spectroscopy, which stimulates electronic transitions in Ba and ionizes it. After which, it is sent to a mass time-of-flight mass-spectrometer for further verification.

A group at the University of Texas in Arlington has adapted the technique of single molecule fluorescence imaging for Ba-tagging [49]. This is to be used by the NEXT collaboration, which is searching for $0\nu\beta\beta$ decay with a high pressure gaseous Xe TPC [50]. A fluor that is non-fluorescent can become fluorescent upon chelation with a suitable ion. Typically this ion is Ca^{++}, however, since the Ba ion is expected to remain Ba^{++} in gaseous Xe, and because Ca and Ba are congeners, the same dyes that have been developed for Ca can be used for Ba. Upon excitation and emission of light, the single molecule can be localized with extreme

precision by an electron-multiplying CCD camera. This technique has been demonstrated by NEXT to work with Ba, which can be localized to within ~ 2 nm [51].

3.4.2 Ba-tagging in Canada

The nEXO collaboration has also entertained the possibility of extracting the Ba ion from a gaseous TPC. If a $\beta\beta$ decay-like event is detected, the electric field would be altered in a way that ions in the volume of interest are drifted to an extraction port, where they are flushed out with Xe gas. Extraction of the Ba ion from the TPC must ideally be done with near 100% efficiency. For this purpose a radio-frequency (RF) only ion-funnel extraction technique has been developed [52, 53], to extract ions from a high pressure noble gas environment into vacuum (10 bar to 10^{-6} mbar). The RF-only ion funnel has no applied DC field. Ions are transported along the funnel axis by the residual gas flow, and they are confined radially by the RF field. The electrically neutral gas escapes through the inter-electrode spacings and is subsequently pumped away. An overview of the funnel is given in fig. 3.9.

The prototype funnel, which was developed at Stanford University, was combined with a Thermo-Finnigan Linear Trap Quadrupole (LTQ) and used to measure the mass spectrum of ions extracted from Xe gas up to 10 bar. This combination showed that the funnel design was largely successful, however it suffered from various limitations, one of which was the sensitivity of the LTQ. A new and improved setup is being developed in a collaboration between McGill, TRIUMF, and Carleton. The new system will have two or three sequential funnels for increased ion transmission efficiency. After passing through the funnels, ions are cooled with a Helium buffer gas and captured with a Linear Paul Trap (LPT), where the Ba ion can be identified with laser-fluorescence spectroscopy [54]. An overview of the LPT is shown in fig. 3.10.

For further identification of the ion species produced in the extraction sequence, the LPT can bunch ions and eject them into a multiple-reflection time-of-flight mass-spectrometer (MR TOF). The MR TOF can then separate ions by their mass with an unprecedented resolution. This additional method of identification will allow for systematic studies of the ion extraction process. It can also confirm that the Ba ion tagged in the LPT is indeed ^{136}Ba. Mass Spectrometry with the MR TOF is discussed at length in Chapter 5. The next chapter however, shall explore a data analysis technique that can be used to reject a particular background to $0\nu\beta\beta$ decay with the EXO-200 detector.

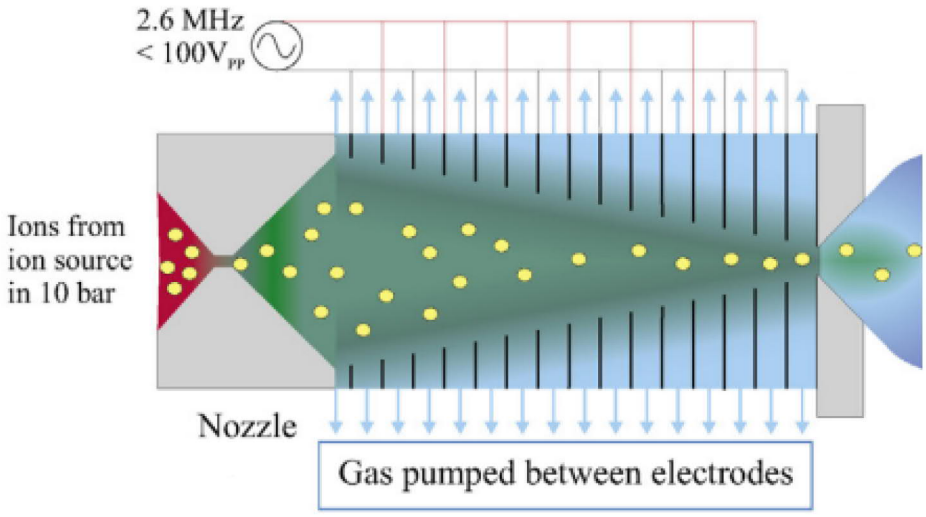

Figure 3.9 A model of the RF-only funnel that allows for the extraction of ions from a high pressure environment to a vacuum. Reproduced from [52].

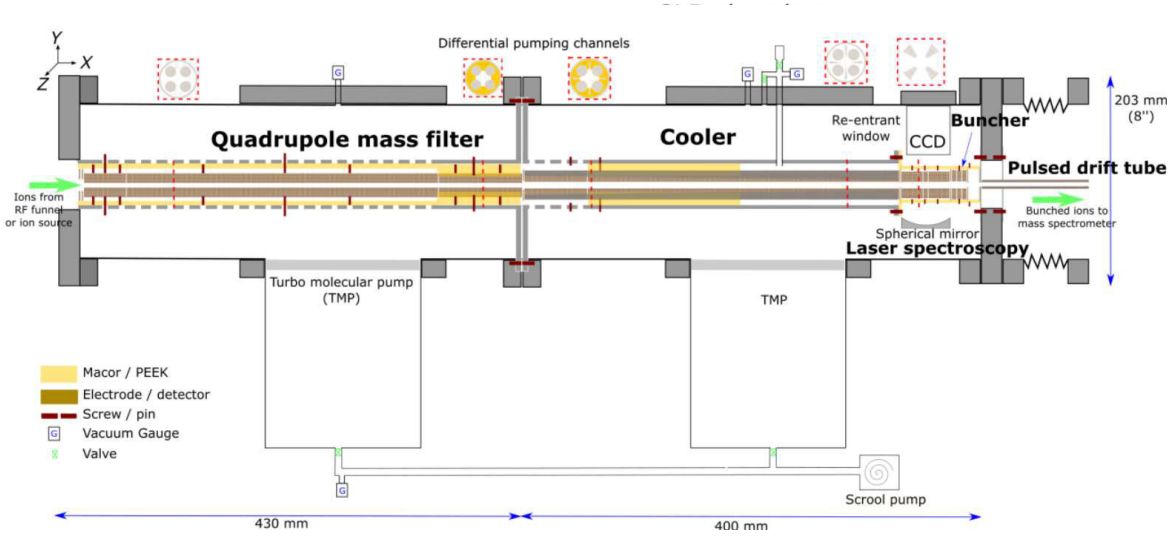

Figure 3.10 Overview of the Linear Paul Trap (LPT), designed by Yang Lan at TRIUMF. Reproduced from [55].

Chapter 4

Data Analysis with EXO-200

To expand upon some of the concepts mentioned in Section 3.2, it is useful to construct variables that help to discriminate against certain backgrounds. The Single-Site (SS) and Multi-Site (MS) variables discussed earlier are a simple example. A SS event occurs when all of the charge is deposited in a volume with a characteristic length of 2-3 mm [37], otherwise it is MS. Since it is know that $0\nu\beta\beta$ decay candidate events will mainly be SS, MS events with energy near the $Q_{\beta\beta}$ value can be easily rejected. Another example is the standoff distance, which is classified as the shortest distance between a charge-deposition and material other than LXe [37]. This helps to discriminate against γ backgrounds, which tend to originate from detector materials, whereas $\beta\beta$ decay occurs uniformly in the LXe.

In an example analysis searching for $0\nu\beta\beta$, the events are classified as SS or MS, then the rotated energy and standoff distance spectra are simultaneously fit using maximum-likelihood [39]. The pdfs supplied to the fit are generated by Monte-Carlo (MC) simulation of the signal and backgrounds. In this way, the relative contribution of a particular background can be quantified, although, this measurement can be correlated with other backgrounds. This technique can be used to measure the efficiency of a background rejection technique, as shall be shown in this chapter. The background in question is created by the decay of the cosmogenically produced radionuclide ^{137}Xe.

4.1 Cosmogenic backgrounds to EXO-200

As previously discussed, there are backgrounds to $0\nu\beta\beta$ searches resulting from the inherent radioactivity of detector materials. These backgrounds can be mitigated through careful selection of detector materials, shielding, and the reduction of material in proximity to the

LXe. There are other backgrounds, however, that result from cosmic rays and cosmogenic activation. These are more difficult to shield against. It is for this reason that experiments of this nature are placed deep underground. Even deep underground, cosmic muons can interact with the detector materials to produce neutrons via muon spallation, as shown in fig. 4.1, resulting in a neutron flux through the cryostat and TPC. The background of most interest in this work is produced by neutron capture on ^{136}Xe, that creates the radionuclide ^{137}Xe. This section will outline the ways in which this neutron capture may be identified.

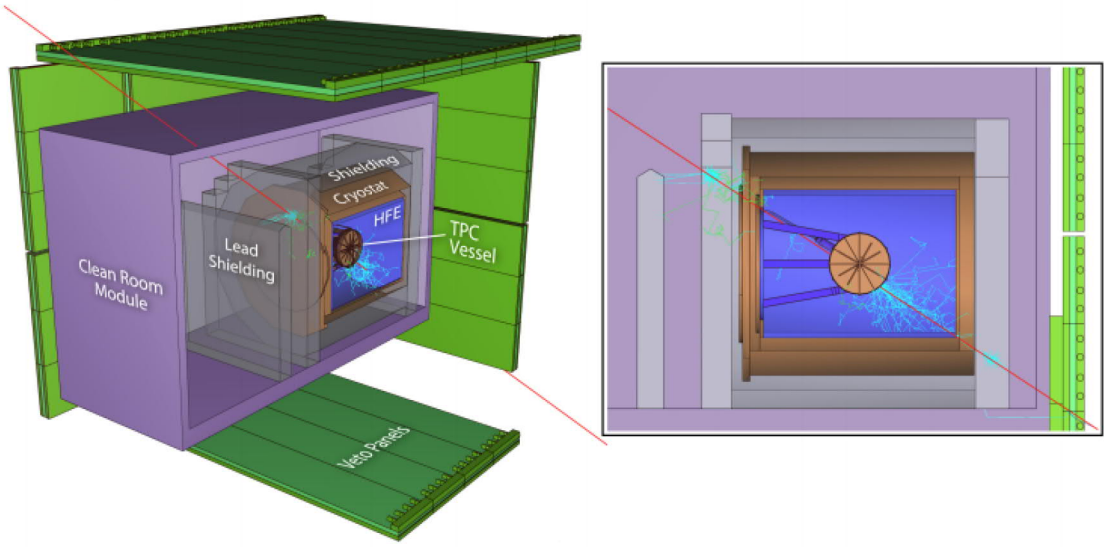

Figure 4.1 Simulation of a muon passing through the EXO-200 clean room and TPC. Reproduced from [36].

^{137}Xe is prone to beta decay, with a half-life of 3.82 min [8], creating coincident γ's only 33$\pm$3% of the time [56], thus the decay will typically appear to be SS and pass the SS/MS cut. The Q value for the decay is 4173$\pm$7 keV [57], hence it can contribute to counts within the $0\nu\beta\beta$ region of interest (ROI). Another important feature of this radionuclide is that it is created in an excited state with an energy of 4025.46$\pm$0.27 keV [58]. It will promptly transition to the ground-state through the release of capture γs, which are distributed isotropically [36].

The most common capture γ associated with neutron capture on ^{136}Xe has an energy of 601 keV, and the total energy released in the cascade can range between 600-4025 keV [59]. Another neutron capture of interest is on the ^{1}H present in the HFE-7000 fluid, which results in the emission of a single 2223 keV γ [60]. This capture on ^{1}H can potentially fake a neutron

capture on ^{136}Xe, as the γ it emits has an energy within the cascade interval.

In summary, a ^{136}Xe neutron capture event can be identified by a muon veto panel trigger, followed by an event containing one or more γ-like energy deposits with a total energy between 600-4025 keV, with the possible exclusion of the ^{1}H neutron capture emission line at 2223 keV. The following section will demonstrate how this information can be used to mitigate the effects of ^{137}Xe decay, using a series of software scripts. These scripts form an algorithm referred to simply as the ^{137}Xe veto.

4.2 The ^{137}Xe Veto

The first step in the algorithm is to identify events with energy deposited in one or more scintillation clusters, that occur $10-5000$ μs after a muon veto-panel trigger, as motivated by fig. 4.2. This window is chosen to ignore Bremsstrahlung from muons passing through the TPC that dominate immediately after the veto panel trigger, as well as the radioactivity induced $2\nu\beta\beta$ events that dominate at later times [36]. Events that occur under these circumstances are tagged for neutron capture, the energy spectrum of which is shown in fig. 4.3. A cut was placed on the energy to select candidate ^{136}Xe neutron capture events. The minimum energy was set at the ^{137}Xe 600 keV emission line, reduced by 3σ, where σ is the energy resolution given by eq. (3.7), to 480 keV. The maximum energy was likewise set to 4025+3σ = 4180 keV. The region of 2.1-2.3 MeV is removed to ignore the neutron capture on ^{1}H as shown in fig. 4.3.

Once the neutron capture events are identified, the positions of the outermost γ clusters are used to set up a volume around the ^{137}Xe atom, as shown in fig. 4.4. A small length is added to these positions, to account for any drift or lack of isotropy in the released γ's. The veto volume is then ignored for data analysis for a length of time, which should be long enough that the ^{137}Xe decay is negated. Events in the data that fall within this volume and time window are not considered in the analysis.

By combining eqs. (2.18) and (3.5), sensitivity to the $0\nu\beta\beta$ half-life can be roughly expressed as

$$S \propto \frac{\text{signal}}{u(\text{background})} \,, \tag{4.1}$$

with,

$$\text{signal} \propto \text{livetime} \,, \quad u(\text{background}) = \sqrt{\text{background}} \,. \tag{4.2}$$

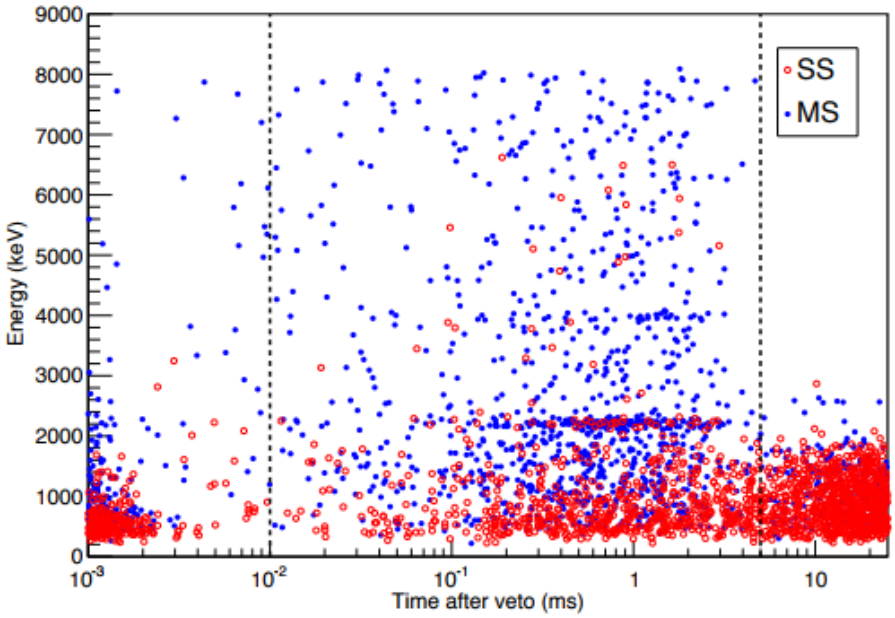

Figure 4.2 Events in the data that occur shortly after a muon veto panel trigger. The lines created by neutron capture on ^{1}H and ^{136}Xe are visible at 2000 keV and 4000 keV respectively. Shortly after the veto trigger, the data is dominated by muon Bremsstrahlung. At longer times, SS $2\nu\beta\beta$ events dominate. This motivates the choice of searching for capture events between 10-5000 μs. Reproduced from [36].

To maximize the sensitivity,

$$\chi \equiv \frac{\text{bkgd}}{\text{livetime}^2} \tag{4.3}$$

needs to be minimized. The bkgd is the total background within 2σ of the ROI (ROI$\pm 2\sigma$), calculated with the number of fitted pdf events for each background. Rather than a precise and lengthy livetime calculation the approximation

$$\text{livetime} \propto 2\nu\beta\beta \tag{4.4}$$

is used, where $2\nu\beta\beta$ is the fitted number of $2\nu\beta\beta$ events. This is justifiable since only the relative value is significant. The veto time and volume are to be chosen such that the sensitivity is maximized. Alternatively, instead of setting up a vetoed volume around the neutron capture, the TPC half containing the capture could simply be vetoed. As shall be shown, the two approaches have similar effects.

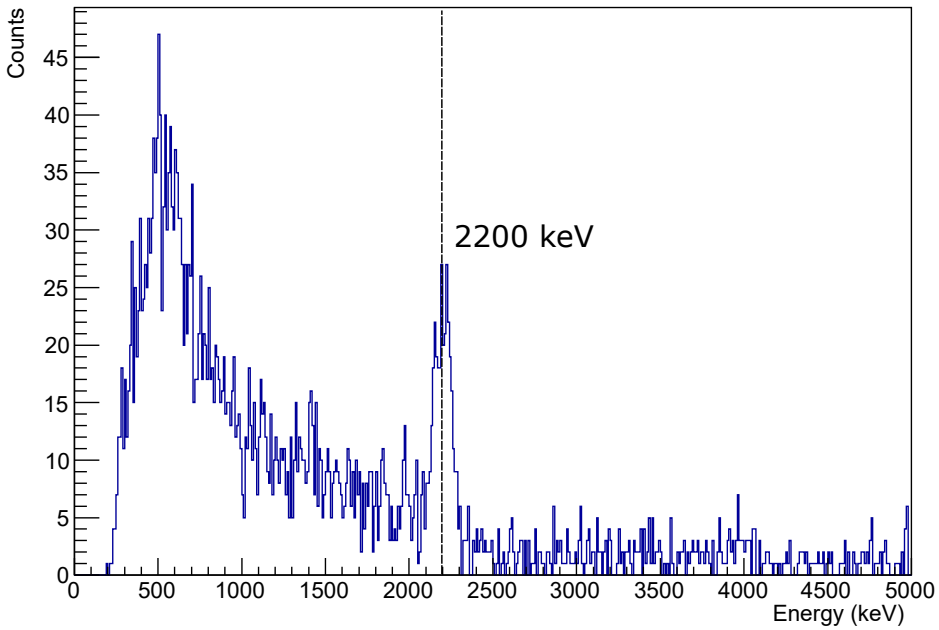

Figure 4.3 The energy spectrum of neutron capture tagged events for Phase-I data. The clear spike at 2200 keV results from the single γ emission from neutron capture on ^{1}H, contained in the HFE-7000 fluid.

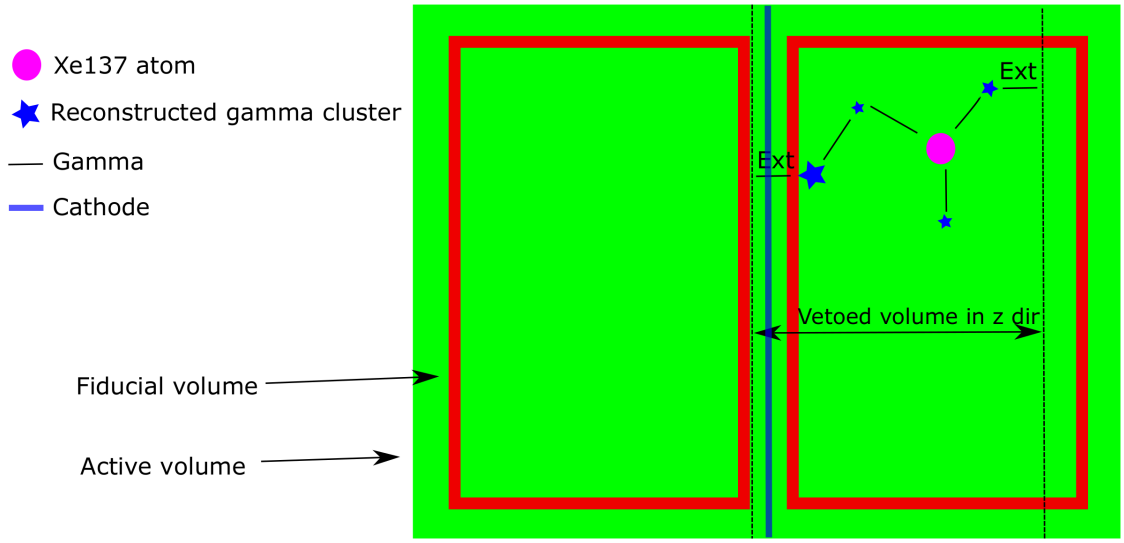

Figure 4.4 Example of the ^{137}Xe veto in the z direction. A small length is added to the position of the outermost γ cluster position, to form the veto volume.

4.3 Results of the ^{137}Xe Veto

The Phase-I data set is subdivided into Run 2abcd, where abcd refer to low-background data taking time periods between extended calibration campaigns. Work began with the optimization of the veto using only Run 2abc data. The approach was to vary the veto time and extension added to the outermost x y and z γ positions, as shown in fig. 4.4, over a 2D grid of points. For future reference this extension will be referred to as *xyz* Extension. The MC background pdfs were then fitted to the data at each point in the grid, from which counts for each background were obtained. The 2D grid allowed the optimization to be performed in parallel and vastly sped up the computation time.

For Run2 abc data, the optimal veto used an *xyz* Extension of 7 cm and a veto time of 9 min, resulting in a $\sim 40\%$ reduction in ^{137}Xe counts, $\sim 10\%$ reduction of total background within the ROI$\pm 2\sigma$, for only a 1% loss of livetime, shown in figs 4.5 and 4.6. However, the veto performed much worse when applied to the full Phase-I data set. The reduction in ^{137}Xe counts dropped to $\sim 25\%$, shown in fig. 4.7. This indicated that fitting pdfs to data is an unreliable method of optimizing the veto, since ^{137}Xe counts are correlated with other backgrounds.

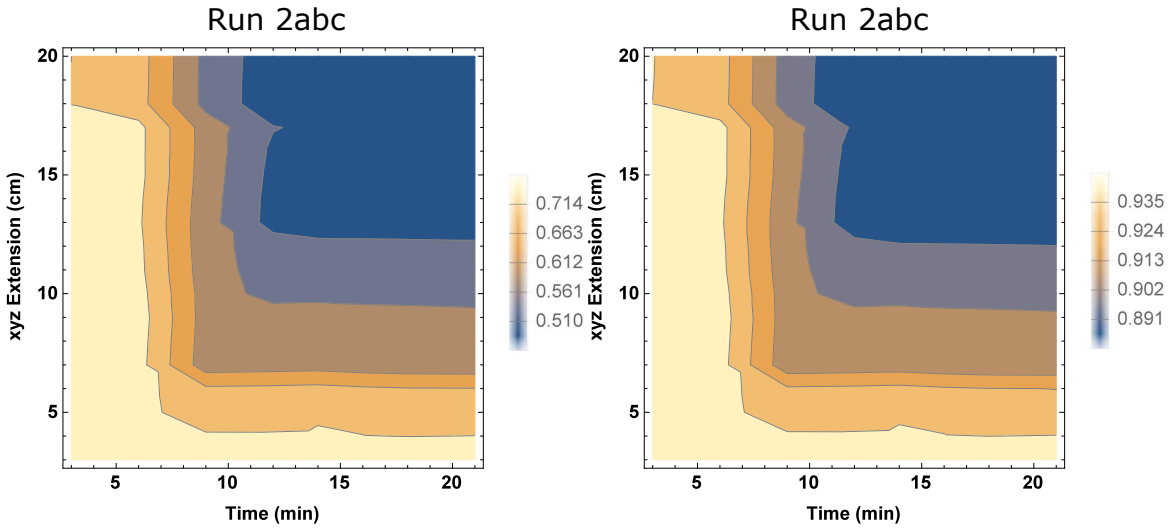

Figure 4.5 (left) The normalized number of fitted ^{137}Xe counts. (right) The normalized number of total background counts within the ROI $\pm 2\sigma$. Both are plotted on a grid of time vs. *xyz* Extension for Run 2abc data. A reduction of ^{137}Xe counts by 50% corresponds to a reduction in total background in the ROI$\pm 2\sigma$ of about 10%.

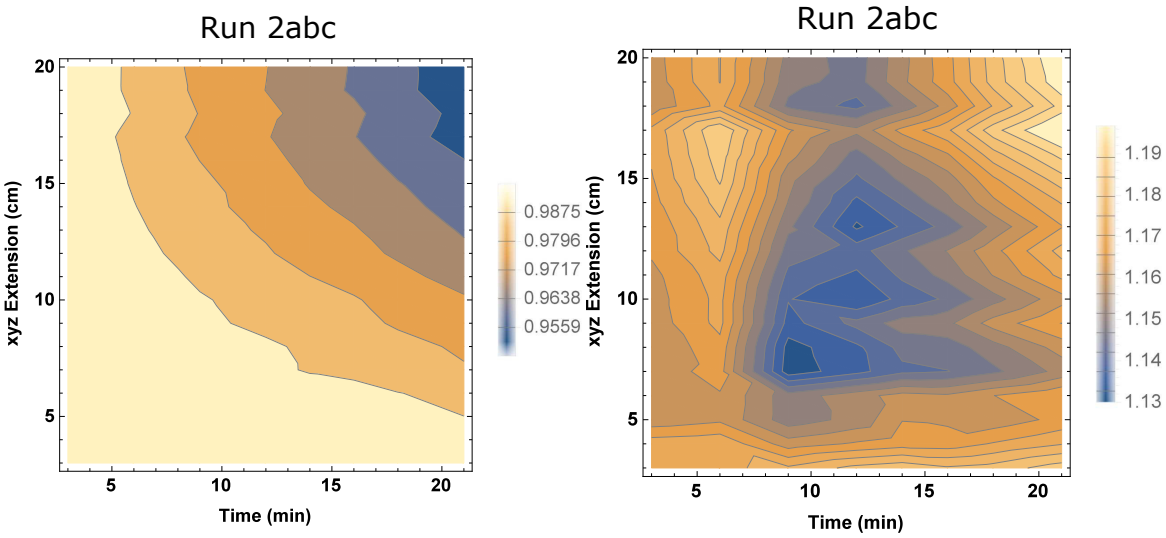

Figure 4.6 (left) The normalized number of fitted $2\nu\beta\beta$ counts, which is used as the fraction of remaining livetime. (right) The rough metric given by eq. (4.3), where the scale of the vertical axis is arbitrary. Both plots are for Run 2abc data. This gives an optimum at *xyz* Extension = 7 cm and veto time of 9 min, which corresponds to a livetime loss of $\sim 1\%$ and reduction in ^{137}Xe counts of $\sim 40\%$.

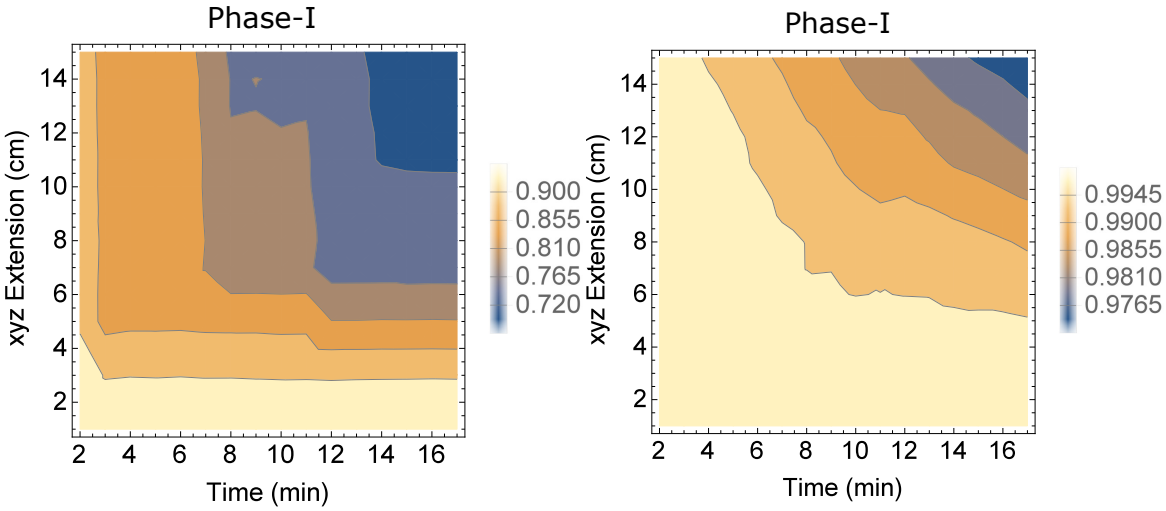

Figure 4.7 (left) The normalized number of fitted ^{137}Xe counts. (right) The normalized number of fitted $2\nu\beta\beta$ counts. Both plots are for full Phase-I data. This shows a maximum reduction in ^{137}Xe counts of $\sim 25\%$, for a loss in livetime of 2.5%.

To check the fit results, the data region between 2800-3600 keV, which has a high purity of of ^{137}Xe events, was used to evaluate the veto performance. The number of counts in this region can then be found as a function of veto time, and fit with

$$\text{counts} = p_0(p_1 + (1 - p_1 e^{-\ln(2)t/3.82})), \tag{4.5}$$

where the efficiency can be extracted as $1 - p_1$. Initially this was done for a veto of the entire TPC volume, which was later restricted to the TPC half containing the event, to regain some of the lost livetime. The steps taken to regain lost livetime and their effectiveness are summarized in fig. 4.9. This study was conducted for Phase-I+II data in lieu of an upcoming analysis. The rejection efficiency for ^{137}Xe events is $\sim 21\%$, with $\sim 6\%$ reduction in total background within ROI$\pm 2\sigma$, for a veto time of approximately 20 min, shown in fig. 4.8. This corresponds to a loss in livetime of 3.5% as shown in fig. 4.9. The increase in sensitivity begins to plateau at 2%. There is no clear optimum in terms of veto length, the final veto cut uses a physically motivated time of 19.1 min (5 half-lives). Vetoing half the TPC volume leads to a sensitivity increase comparable to vetoing a dynamic volume created with the capture γs, yet is simpler to implement and understand.

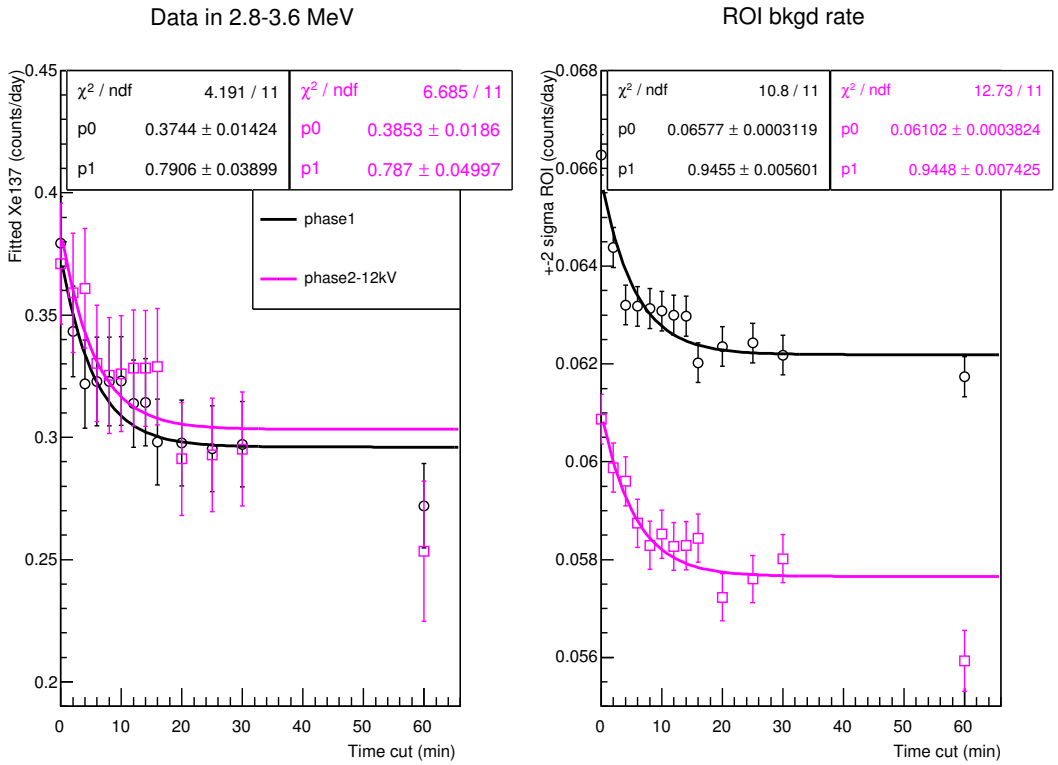

Figure 4.8 (left) Counts per day for high purity ^{137}Xe events in the data region 2.8-3.6MeV, as a function of veto time. (right) Counts per day within the ROI$\pm 2\sigma$ as a function of veto time. This was done for Phase-I+II data, denoted with circles and squares respectively. The rejection efficiency for ^{137}Xe events is $\sim 21\%$, with $\sim 6\%$ reduction in total background within the ROI$\pm 2\sigma$, for a veto time of approximately 20 min.

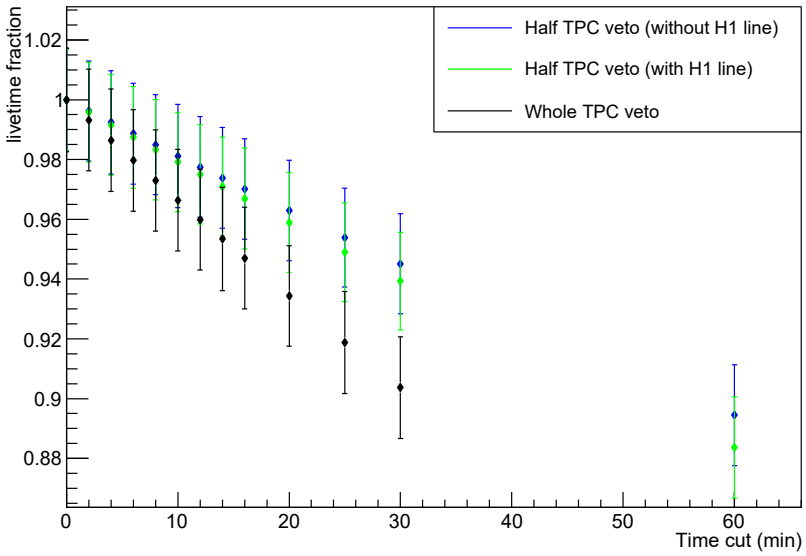

Figure 4.9 The livetime gained by vetoing half the TPC volume and removing the ^{1}H line, for Phase-I data only.

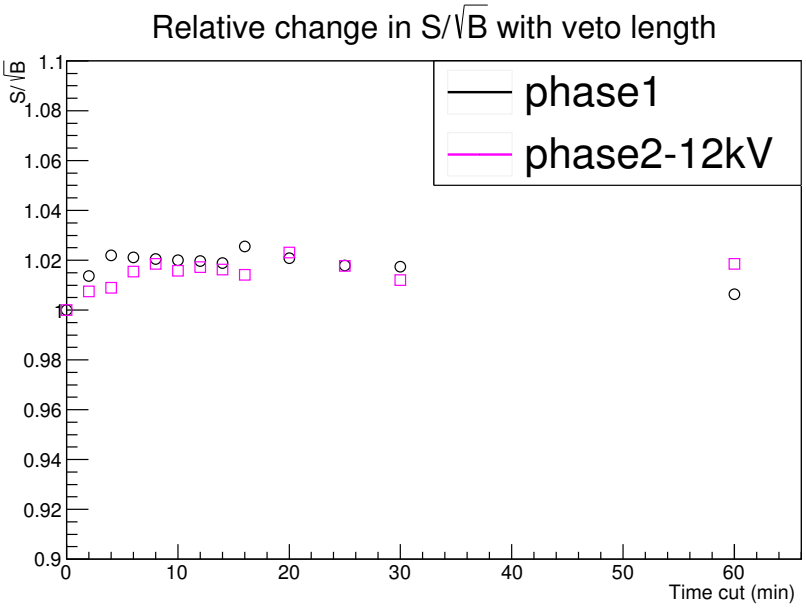

Figure 4.10 A plot of the sensitivity increase as a function of veto time, which is shown to plateau at 2%. This was done for Phase-I+II data, denoted with circles and squares respectively, and a half TPC veto. There is no significant gain in sensitivity for a large veto length, or clear optimum, which led to the physically motivated length of 5 half-lives i.e. 19.1 min.

4.4 Systematic Studies

The veto could potentially create disagreement between the data and MC, since it only affects a sub-volume of the TPC. Thus, a simple procedure has been developed to also apply the veto to MC data, such that this effect can be quantified. Once the veto is applied, the resulting background pdfs are generated, merged together, and fit to Phase-I+II data. The systematic uncertainty is calculated as the error generated in total counts within the ROI$\pm 2\sigma$. This procedure has been applied in the simple case of a half TPC veto. However, it has been developed in a general manner, so that it can also be applied in the case of a dynamic veto volume, should the need arise. The procedure for applying the veto to MC data is outlined in fig. 4.11.

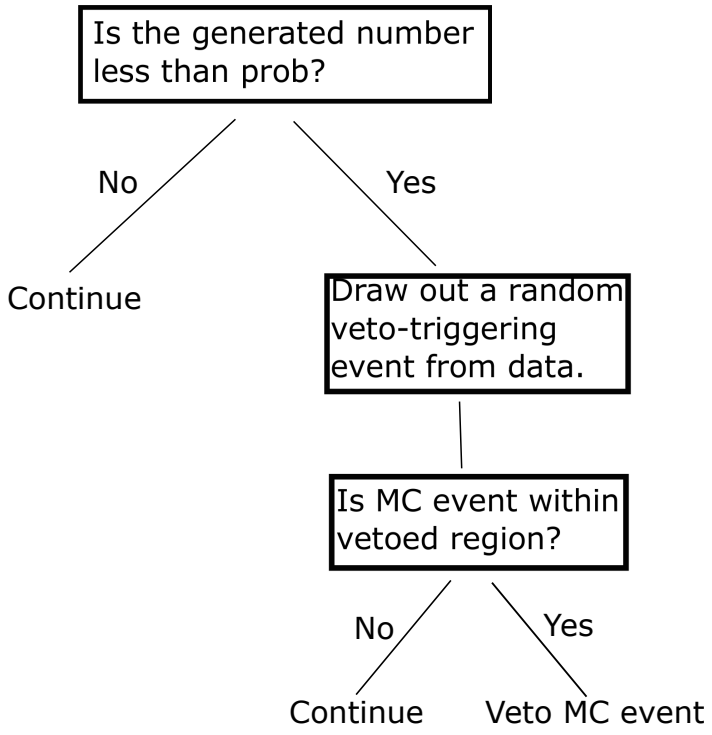

Figure 4.11 Procedure for applying the ^{137}Xe veto to MC data.

A random number is generated between 0 and 100 for every event, and compared with the user input variable called *prob*. If this number is less than *prob*, a random veto-triggering event is drawn from the data, from which the corresponding veto volume is taken. If the MC event falls within this volume, it is ignored. For a half TPC veto, this has a probability of approximately 50% [1]. Thus, the variable *prob* corresponds roughly to twice the loss in

1. This is approximate because some events may lie in both TPC halves.

livetime, in percentage. Shown in fig. 4.12 is an example of the procedure applied to SS and MS ^{232}Th MC data, with *prob* = 7, assuming a loss in livetime of 3.5%. The changes in pdf shape are, in general, quite small ($< 1\%$), barring the region where the probability density drops to 0.

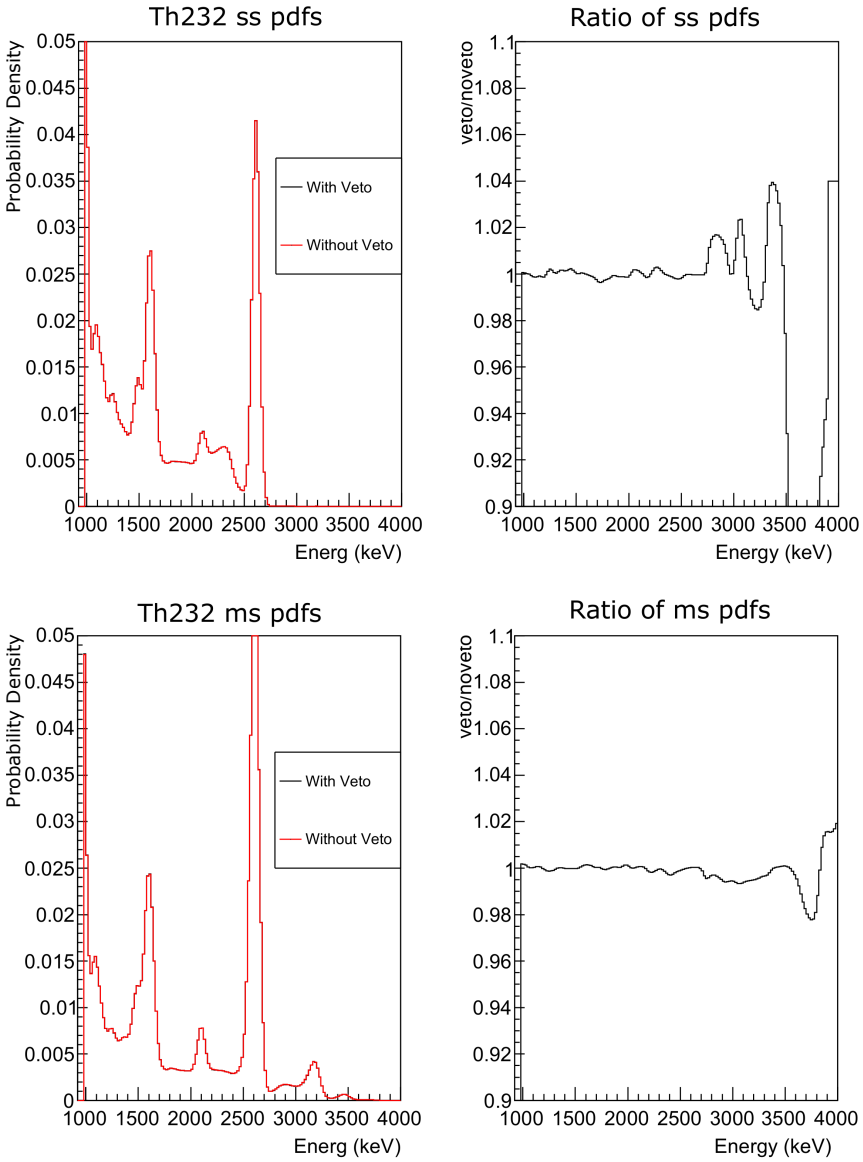

Figure 4.12 (left) Comparison between a normal ^{232}Th pdf, and a ^{232}Th pdf generated using the procedure outlined in fig. 4.11 with *prob*=7, for SS and MS events, which corresponds to a loss in livetime of $\sim$3.5%. (right) The ratio of these pdfs is provided to highlight any differences in shape.

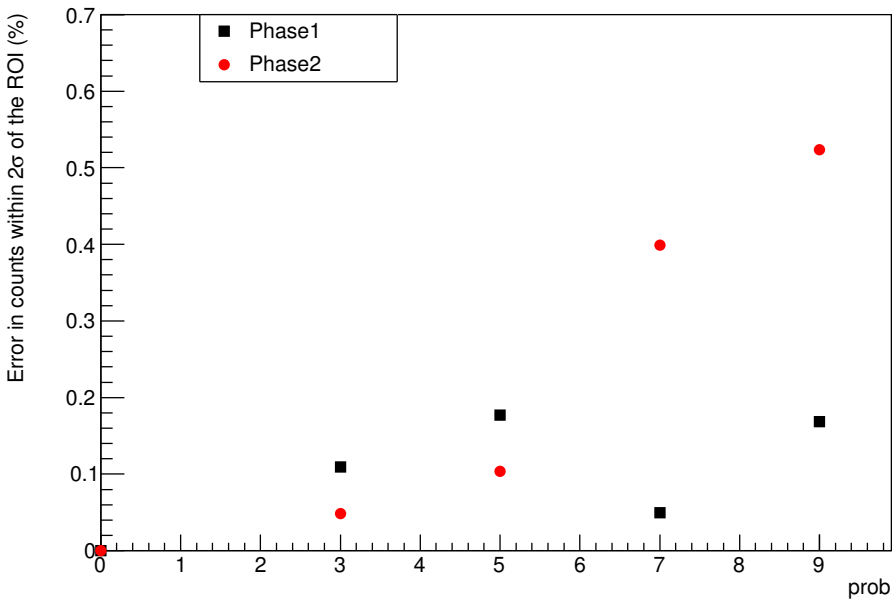

Figure 4.13 The error induced in total counts within 2σ of the ROI, for various values of *prob*.

The error induced in total counts within the ROI$\pm 2\sigma$ was calculated for various values of prob, shown in fig. 4.13. Which yielded a systematic uncertainty of 0.2% in Phase-I and 0.5% in Phase-II.

Chapter 5

Mass Spectrometry

As discussed in section 3.4, the process of Ba-tagging presents a unique opportunity to not only eliminate the backgrounds to $0\nu\beta\beta$ decay [1], but also verify the signal. The MR TOF can provide efficient and high-resolution identification of ions extracted from the TPC. This information can be used for systematic studies of the RF-only ion funnel. Once these studies are complete, the MR TOF will be used to provide secondary verification of the Ba isotope after it has been tagged in the LPT.

The presented design is based on the MR TOF used in the ISOLTRAP experiment at the ISOLDE facility [61]. This chapter explores the ways in which the original operation mode may be modified, to make it more suitable for high-resolution broad-range mass-spectrometry.

5.1 Ion Optics

The modeling of ion transport in this work is done using transfer matrix formalism, which is used to describe the effects of ion optical devices, and drift regions, on an ion's trajectory [62]. The properties of an ion's trajectory can be described at any point in its flight with the vector

$$X = \begin{bmatrix} x \\ a \\ y \\ b \\ \delta \\ t' \end{bmatrix}, \tag{5.1}$$

1. Note that this is dependent on the Ba-tagging efficiency and does not apply to backgrounds created by $2\nu\beta\beta$ decay.

where x and y are transverse displacements and $a = \frac{\partial x/\partial t}{\partial z/\partial t}$ and $b = \frac{\partial y/\partial t}{\partial z/\partial t}$ are transverse angles, all of which are relative to a reference trajectory [63]. The variable

$$\delta = \frac{K - K_0}{K_0} \tag{5.2}$$

is the deviation of an ion's kinetic energy K from the reference ion's kinetic energy K_0. Likewise, $t' = t - t_0$ is the difference in time-of-flight (TOF) of the considered ion from the reference ion [2].

Figure 5.1 Example of an arbitrary ion's trajectory through a 2D einzel lens, showing the transverse displacement x, and transverse angle a, relative to a reference ion's trajectory.

After passage through an ion optical element, the components of X can be calculated with

$$X_i = \sum_j Y_j \left[(X_i|Y_j) + \sum_k \frac{Y_k}{2} \left[(X_i|Y_jY_k) + \sum_l \frac{Y_l}{3} \left[(X_i|Y_jY_kY_l) + ... \right] \right] \right], \tag{5.3}$$

where Y_i are the components of the initial vector and $(X_i|Y_j)$, $(X_i|Y_jY_k)$ and $(X_i|Y_jY_kY_l)$ are the first, second and third order transfer coefficients [64]. The ion trajectory can then be described using a matrix equation, where the matrix elements are the transfer coefficients that map initial conditions to final. The first, second and third order matrices are 6×6, 6×6^2 and 6×6^3 etc.

In a simple 2D einzel lens example, shown in fig. 5.1, the first order transfer matrix takes the form [65]

$$\begin{bmatrix} x \\ a \end{bmatrix} = \begin{bmatrix} (x|x) & (x|a) \\ (a|x) & (a|a) \end{bmatrix} \begin{bmatrix} x_0 \\ a_0 \end{bmatrix}, \tag{5.4}$$

where δ and t' are ignored for the moment. An einzel lens consists of 3 concentric rings, in which the outer rings are held at ground potential, and the center ring is held at some

2. This parameterization is chosen over path length for convenience in time-of-flight mass-spectrometry.

dissimilar potential. This has the effect of focusing ions that pass through it.

Assuming the ions diverge radially from a point-like source, the lens can produce a parallel bunch of ions if it is tuned such that $(a|a) = 0$. This can be generalized to the 3D case, in which the optimization goal is simply [66]

$$(a|a) = (b|b) = 0, \tag{5.5}$$

where the transfer coefficients can be obtained from a fit to simulated ion data. This point-to-parallel feature will also be used for the MR TOF. The following sections will show how this simple technique can also be used to optimize other ion-optical properties, as well as discuss the principles of the MR TOF's operation.

5.2 Ion Source

An ion being accelerated by a potential energy gradient ΔU has a kinetic energy

$$K = q\,\Delta U = \frac{1}{2}\,m\,v^2, \tag{5.6}$$

hence it has a velocity

$$v = \sqrt{\frac{2\,q\,\Delta U}{m}}\,. \tag{5.7}$$

This means that in principle, the flight time for an ion species should depend only on its mass-to-charge ratio (m/q). In reality however, the ions have an initial position and velocity distribution, which causes ions with the same m/q to have different flight times.

For extraction from the LPT, the ions are placed on a potential energy slope. At the time of extraction, ions traveling in the opposite direction to the exit will first have to reverse their momentum, then re-accelerate. This creates a fundamental lower limit to the peak width Δt_{ar}, which is called the turn-around time [67]. The difference in starting position creates a spread in the kinetic energy, as ions are placed at different heights on the potential energy slope. Thus a steeper slope creates a smaller turn around time, but increases the spread in kinetic energy.

The initial spread in kinetic energy gives the ion bunch what is known as a time focus. A time focus is a point in space at which ions of the same m/q will arrive at the same time, even though they have slightly different kinetic energies. With a two-stage extraction scheme,

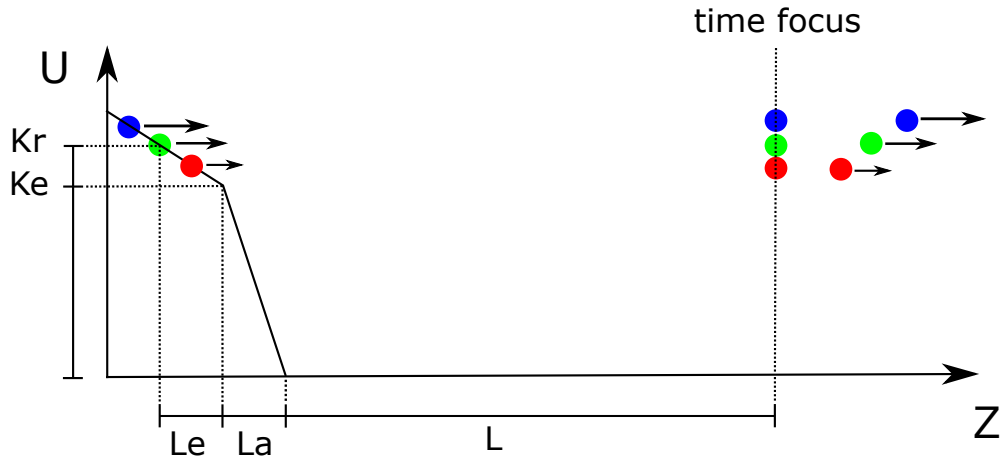

Figure 5.2 The primary time focus created using a two-stage extraction scheme. U is the potential energy, z is the distance traveled along the optical axis. The red, blue and green dots are ions that start at different points on the extraction slope. Recreated from [67].

in which two different potential energy slopes are used, the second order TOF aberration $(t|\delta\delta)$, as given by eq. (5.3), can be eliminated. The location of the primary time focus set by the two-stage extraction scheme is given by [67]

$$L = 2L_e\left(\frac{K_r}{K_e}\right)^{\frac{3}{2}} - 2L_a\sqrt{\frac{K_r}{K_e}}\frac{1}{1+\sqrt{K_e/K_r}}, \tag{5.8}$$

where the variables K_r, K_e, L_e and L_a are as shown in fig 5.2.

The ion source can be more formally characterized in terms of its emittance. The beam emittance is a conserved quantity along the trajectory of the ion bunch. It is a 6-dimensional phase-space volume, although it is typically projected onto a single position and momentum plane e.g. (x, p_x). However, instead of the phase-space area, the trace-space area is often used for convenience since it is transverse to the direction of motion. Assuming x and y are the transverse coordinates, the coordinate system (x,x',y,y') where $x' = \frac{p_x}{p_z}$ and $y' = \frac{p_y}{p_z}$ is used. The trace-space emittance is defined as

$$\varepsilon = \sqrt{\langle x^2\rangle\langle x'^2\rangle - \langle xx'\rangle^2} \tag{5.9}$$

and is usually expressed in units of mm·mrad [68].

5.3 Multiple-Reflection Time-of-Flight Mass-Spectrometry

In general, the goal of mass spectrometry is to shift the time focus onto the detector plane in a way that maximizes the mass resolution. Using eq. (5.7) the TOF can be expressed simply as

$$t = \frac{L}{v} \propto \sqrt{\frac{m}{q}} = \alpha\sqrt{\frac{m}{q}}, \tag{5.10}$$

and thus the mass-resolving power is defined as

$$R \equiv \frac{m}{\Delta m} = \frac{t}{2\Delta t}\ , \tag{5.11}$$

where Δt is the TOF spread of the ion bunch. Ideally, Δt should be comparable to the turn around time Δt_{ar} and t should be as long as possible. There are multiple ways to extend the ion's flight path, as is discussed in [61]. For this work, ion bunches are to be trapped between two coaxial electrostatic mirrors and reflected between them for N turns. A reflection through an electrostatic mirror can be used to shift the time focus position, by altering the path lengths of ions with slightly different kinetic energies [69]. This allows the time focus to be shifted from the primary position shown in fig. 5.2, to a more desired location. This is an extremely useful feature, and it will be taken full advantage of.

As mentioned in the chapter's preamble, the McGill MR TOF design is based on an existing design used in the ISOLTRAP experiment. This group has reported mass resolving-powers of $m/\Delta m = 100,000$ and above [9]. The design consists of two coaxial electrostatic mirrors, that each contain six electrodes, placed on either side of a drift tube. An overview of the configuration is shown in fig. 5.3, the mirrors and drift tube are collectively referred to as the analyzer. The mirror electrodes are held at fixed voltages, during ion injection the drift tube is also held at some potential. In this scenario, ion bunches have enough kinetic energy to pass through the mirrors and consequently, the MR TOF. However, the drift tube's potential is switched to ground as the ions pass through it; the ions no longer have enough energy to pass through the mirror and are trapped, shown in fig. 5.4. This is referred to as the in-trap lift method.

As ion species begin to separate, the lighter and therefore quicker ions will begin to overlap the heavier ions. As such, the MR TOF has an unambiguous mass range that deteriorates rapidly with an increasing number of turns N. For the in-trap lift method, this range can be expressed as [66]

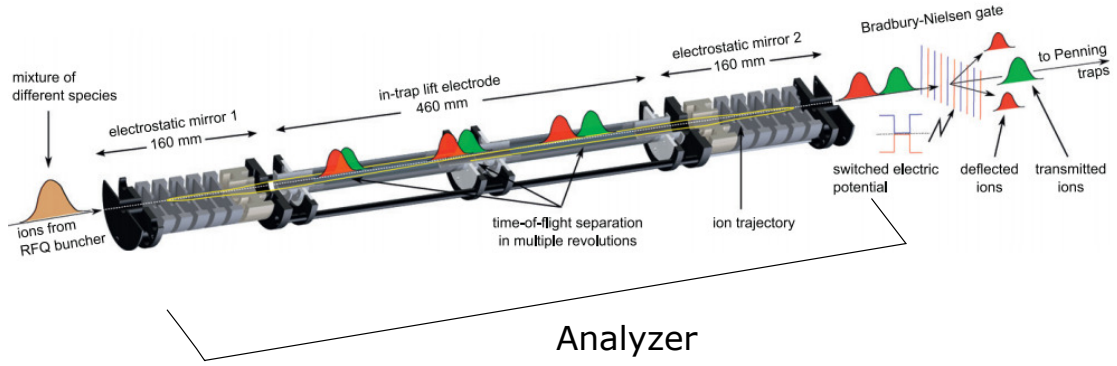

Figure 5.3 Overview of the MR TOF used in ISOLTRAP. Ion bunches are trapped between coaxial electrostatic mirrors. Ion species will begin to separate by their masses since they have different velocities. Each mirror consists of 6 electrodes, and they are placed on each end of the drift tube. Reproduced from [9].

$$\frac{(m/q)_{\max}}{(m/q)_{\min}} = \left(\frac{N+1}{N}\right)^2, \tag{5.12}$$

also displayed in fig. 5.5.

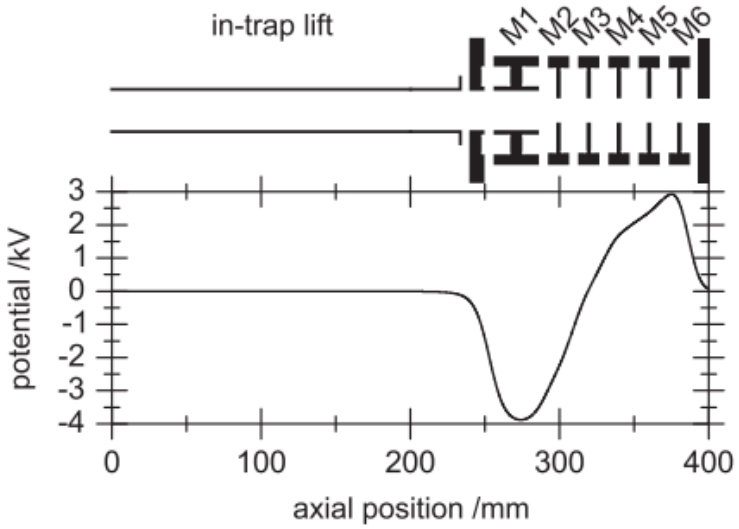

Figure 5.4 The potential energy along the MR TOF optical axis. Ions are injected by switching the drift tube potential to ground, such that they have kinetic energy less than 3 keV. Typically M1 and M2 are used for steering and are set to a negative bias, M3-6 create a potential barrier. Reproduced from [9].

For each reflection only the first order dispersion coefficient between kinetic energy and TOF is modeled for ISOLTRAP. The resolution given by eq. (5.11) was modeled as

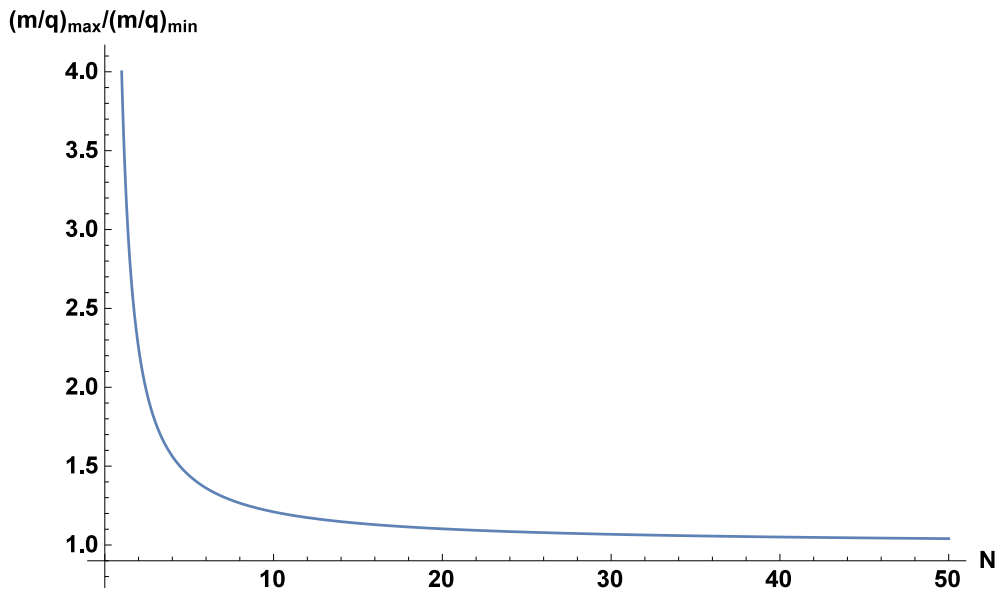

Figure 5.5 The unambiguous mass range for a coaxial MR TOF as given by eq. (5.12) as a function of turn number N.

$$R = \frac{t_s + nT_0}{2\sqrt{\Delta t_{ta}^2 + (\Delta t_s - nT_0(\partial\delta_T/\partial\delta_E)\Delta\delta_E)^2}}, \tag{5.13}$$

where t_s is the TOF from the primary time focus to the detector plane, T_0 is the revolution time and Δt_{ta} is the turn-around time [9]. The dispersion relation was measured as $(\partial\delta_T/\partial\delta_E)\Delta\delta_E \approx 5\times10^{-6}$. In the limiting case that this dispersion approaches 0, the MR TOF is deemed isochronous, meaning there is no difference in the TOF resulting from a slight difference in kinetic energy. For a flight time of 30 ms the MR TOF has reported a mass-resolving power of $\frac{m}{\Delta m} = 2\times10^5$ [9]. If the number of turns is changed however, the device must be re-tuned, making it difficult to adjust the unambiguous mass range. It is in principle possible to disentangle overlapping mass spectra [66], but this is once again facilitated by a quickly adjustable turn number. The next section will explore a method by which the unambiguous mass range can be adjusted, without having to re-tune the MR TOF.

5.4 Optimization for Turn Independent Operation

As shown in fig. 5.5, the unambiguous mass range drops rapidly as a function of turn number. If the MR TOF is to be used for broad-range mass measurements, it would be useful to switch quickly between low turn numbers for the desired mass range. As mentioned earlier, it would

be preferable for the MR TOF settings to remain the same for any turn number.

One method of doing this involves the setting an intermediate time focus. The primary time focus is shifted into the center of the analyzer with the first reflection. This time focus is then shifted onto a detector with the last reflection. The first and last reflections are thus referred to as Time Focus Shift (TFS) reflections. The procedure is outlined graphically in fig. 5.6.

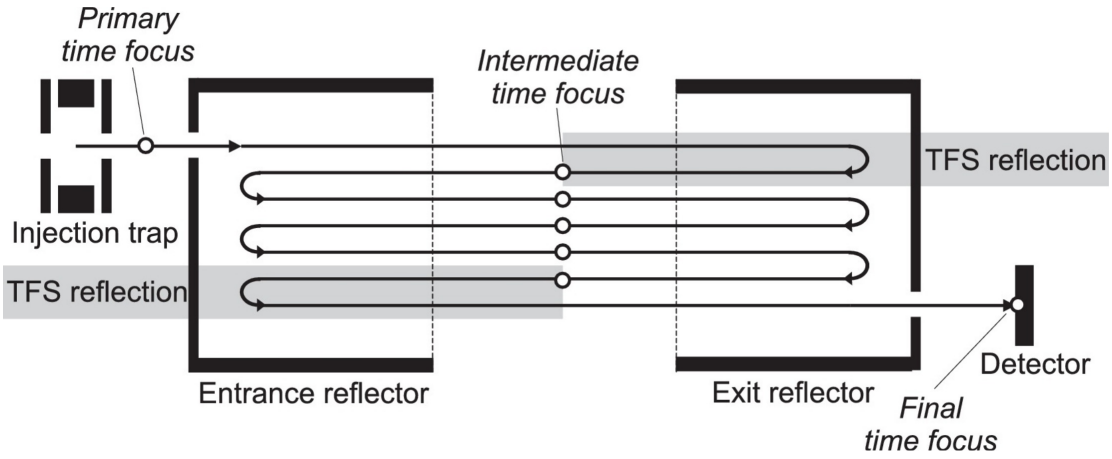

Figure 5.6 An example of how the time focus can be shifted using the first and last reflections of the MR TOF, they are referred to as the TSF reflections. The setting of an intermediate time focus allows for the MR TOF's settings to be independent of the number of reflections. Reproduced from [70].

This placement of an intermediate time focus allows the MR TOF settings to decouple from the number of turns. The first and last reflections will have longer focal lengths and every reflection between them is isochronous. To change the focal length it is only necessary to adjust the M5 and M6 electrodes, but most importantly M6 as it defines the position of the ion's turning point. The values of M5 and M6 will be lower on the first and last reflections as the longer focal length requires a shallower potential distribution. An example potential distribution is shown in fig. 5.4.

The optimization goals can be expressed in terms of the transfer matrix coefficients given by eq. (5.3). After a reflection the ion properties can be expressed as [66]

$$x = (x|x)x_0 + (x|a)a_0 + (x|x\delta)x_0\delta + (x|a\delta)a_0\delta + ... \tag{5.14}$$

$$a = (a|x)x_0 + (a|a)a_0 + (a|x\delta)x_0\delta + (a|a\delta)a_0\delta + ... \tag{5.15}$$

$$y = (y|y)y_0 + (y|b)b_0 + (y|y\delta)y_0\delta + (y|b\delta)b_0\delta + ... \tag{5.16}$$

$$b = (b|y)y_0 + (b|b)b_0 + (b|y\delta)y_0\delta + (b|b\delta)b_0\delta + ... \tag{5.17}$$

$$\begin{aligned} t' =& (t|\delta)\delta + (t|xx)x_0^2 + (t|xa)x_0a_0 + (t|aa)a_0^2 + (t|yy)y_0^2 + (t|yb)y_0b_0 \\ &+ (t|bb)b_0^2 + (t|\delta\delta)\delta^2 + (t|\delta\delta\delta)\delta^3 + (t|\delta\delta\delta\delta)\delta^4 + (t|xx\delta)x_0^2\delta \\ &+ (t|xa\delta)x_0a_0\delta + (t|aa\delta)a_0^2\delta + (t|yy\delta)y_0^2\delta + (t|yb\delta)y_0b_0\delta + \\ &+ (t|bb\delta)b_0^2\delta + ... \end{aligned} \tag{5.18}$$

The measurement point is taken to be the mid plane between the coaxial mirrors, and the variables with subscript 0 are initial conditions before any reflections. To tune to parallel-to-point conditions the conditions

$$(x|x) = (y|y) = 0 \tag{5.19}$$

must be met. Due to the MR TOF's symmetry this will automatically set

$$(a|a) = (b|b) = 0. \tag{5.20}$$

The second order position and angular effects on the time focus can also be tuned simultaneously to

$$(t|xx) = (t|aa) = (t|yy) = (t|bb) = 0. \tag{5.21}$$

After one full turn in the analyzer there will be

$$(x|a) = (a|x) = (y|b) = (b|y) = 0, \tag{5.22}$$

which also fulfills

$$(t|xa) = (t|yb) = 0. \tag{5.23}$$

This automatically leads to the vanishing of

$$(x|\delta x) = (x|a\delta) = (a|x\delta) = (a|a\delta) = (y|y\delta) = (y|b\delta) = (b|y\delta) = (b|b\delta) = 0. \tag{5.24}$$

Since the first and last reflections are necessarily different from all intermediate reflections, it becomes natural to inject and eject ion bunches by pulsing down the mirrors, as opposed to

using an in-trap lift. However, this has the negative side-effect of reducing the accepted mass range slightly, it shall be shown that the decrease is very minor. Suppose t_a is the time of flight for one turn in the analyzer. Then

$$t_{\text{inj}} = \lambda_{\text{inj}}\, t_a \tag{5.25}$$

is the TOF from the ion source to the beginning of the exit mirror, and

$$t_{\text{mir}} = \lambda_{\text{mir}}\, t_a \tag{5.26}$$

is the TOF spent in the mirror for a single reflection, see fig. 5.7 for clarification. The mass range can then be expressed as

$$\frac{(m/q)_{\max}}{(m/q)_{\min}} = \left(\frac{N_a + \lambda_{\text{inj}}}{N_a + \lambda_{\text{inj}} - (1 - \lambda_{\text{mir}})}\right)^2, \tag{5.27}$$

where both λ_{mir} and λ_{inj} are fairly simple coefficients to measure using simulation [66].

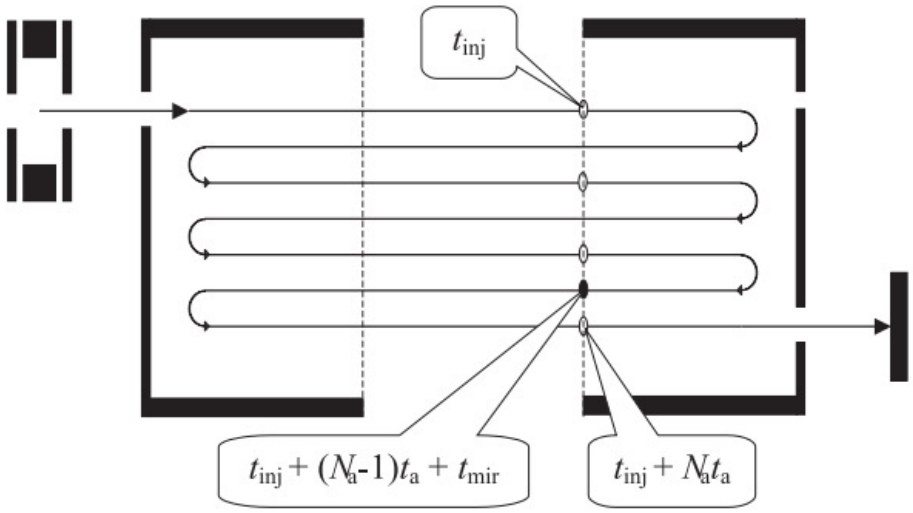

Figure 5.7 A diagram used to quantify the effect of pulsing the mirror voltages to inject/eject ions on the accepted mass range. Reproduced from [70].

5.5 The Genetic Algorithm

Optimization of the MR TOF requires an optimization of the einzel lens, the mirror electrodes and both time focus shift reflections. This totals to 11 voltages which need to be optimized to fulfill the goals outlined in eqs. (5.19)-(5.24). Typically the Nelder-Mead (NM) method

is used in an environment such as SIMION to optimize electrode potentials. However, this method will only yield a local minimum, and only with a smoothly varying objective function. To explore the space of local minima, it is better to use a stochastic algorithm as they are more robust and inherently random. The Genetic Algorithm (GA) has been used to optimize an electrostatic mirror with great precision in another application [71], and has been adapted for this work.

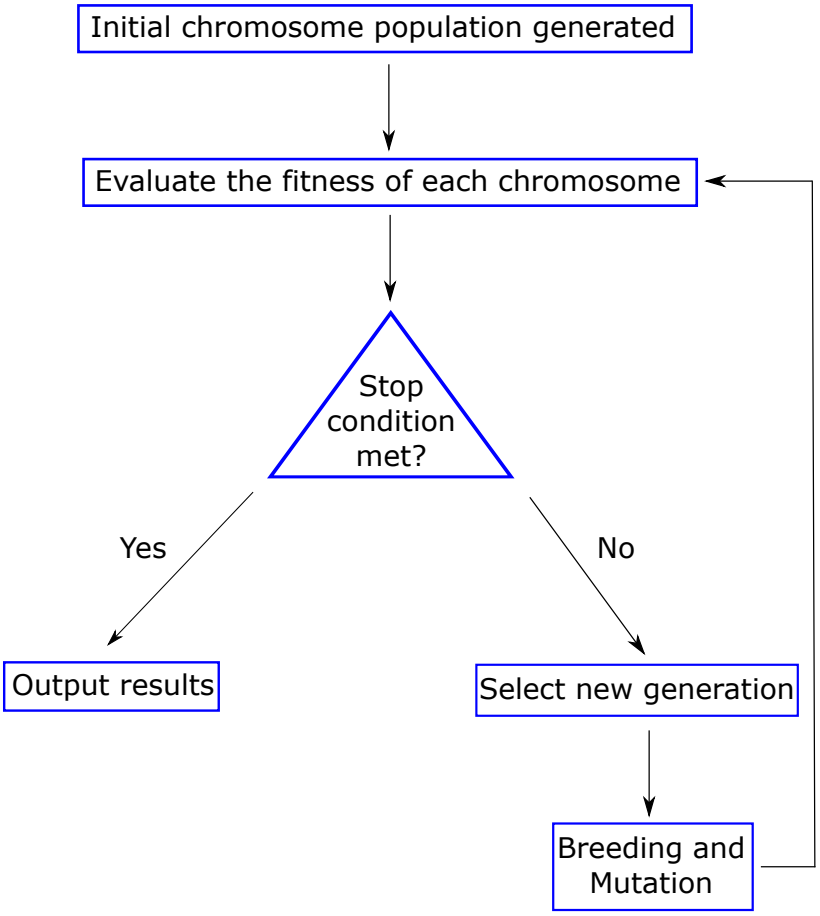

Figure 5.8 Flow diagram for the Genetic Algorithm.

The procedure for the GA, accompanied by a flow-diagram in fig. 5.8, is as follows:

— The GA starts with a population of random solutions, where each solution is a vector of voltages required for operation. Each voltage must fall within user defined limits and the population size is also user defined. In GA nomenclature each solution is called a chromosome.

— Each chromosome in the population is then tested and assigned a fitness. How the fitness is assigned can vary greatly depending on the application. In this work a linear combination of the transfer coefficients to minimize was used as a fitness metric.
— After each chromosome has been tested and assigned a fitness, the new generation is selected. Fitter chromosomes will have a higher probability of breeding and creating child chromosomes. Unfit chromosomes have a higher probability of being removed from the population, as the total population size stays fixed.
— There are many methods of breeding two chromosomes. The most popular is recombination, whereby the values from each parent are mixed in some way to form the child. In this work the average is taken.
— There is also a mutation step, which randomly changes some chromosomes in order to boost the population diversity.

The GA is useful for exploring the extraordinarily large parameter space, since it is a guided stochastic process, however it seems to be slower in performance compared to an algorithm such as NM. Together, they make a powerful combination, with the GA searching out the most promising local minima and NM fine-tuning the voltages to find the optimum.

5.6 Design and Simulation

The ions used to optimize the MR TOF have been produced through simulation of the LPT, using SIMION 8.1 [72], by Yang Lang at TRIUMF as discussed in section 3.4.2. They have been simulated with an average kinetic energy of $\sim$ 1200 eV and a FWHM of $\sim$ 23 eV, they have a transverse emittance of $\varepsilon_{\mathrm{rms}}^{\mathrm{trans}} \sim 0.4$ mm·mrad, their phase-space diagrams are shown in see figs. 5.9 and 5.10.

The MR TOF, as well as the vacuum chamber it will be housed in, have been drawn in Solid Works and also simulated in SIMION 8.1. The vacuum chamber is comprised of two 6-way CF crosses with 8" flanges, two 8" CF nipples and an 8" spherical Hexagon. The spherical hexagon will provide HV feed throughs for the analyzer, the vacuum chamber overview is shown in fig. 5.11.

The first 6-way cross houses ion optical elements to guide the ion bunch into the analyzer. A channeltron detector will be placed on a linear actuator, so that it can move in and out of the ion bunch trajectory. This is a diagnostic measure, required for tuning and to measure the transmission efficiency. The optics consist of four sets of x-y steerers and an einzel lens.

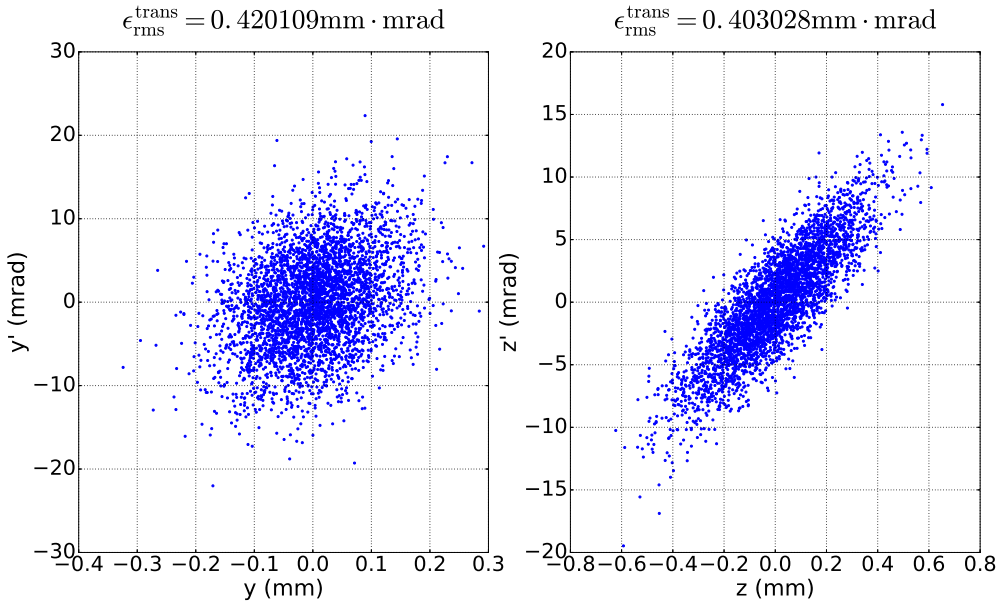

Figure 5.9 The transverse emittance of a simulated ion bunch, with $\varepsilon_{\mathrm{rms}}^{\mathrm{trans}} \sim 0.4$ mm.mrad.

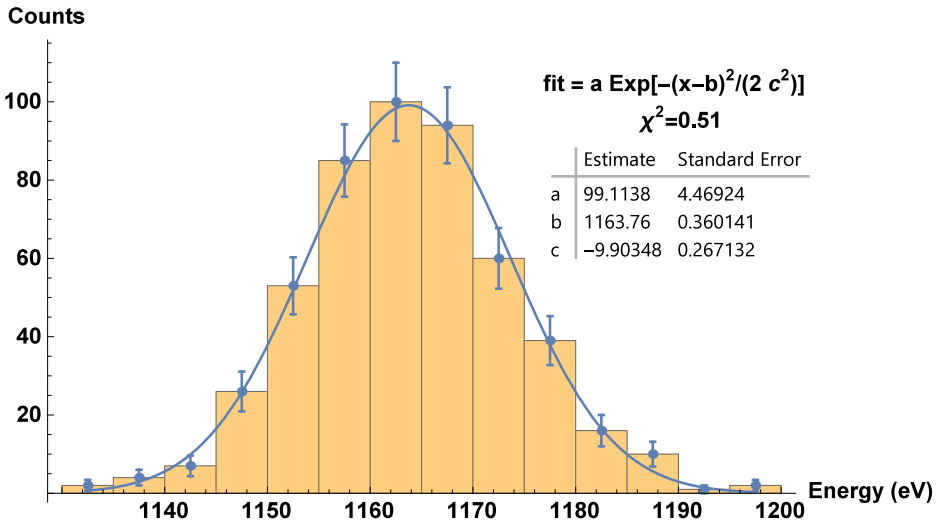

Figure 5.10 Energy spectrum of 1000 simulated ions ejected from the LPT. The ions have an average kinetic energy of 1163 eV and FWHM of 23 eV.

Two sets of steerers come before the lens and two more come after, shown in fig. 5.12. A turbomolecular pump will be connected to each 6-way cross to achieve the required vacuum. Custom double-sided flanges will be used to support both ends of the MR TOF.

After passing through the ion optics, the ion bunch enters the analyzer, a close up of which is shown in fig. 5.13. The dimensions of the mirror electrodes and drift tube are the same

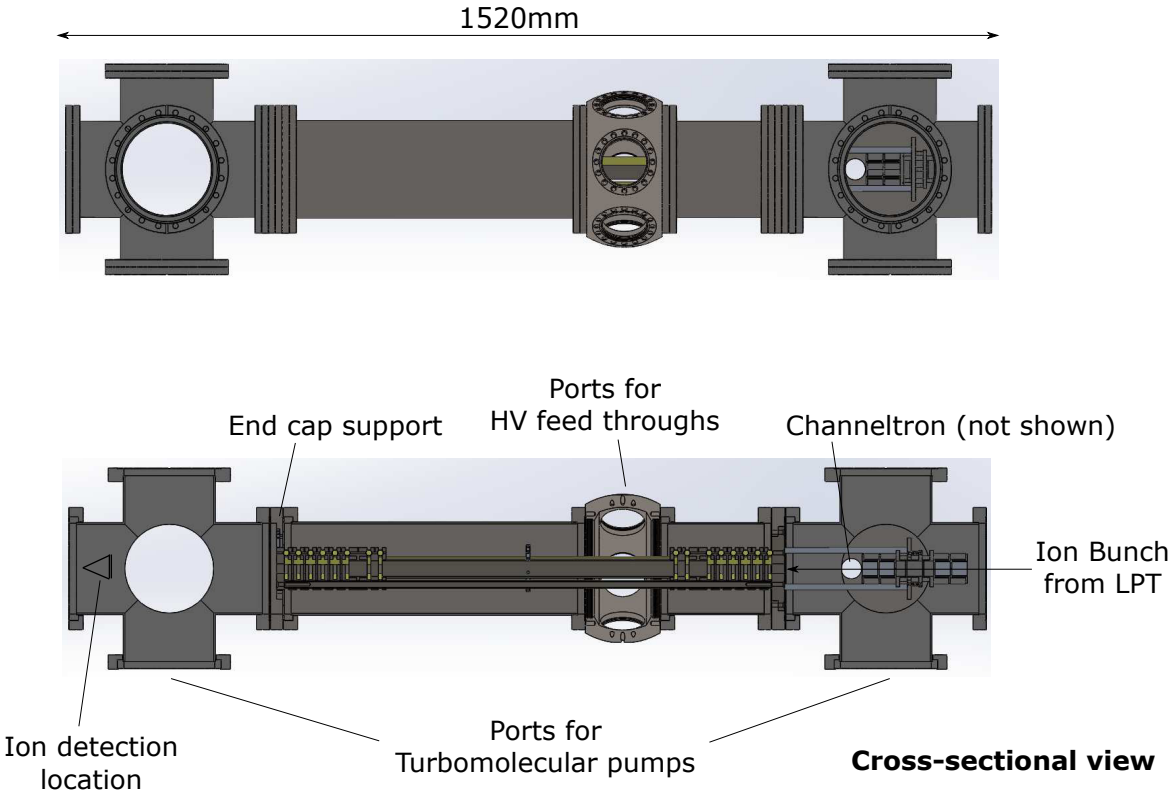

Figure 5.11 (top) The vacuum chamber for the MR TOF, designed in the Solid Works program. This consists of two 6-way CF crosses with 8" flanges, two 8" CF nipples and an 8" spherical Hexagon. (bottom) A cross-sectional view of the MR TOF. Ion bunches will enter from the LPT on the right, after which they immediately pass through four sets of x-y steerers and an einzel lens. A channeltron will be mounted on a linear actuator, as a diagnostic tool for ion bunches exiting the optics.

as those used for ISOLTRAP. However, a mass-selector has been mounted onto the center of the drift tube, to eject unwanted ions. Three pins will be protrude into the center of the tube and can be pulsed to destabilize passing ions, shown in fig. 5.14. Placement in the center of the drift tube is sensible for two reasons. Firstly, it is the same position as the intermediate time focus, hence ions from a particular mass species will be arriving at the same time. Secondly, there will be a higher density of ions in the mirrors since they have to reverse their momentum there. Lowering the ion density allows the mass selector to more precisely eject unwanted species. There are 6 mirror electrodes, with M1 and M2 used for steering and M3-6 to form a potential barrier as in ISOLTRAP. An overview of the analyzer is shown in 5.13.

The MR TOF has been optimized on a random selection of simulated ions from the LPT. The ions are injected/ejected by pulsing down the entrance and exit mirrors. The MR TOF also

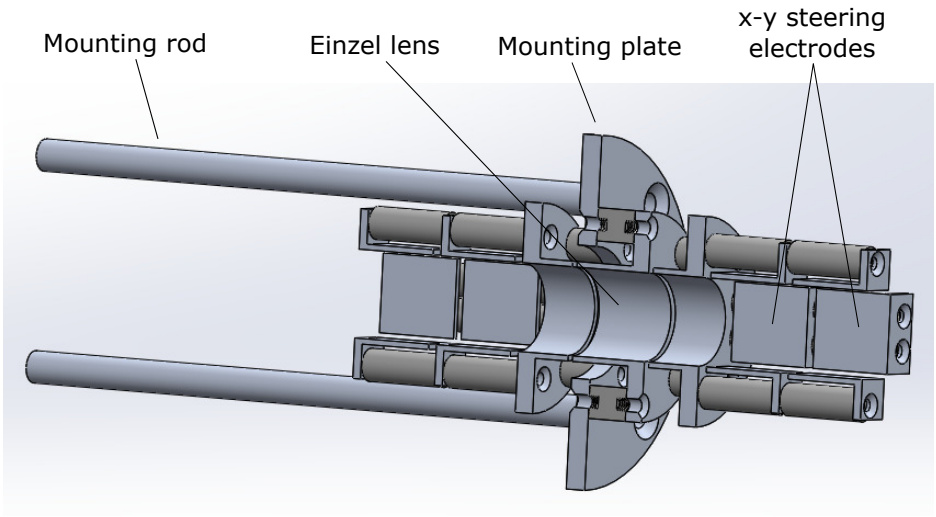

Figure 5.12 A close up view of the ion optical elements that will be used to focus the ion bunch into the mass analyzer.

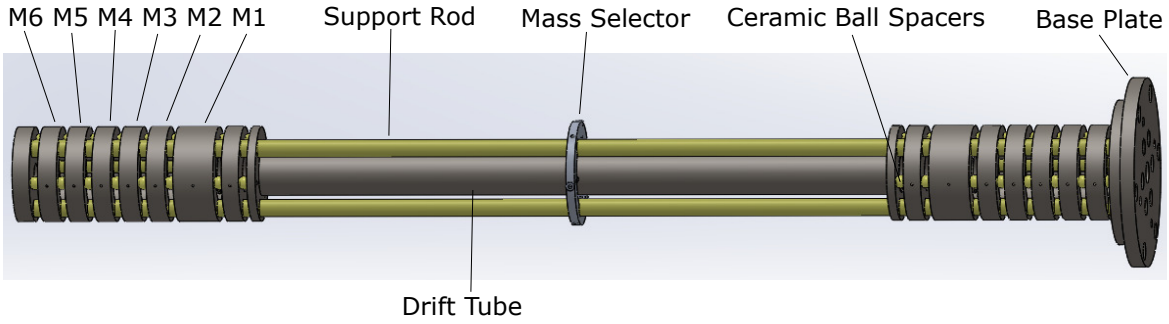

Figure 5.13 The MR TOF analyzer, consisting of two electrostatic mirrors on either side of a central drift tube. The mirror and tube dimensions are the same as those used for the ISOLTRAP MR TOF. A mass selector is mounted in the center of the drift tube to eject unwanted ions.

operates in a turn-independent mode, as discussed in section 5.4. A cross-sectional view of the MR TOF potential array is shown in fig. 5.15.

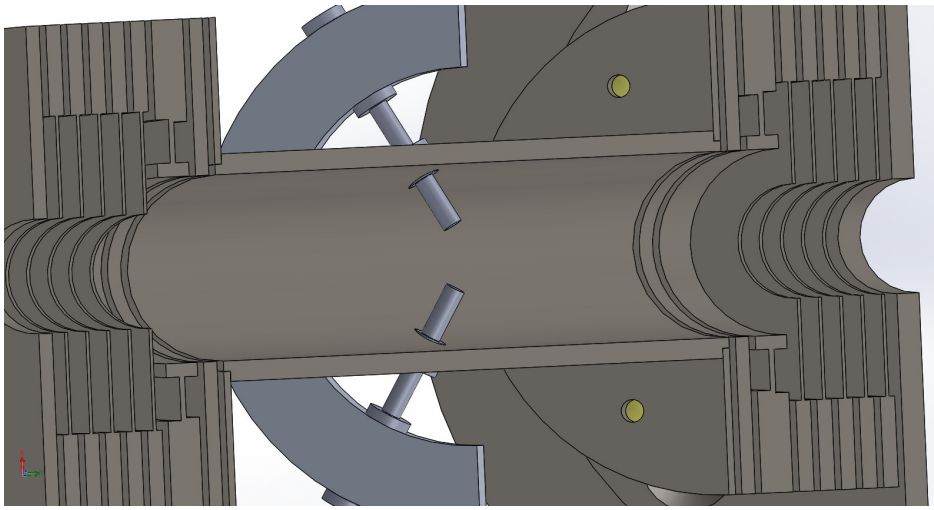

Figure 5.14 A close up view of the mass selector. Three electrodes will protrude into the drift tube, whilst being insulated from it by ceramic washers. These electrodes can then be pulsed to destabilize passing ions.

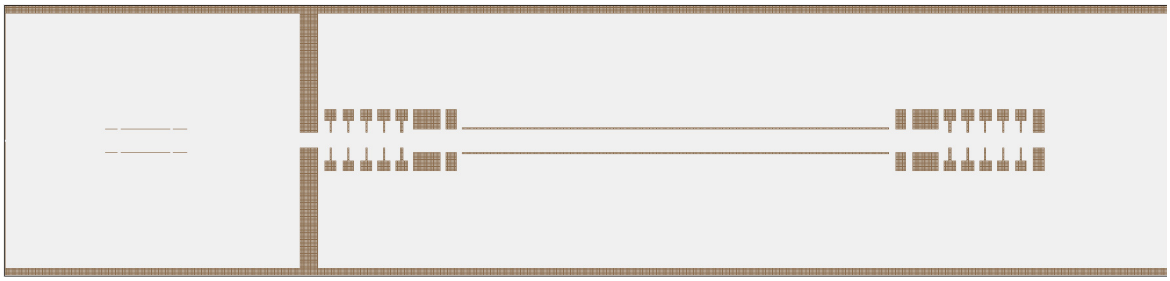

Figure 5.15 The MR TOF SIMION potential array for optimization of the TFS reflections and other analyzer voltages.

5.7 Simulation Results

To calculate the MR TOF mass acceptance using eq. (5.27), λ_{inj} and λ_{mir} were extracted from simulations. They were measured to be $\lambda_{inj} = 0.63$ and $\lambda_{mir} = 0.21$. The slightly reduced mass range is shown in fig. 5.16. It is clear that the effect on the mass range is relatively insignificant.

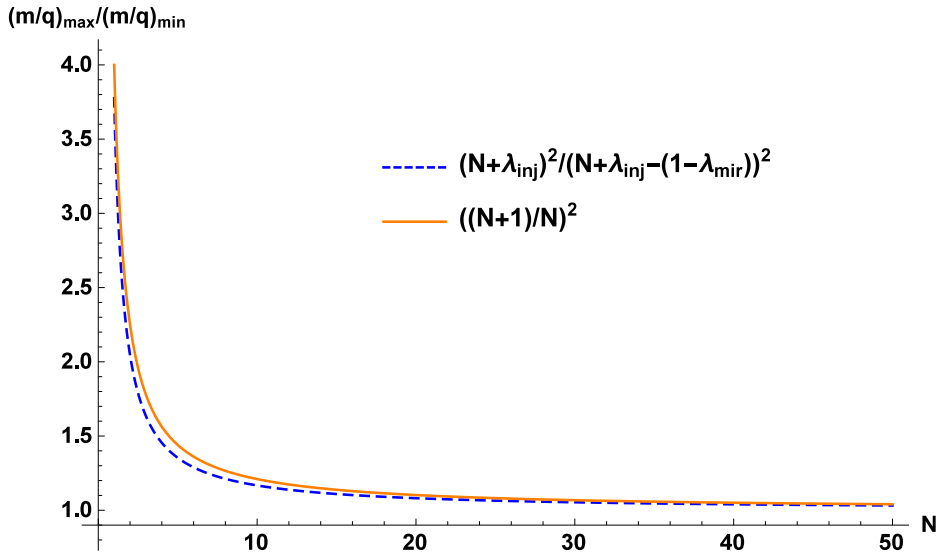

Figure 5.16 Comparison of the mass range allowed by drift tube injection/ejection and the mass range allowed by pulsing the mirror voltages, as a function of turn number.

The MR TOF has been optimized for turn independence using the Genetic and Nelder-Meade algorithms. Where the Genetic algorithm is used to roughly search the large parameter space, and Nelder-Meade is used to fine-tune the best results. The optimal voltages thus far are given in table 5.1.

	M1	M2	M3	M4	M5	M6
First reflection	-1808.406	-1147.855	389.830	519.658	1132.258	1377.908
Intermediate reflections	-1808.406	-1147.855	389.830	519.658	1141.007	1504.669
Last reflection	-1808.406	-1147.855	389.830	519.658	1123.676	1374.785

Table 5.1 Voltage sets for the MR TOF to operate with turn independence. Only M5 and M6 differ amongst reflections, while M1-M4 are held fixed.

To calculate the mass-resolving power, the TOF spectrum of 1000 ions was simulated for a varying number of N turns. For each N, the TOF spectrum was fit with a Gaussian function

for a measurement of the mean and FWHM which are used as t and Δt, from which the resolving-power can be calculated using eq. (5.11) [61]. An example spectrum is given in fig. 5.17 for 50 turns. The mass resolving-power reaches a maximum in the region of 40-50 turns with $m/\Delta m \sim 70000$, shown in fig. 5.18. After which the broadening of the intermediate time focus due to the $(t|\delta\delta)$ and $(t|\delta\delta\delta)$ coefficients will begin to outweigh the gain in flight time. Dependence of the TOF spectrum on the higher order energy dispersion coefficients will only manifest after significant flight time. As a result ions must be flown for many reflections to ensure the stability of the intermediate time focus during optimization. The resolution can potentially be improved through finer control of these coefficients, although this remains to be shown.

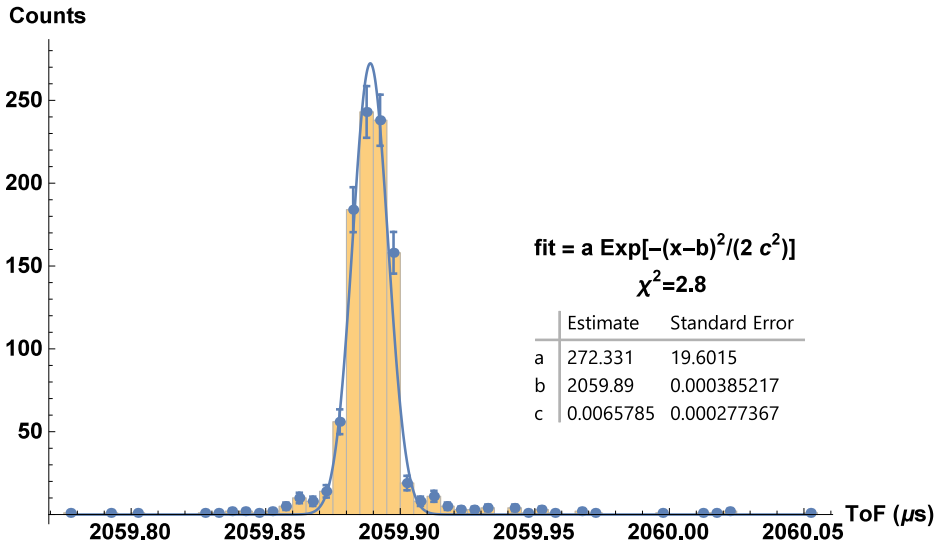

Figure 5.17 A gaussian function fitted to the TOF spectrum for 1000 ions flown for 50 turns. The peak has a FWHM of 15.5 ns, allowing for a mass resolving-power in the region of $m/\Delta m \approx 65000$.

The mass selector was tested with a bunch of 200 ions. A 200 ns pulse was sent to the electrodes, as the ions crossed the center of the analyzer. Biasing two electrodes to -150V and one electrode to 150V alters the angle at which ions enter a reflection. This results in a trajectory that collides with the wall of the drift tube after only one reflection, shown in fig. 5.19.

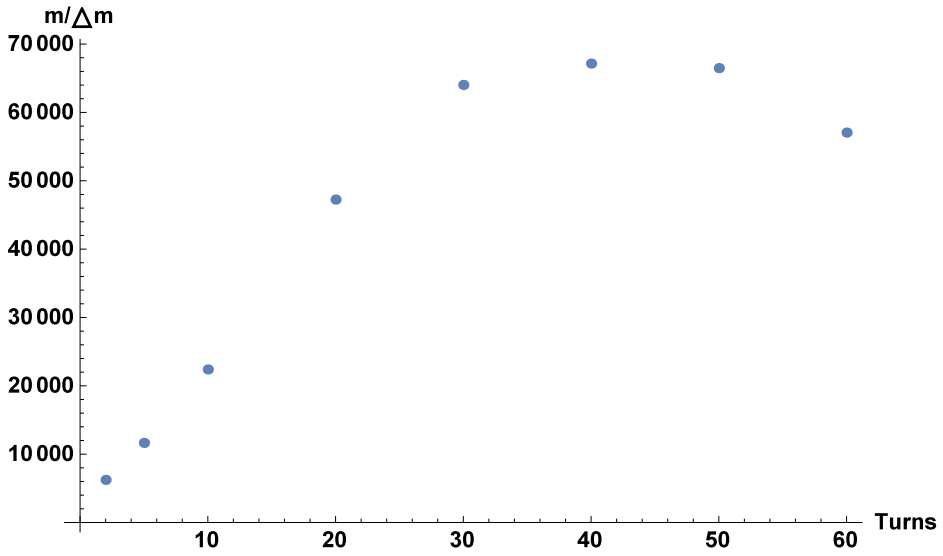

Figure 5.18 The mass resolving-power as a function of the number of turns N, calculated using $m/\Delta m$= mean/2FWHM, obtained from a Guassian fit to the TOF spectra.

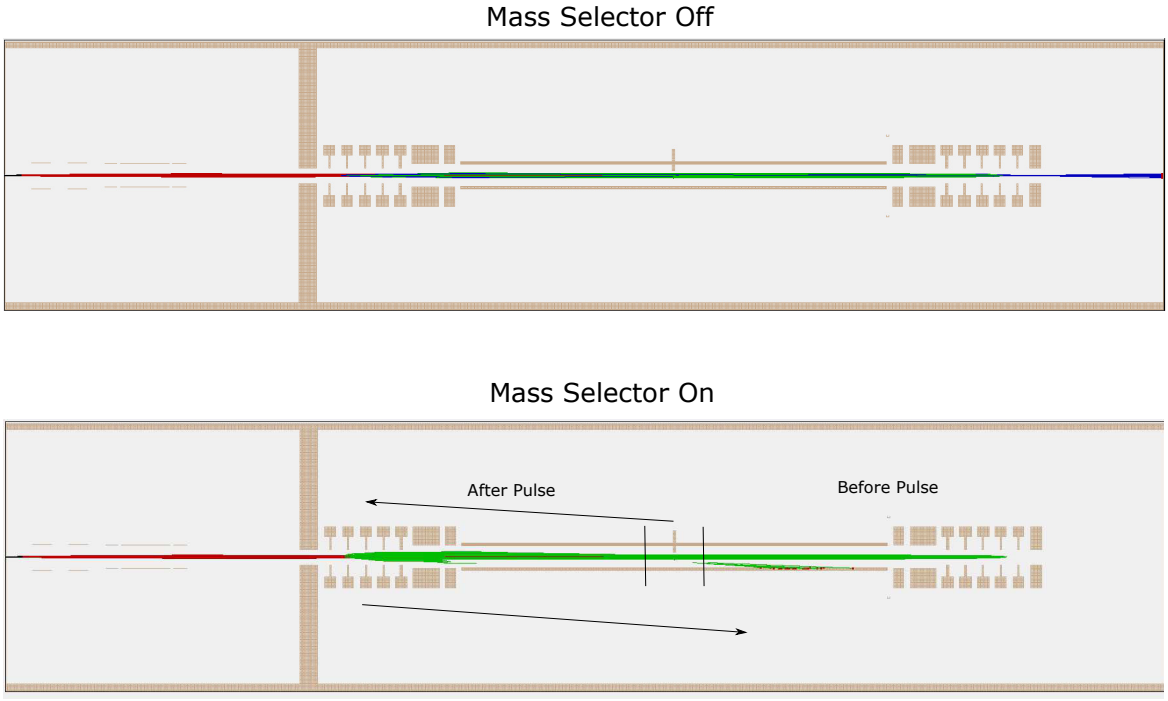

Figure 5.19 The mass selector is pulsed in a 200 ns window when ions pass by. This alters the ion's entrance angle into the electrostatic mirror resulting in a subsequent collision with the drift tube.

Chapter 6

Summary and Conclusions

The observation of $0\nu\beta\beta$ decay would demonstrate the Majorana nature of the neutrino. This has potentially far-reaching implications, from the development of massive neutrino theories that go beyond the Standard Model, to providing a measurement of the effective Majorana neutrino mass. It is clear that experiments will have to employ advanced methods of background reduction, in order to boost their sensitivity and discovery potential. This work explored two very different methods of accomplishing this, first with the ^{137}Xe software veto for EXO-200, then with the Ba-tagging project for nEXO.

The ^{137}Xe veto, discussed in Chapter 4, is a series of software scripts, that combine to form an algorithm for rejecting the background created by ^{137}Xe decay. The algorithm identifies neutron capture on ^{136}Xe, localizes it to half of the TPC volume, then removes that volume from the analysis for 19.1 min. Based on the results given in [36], it was expected that this approach would perform far better than it has so far. The initial results with the Run 2abc datasets were promising, and saw a 40% rejection of ^{137}Xe counts. However, when applied to the full Phase-I+II datasets, the rejection efficiency dropped dramatically. The ^{137}Xe rejection efficiency is $21 \pm 4\%$ for Phase-I and $21 \pm 5\%$ for Phase-II with a loss in livetime of 3.5% and 2.8% respectively, it is currently unclear why there is a discrepancy in livetime loss, as such it warrants further investigation. This results in a $\sim 2\%$ increase in the experiment's sensitivity, and introduces a systematic error in fitted counts within the ROI$\pm 2\sigma$ and 0.2% in Phase-I and 0.5% in Phase-II.

The MR TOF has been designed and simulated for the Ba-tagging project, where it will be used to conduct systematic studies of the ion extraction technique, and to potentially provide further identification of the Ba ion. Simulation of the MR TOF has shown that it is able to operate effectively using settings that are independent from the number of turns. This is

achieved by placing an intermediate time focus in the center of the analyzer, which is shifted onto the detector upon ejection. Ion bunches are injected and ejected from the MR TOF by pulsing down the mirror voltages. This incurs a slight reduction to the accepted mass range, although this effect is relatively negligible as shown in fig. 5.16. The simulation shows a possible resolving-power of $m/\Delta m \approx 70000$ with only 2 ms of flight time, using simulated ions from the LPT. The resolving-power of the MR TOF is comparable to that of the MR TOF used for TITAN at TRIUMF, which also uses the turn independent mode, and was measured to be $m/\Delta m \approx 50000$ [73]. With its current resolving-power the MR TOF is able to separate the ^{136}Xe and ^{136}Ba isotopes, however, their spectra will overlap considerably. In order to separate a single ^{136}Ba ion from ^{136}Xe, a mass-resolving power exceeding $m/\Delta m = 100000$ is required. Thus the original operation mode holds the advantage in this regard. However, the turn independent mode allows for an easily adjustable unambiguous mass range, with a relatively high resolution for low turn number, which makes it more suitable for systematic studies of the RF-only ion funnel. It is possible that the MR TOF may achieve a greater resolving-power, even while operating in the turn independent mode, through a better optimization method. Given the extraordinary complexity of the system it may be fruitful to explore the avenue of machine learning. This could be useful not only for the MR TOF, but also for other complex ion-optical devices.

Lastly, the mass selector has shown preliminary success and was able to terminate contaminant-ions within only one reflection. It operates with one electrode biased to -150 V, the other two set to 150 V and a pulse length of 200 ns. This alters an ion's angle of entry into a mirror and causes it to steer into the wall of the drift tube, effectively eliminating any unwanted ion species. The addition of this mass selector is vital to keep the unambiguous mass range unambiguous.

Bibliography

[1] QR Ahmad et al. Measurement of day and night neutrino energy spectra at SNO and constraints on neutrino mixing parameters. *Physical Review Letters*, 89(1):011302, 2002.

[2] S Fukuda et al. Determination of solar neutrino oscillation parameters using 1496 days of Super-Kamiokande-I data. *Physics Letters B*, 539(3):179, 2002.

[3] Vernon Barger, Danny Marfatia, and Kerry Lewis Whisnant. *The physics of neutrinos*. Princeton University Press, 2012.

[4] J W F Valle. Neutrino physics overview. *Journal of Physics: Conference Series*, 53(1):473, 2006.

[5] J D Vergados, H Ejiri, and F Šimkovic. Theory of neutrinoless double beta decay. *Reports on Progress in Physics*, 75(10):106301, 2012.

[6] M Auger et al. The EXO-200 detector, part I: detector design and construction. *Journal of Instrumentation*, 7(05):P05010, 2012.

[7] J. Albert, ..., K. Murray, et al. Sensitivity and discovery potential of nEXO to neutrinoless double beta decay. *arXiv preprint arXiv:1710.05075*, 2017.

[8] GC Carlson et al. Half-lives of some short-lived mass-separated gaseous fission products and their daughters. *Nuclear Physics A*, 125(2):267, 1969.

[9] RN Wolf et al. On-line separation of short-lived nuclei by a multi-reflection time-of-flight device. *Nuclear Instruments and Methods in Physics Research Section A*, 686:82, 2012.

[10] Wolfgang Pauli. Dear radioactive ladies and gentlemen. *Physics Today*, 31:27, 1930.

[11] Fred L. Wilson. Fermi's Theory of Beta Decay. *American Journal of Physics*, 36(12):1150, 1968.

[12] C. L. Cowan, F. Reines, F. B. Harrison, H. W. Kruse, and A. D. McGuire. Detection of the free neutrino: a confirmation. *Science*, 124(3212):103, 1956.

[13] G. Danby et al. Observation of high-energy neutrino reactions and the existence of two kinds of neutrinos. *Physical Review Letters*, 9:36, 1962.

[14] M. L. Perl et al. Evidence for anomalous lepton production in $e^+ - e^-$ annihilation. *Physical Review Letters*, 35:1489, 1975.

[15] K Kodama et al. Observation of tau neutrino interactions. *Physics Letters B*, 504(3):218, 2001.

[16] Raymond Davis Jr, Don S Harmer, and Kenneth C Hoffman. Search for neutrinos from the sun. *Physical Review Letters*, 20(21):1205, 1968.

[17] Ziro Maki, Masami Nakagawa, and Shoichi Sakata. Remarks on the unified model of elementary particles. *Progress of Theoretical Physics*, 28(5):870, 1962.

[18] Jose Bernabeu. On the history of the PMNS Matrix... with today's perspective. *arXiv preprint arXiv:1312.7451*, 2013.

[19] SF King. Neutrino mass models: A road map. In *Journal of Physics: Conference Series*. IOP Publishing, 2008.

[20] Boris Kayser. Are neutrinos their own antiparticles? In *Journal of Physics: Conference Series*. IOP Publishing, 2009.

[21] Steven R Elliott and Petr Vogel. Double beta decay. *Annual Review of Nuclear and Particle Science*, 52(1):115, 2002.

[22] Samoil M Bilenky and ST Petcov. Massive neutrinos and neutrino oscillations. *Reviews of Modern Physics*, 59(3):671, 1987.

[23] HV Klapdor-Kleingrothaus, A Dietz, HL Harney, and IV Krivosheina. Evidence for neutrinoless double beta decay. *Modern Physics Letters A*, 16(37):2409, 2001.

[24] Samoil M Bilenky et al. Majorana neutrinos, neutrino mass spectrum, cp violation, and neutrinoless double beta decay: The three-neutrino mixing case. *Physical Review D*, 64(5):053010, 2001.

[25] Frank T. Avignone, Steven R. Elliott, and Jonathan Engel. Double beta decay, Majorana neutrinos, and neutrino mass. *Reviews of Modern Physics*, 80:481, 2008.

[26] Brian R Martin. *Nuclear and particle physics: an introduction*. John Wiley & Sons, 2006.

[27] K Zuber. Double beta decay. *Contemporary Physics*, 45(6):491, 2004.

[28] Ruben Saakyan. Two neutrino double beta decay. *Annual Review of Nuclear and Particle Science*, 63:503, 2013.

[29] D. Akimov et al. EXO: an advanced Enriched Xenon double-beta decay Observatory. *Nuclear Physics B - Proceedings Supplements*, 138(Supplement C):224, 2005.

[30] NIST. https://www.nist.gov/pml/xcom-photon-cross-sections-database , visited 2017-11.

[31] VN Solovov et al. Detection of scintillation light of liquid xenon with a LAAPD. *Nuclear Instruments and Methods in Physics Research Section A*, 488(3):572, 2002.

[32] JJ Gómez-Cadenas and Justo Martín-Albo. Phenomenology of neutrinoless double beta decay. *arXiv preprint arXiv:1502.00581*, 2015.

[33] J.J. Gómez-Cadenas et al. Sense and sensitivity of double beta decay experiments. *Journal of Cosmology and Astroparticle Physics*, 2011(06):007, 2011.

[34] JJ Gomez-Cadenas, J Martin-Albo, M Mezzetto, F Monrabal, and M Sorel. The search for neutrinoless double beta decay. *arXiv preprint arXiv:1109.5515*, 2011.

[35] E. Conti et al. Correlated fluctuations between luminescence and ionization in liquid Xenon. *Physical Review B*, 68:054201, 2003.

[36] J. B. Albert et al. Cosmogenic backgrounds to $0\nu\beta\beta$ in EXO-200. *Journal of Cosmology and Astroparticle Physics*, 2016(04):029, 2016.

[37] J. Albert et al. Improved measurement of the 2 $\nu\beta\beta$ half-life of ^{136}Xe with the EXO-200 detector. *Physical Review C*, 89(1):015502, 2014.

[38] Matthew Redshaw et al. Mass and double beta decay Q value of ^{136}Xe. *Physical Review Letters*, 98(5):053003, 2007.

[39] The EXO-200 Collaboration. Search for majorana neutrinos with the first two years of EXO-200 data. *Nature*, 510(7504):229, 2014. Article.

[40] Tadayoshi Doke and Kimiaki Masuda. Present status of liquid rare gas scintillation detectors and their new application to gamma-ray calorimeters. *Nuclear Instruments and Methods in Physics Research Section A*, 420(1):62, 1999.

[41] JB Albert et al. Search for neutrinoless double-beta decay with the upgraded EXO-200 detector. *Physical Review Letters*, 120(7):072701, 2018.

[42] Caio Licciardi. Latest EXO-200 results. TAUP conference, Sudbury, 2017.

[43] N. Ackerman et al. Observation of two-neutrino double-beta decay in ^{136}Xe with the EXO-200 detector. *Physical Review Letters*, 107:212501, 2011.

[44] J. Albert, ..., K. Murray, et al. Searches for double beta decay of ^{134}Xe with EXO-200. *Physical Review D*, 96:092001, 2017.

[45] M Jewell et al. Characterization of an ionization readout tile for nEXO. *Journal of Instrumentation*, 13(01):P01006, 2018.

[46] SNOLAB user's manual, revision 2. 2006.

[47] B. Mong et. al. Spectroscopy of Ba and Ba^+ deposits in solid Xenon for Barium tagging in nEXO. *Physical Review A*, 91:022505, 2015.

[48] K. Twelker et al. An apparatus to manipulate and identify individual Ba ions from bulk liquid Xe. *Review of Scientific Instruments*, 85(9):095114, 2014.

[49] B.J.P. Jones et al. Single molecule fluorescence imaging as a technique for Barium tagging in neutrinoless double beta decay. *Journal of Instrumentation*, 11(12):P12011, 2016.

[50] V Álvarez et al. Operation and first results of the NEXT-DEMO prototype using a silicon photomultiplier tracking array. *Journal of Instrumentation*, 8(09):P09011, 2013.

[51] A. D. McDonald et al. Demonstration of single-Barium-ion sensitivity for neutrinoless double-beta decay using single-molecule fluorescence imaging. *Physical Review Letters*, 120:132504, 2018.

[52] Thomas Brunner et al. An RF-only ion-funnel for extraction from high-pressure gases. *International Journal of Mass Spectrometry*, 379:110, 2015.

[53] T. Brunner et al. A setup for Ba-ion extraction from high pressure Xe gas for double-beta decay studies with EXO. *Nuclear Instruments and Methods in Physics Research Section B*, 317:473, 2013.

[54] M Green et al. Observation of single collisionally cooled trapped ions in a buffer gas. *Physical Review A*, 76(2):023404, 2007.

[55] Yang Lan. TRI-DN-17-34 A Linear Paul Trap for Identification of Barium Ions. Technical report, TRIUMF, 10 2017.

[56] Ronald J Onega and William W Pratt. Decay of ^{137}Xe. *Physical Review*, 136(2B):B365, 1964.

[57] E Browne and JK Tuli. Nuclear data sheets for A=137. *Nuclear Data Sheets*, 108(10):2173, 2007.

[58] Said F Mughabghab. *Atlas of Neutron Resonances: Resonance Parameters and Thermal Cross Sections. Z= 1-100*. Elsevier, 2006.

[59] Joshua Albert et al. Measurement of neutron capture on ^{136}Xe. *Physical Review C*, 94(3):034617, 2016.

[60] RB Firestone et al. Database of prompt gamma rays from slow neutron capture for elemental analysis. *Lawrence Berkeley National Laboratory*, 2004.

[61] Wolfgang R Plaß et al. Multiple-reflection time-of-flight mass spectrometry. *International Journal of Mass Spectrometry*, 349:134, 2013.

[62] Hermann Wollnik. *Optics of charged particles*. Elsevier, 2012.

[63] Mikhail Yavor. Chapter 8 time-of-flight mass analyzers. In *Optics of Charged Particle Analyzers*, volume 157 of *Advances in Imaging and Electron Physics*, page 283. Elsevier, 2009.

[64] T Kalvas. Beam extraction and transport. *arXiv preprint arXiv:1401.3951*, 2014.

[65] Friedrich Hinterberger. Ion optics with electrostatic lenses. 2006.

[66] T Dickel et al. A high-performance multiple-reflection time-of-flight mass spectrometer and isobar separator for the research with exotic nuclei. *Nuclear Instruments and Methods in Physics Research Section A*, 777:172, 2015.

[67] Christian Jesch. *The multiple-reflection time-of-flight isobar separator for TITAN and direct mass measurements at the FRS Ion Catcher*. PhD thesis, Universitätsbibliothek Giessen, 2016.

[68] Klaus Floettmann. Some basic features of the beam emittance. *Physical Review Special Topics-Accelerators and Beams*, 6(3):034202, 2003.

[69] D. Ioanoviciu. The application of ion optics in time-of-flight mass spectrometry. *International Journal of Mass Spectrometry and Ion Processes*, 131(Supplement C):43, 1994.

[70] Timo Dickel et al. Dynamical time focus shift in multiple-reflection time-of-flight mass spectrometers. *International Journal of Mass Spectrometry*, 412(Supplement C):1, 2017.

[71] AV Karpov et al. Genetic algorithm for voltage optimization of gridless ion mirror. *Physics Procedia*, 72:236, 2015.

[72] D. Manura and D. Dahl. *SIMION v8.1*. Scientific Instrument Services Inc., 2012.

[73] Christian Jesch et al. The MR-TOF-MS isobar separator for the TITAN facility at TRIUMF. *Hyperfine Interactions*, 235(1):97, 2015.

Appendix A

Drawings

A.1 Analyzer

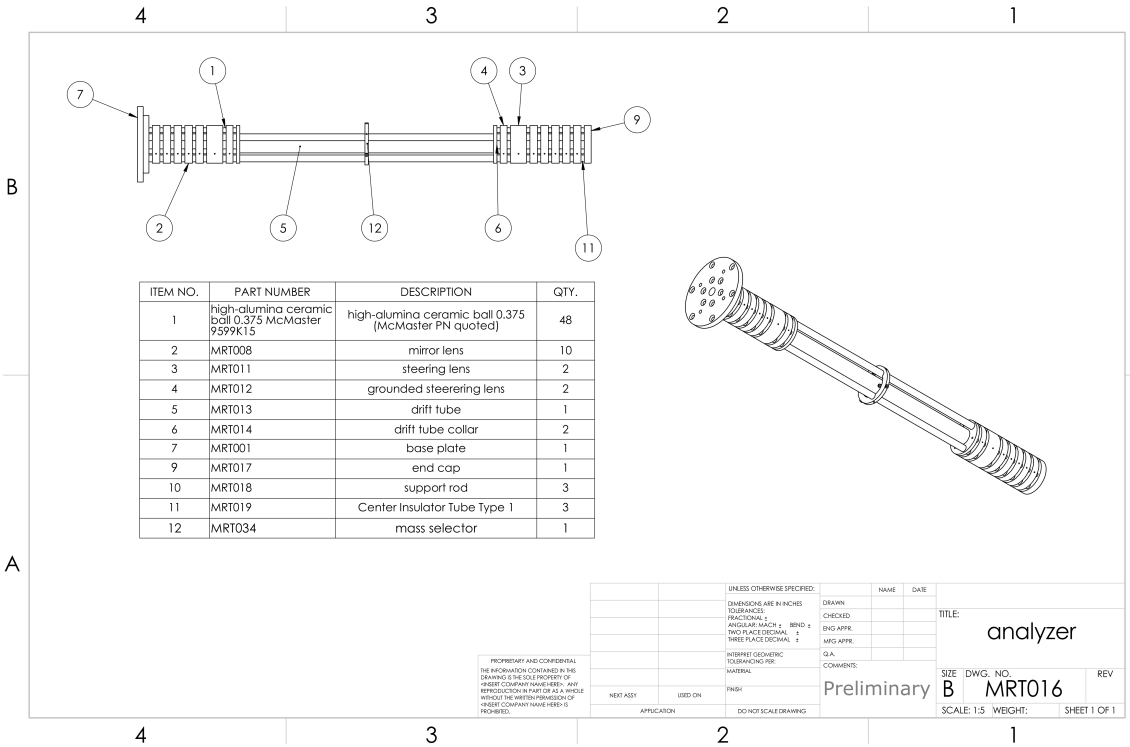

ITEM NO.	PART NUMBER	DESCRIPTION	QTY.
1	high-alumina ceramic ball 0.375 McMaster 9599K15	high-alumina ceramic ball 0.375 (McMaster PN quoted)	48
2	MRT008	mirror lens	10
3	MRT011	steering lens	2
4	MRT012	grounded steerering lens	2
5	MRT013	drift tube	1
6	MRT014	drift tube collar	2
7	MRT001	base plate	1
9	MRT017	end cap	1
10	MRT018	support rod	3
11	MRT019	Center Insulator Tube Type 1	3
12	MRT034	mass selector	1

UNLESS OTHERWISE SPECIFIED:
DIMENSIONS ARE IN INCHES
TOLERANCES:
FRACTIONAL ±
ANGULAR: MACH ± BEND ±
TWO PLACE DECIMAL ±
THREE PLACE DECIMAL ±
INTERPRET GEOMETRIC TOLERANCING PER:
MATERIAL
FINISH
DO NOT SCALE DRAWING
NAME DATE
DRAWN
CHECKED
ENG APPR.
MFG APPR.
Q.A.
COMMENTS:
Preliminary
TITLE: analyzer
SIZE B DWG. NO. MRT016 REV
SCALE: 1:5 WEIGHT: SHEET 1 OF 1

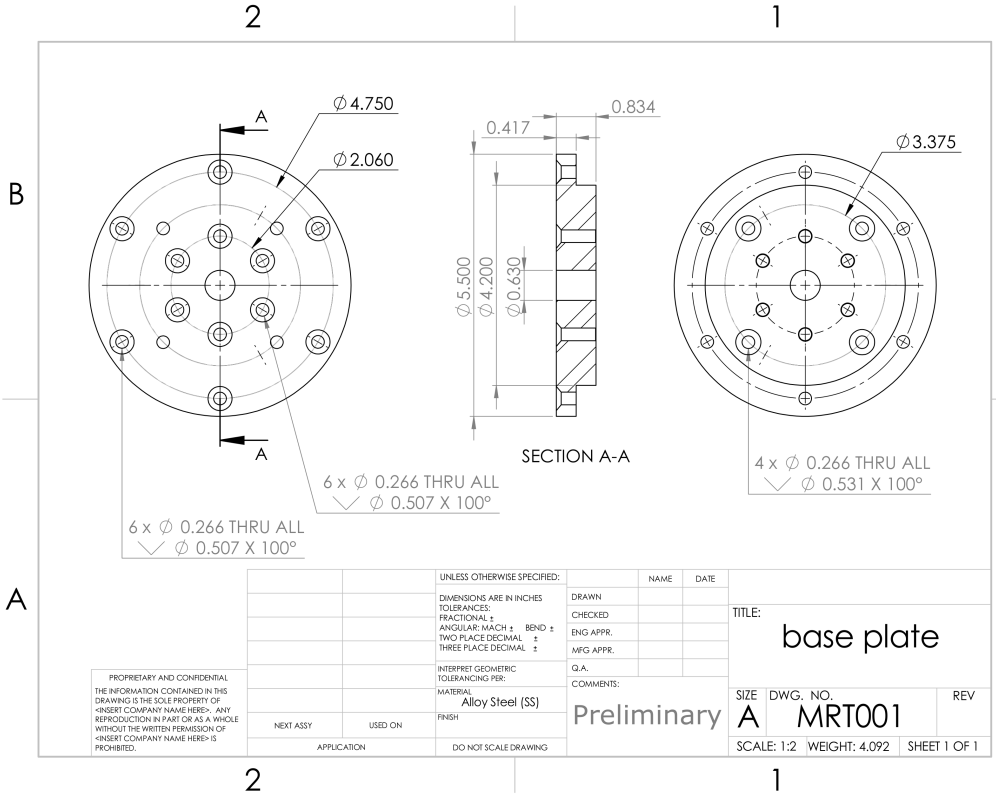
2
1
B
A
∅4.750
∅2.060
A
A
0.417
0.834
∅5.500
∅4.200
∅0.630
SECTION A-A
∅3.375
6 x ∅ 0.266 THRU ALL
∅ 0.507 X 100°
6 x ∅ 0.266 THRU ALL
∅ 0.507 X 100°
4 x ∅ 0.266 THRU ALL
∅ 0.531 X 100°
UNLESS OTHERWISE SPECIFIED:
DIMENSIONS ARE IN INCHES
TOLERANCES:
FRACTIONAL ±
ANGULAR: MACH ± BEND ±
TWO PLACE DECIMAL ±
THREE PLACE DECIMAL ±
INTERPRET GEOMETRIC TOLERANCING PER:
MATERIAL
Alloy Steel (SS)
FINISH
NEXT ASSY
USED ON
APPLICATION
DO NOT SCALE DRAWING
NAME
DATE
DRAWN
CHECKED
ENG APPR.
MFG APPR.
Q.A.
COMMENTS:
Preliminary
TITLE:
base plate
SIZE
A
DWG. NO.
MRT001
REV
SCALE: 1:2
WEIGHT: 4.092
SHEET 1 OF 1
PROPRIETARY AND CONFIDENTIAL
THE INFORMATION CONTAINED IN THIS DRAWING IS THE SOLE PROPERTY OF <INSERT COMPANY NAME HERE>. ANY REPRODUCTION IN PART OR AS A WHOLE WITHOUT THE WRITTEN PERMISSION OF <INSERT COMPANY NAME HERE> IS PROHIBITED.

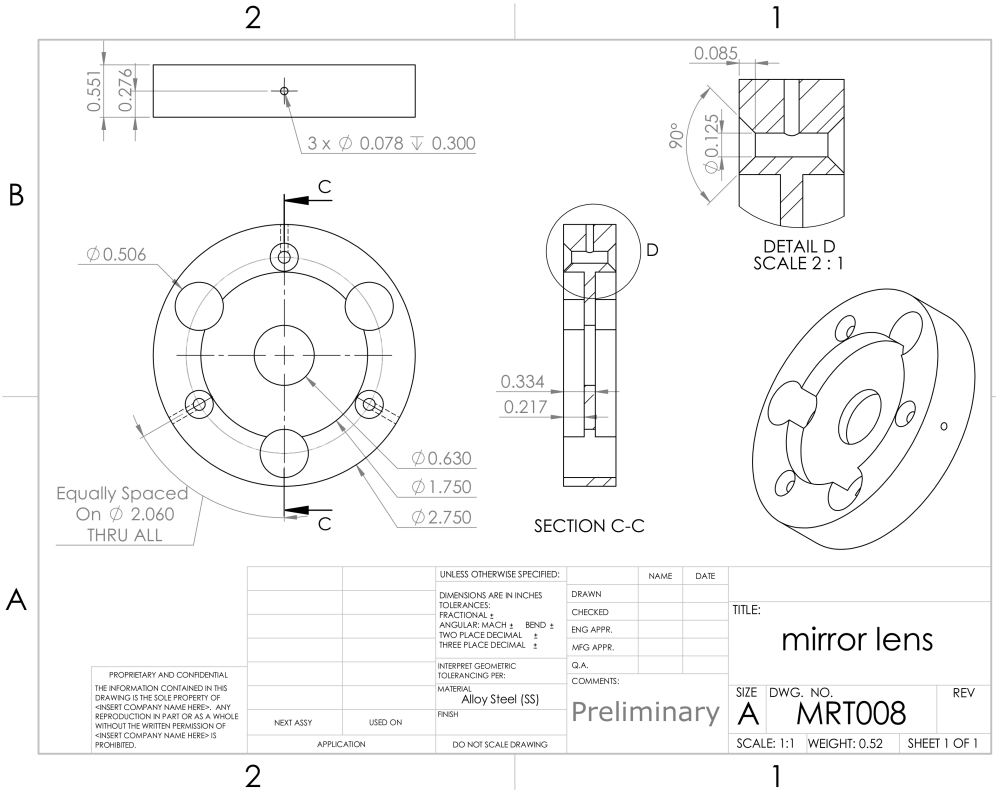
2
1
B
A
0.551
0.276
3 x ∅ 0.078 ↧ 0.300
0.085
90°
∅0.125
DETAIL D
SCALE 2 : 1
C
∅0.506
D
0.334
0.217
∅0.630
∅1.750
∅2.750
Equally Spaced
On ∅ 2.060
THRU ALL
C
SECTION C-C
UNLESS OTHERWISE SPECIFIED:
DIMENSIONS ARE IN INCHES
TOLERANCES:
FRACTIONAL ±
ANGULAR: MACH ± BEND ±
TWO PLACE DECIMAL ±
THREE PLACE DECIMAL ±
INTERPRET GEOMETRIC TOLERANCING PER:
MATERIAL
Alloy Steel (SS)
FINISH
NEXT ASSY
USED ON
APPLICATION
DO NOT SCALE DRAWING
NAME
DATE
DRAWN
CHECKED
ENG APPR.
MFG APPR.
Q.A.
COMMENTS:
Preliminary
TITLE:
mirror lens
SIZE
A
DWG. NO.
MRT008
REV
SCALE: 1:1
WEIGHT: 0.52
SHEET 1 OF 1
PROPRIETARY AND CONFIDENTIAL
THE INFORMATION CONTAINED IN THIS DRAWING IS THE SOLE PROPERTY OF <INSERT COMPANY NAME HERE>. ANY REPRODUCTION IN PART OR AS A WHOLE WITHOUT THE WRITTEN PERMISSION OF <INSERT COMPANY NAME HERE> IS PROHIBITED.

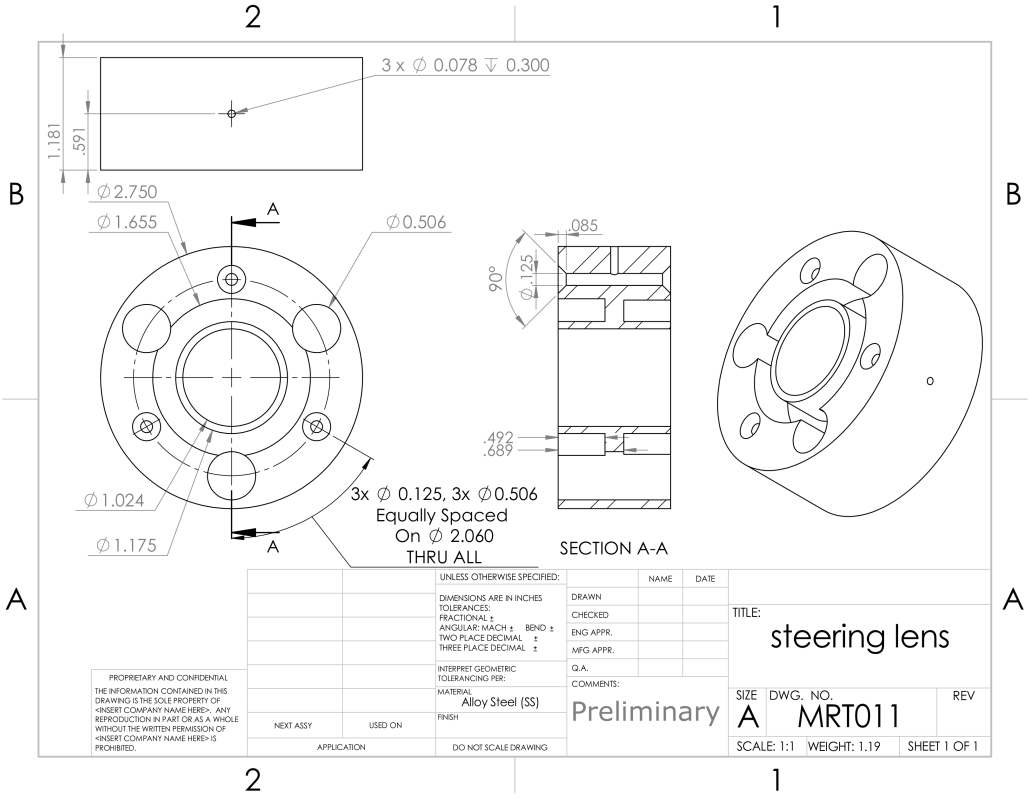
3 x ∅ 0.078 ↧ 0.300
1.181
.591
∅2.750
∅1.655
∅0.506
.085
90°
∅.125
.492
.689
∅1.024
∅1.175
3x ∅ 0.125, 3x ∅0.506
Equally Spaced
On ∅ 2.060
THRU ALL
SECTION A-A
UNLESS OTHERWISE SPECIFIED:
DIMENSIONS ARE IN INCHES
TOLERANCES:
FRACTIONAL ±
ANGULAR: MACH ± BEND ±
TWO PLACE DECIMAL ±
THREE PLACE DECIMAL ±
INTERPRET GEOMETRIC TOLERANCING PER:
MATERIAL
Alloy Steel (SS)
FINISH
NEXT ASSY
USED ON
APPLICATION
DO NOT SCALE DRAWING
NAME
DATE
DRAWN
CHECKED
ENG APPR.
MFG APPR.
Q.A.
COMMENTS:
Preliminary
PROPRIETARY AND CONFIDENTIAL
THE INFORMATION CONTAINED IN THIS DRAWING IS THE SOLE PROPERTY OF <INSERT COMPANY NAME HERE>. ANY REPRODUCTION IN PART OR AS A WHOLE WITHOUT THE WRITTEN PERMISSION OF <INSERT COMPANY NAME HERE> IS PROHIBITED.
TITLE:
steering lens
SIZE
A
DWG. NO.
MRT011
REV
SCALE: 1:1
WEIGHT: 1.19
SHEET 1 OF 1

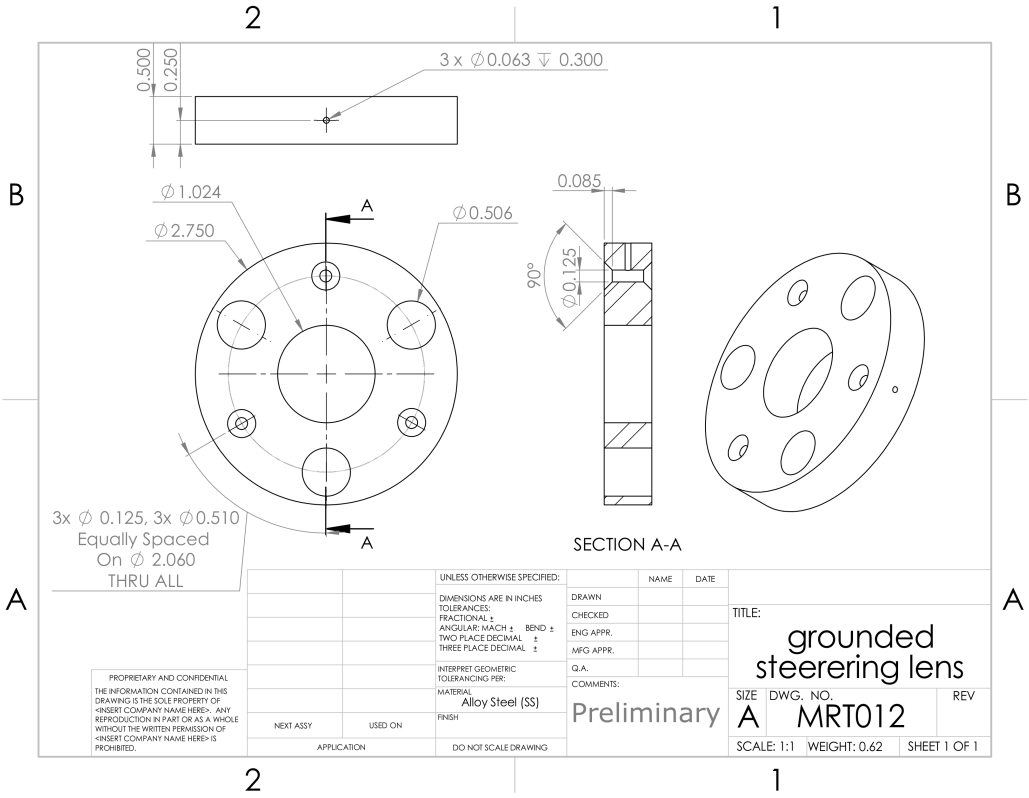
3 x ∅0.063 ↧ 0.300
0.500
0.250
∅1.024
∅2.750
∅0.506
0.085
90°
∅0.125
3x ∅ 0.125, 3x ∅0.510
Equally Spaced
On ∅ 2.060
THRU ALL
SECTION A-A
UNLESS OTHERWISE SPECIFIED:
DIMENSIONS ARE IN INCHES
TOLERANCES:
FRACTIONAL ±
ANGULAR: MACH ± BEND ±
TWO PLACE DECIMAL ±
THREE PLACE DECIMAL ±
INTERPRET GEOMETRIC TOLERANCING PER:
MATERIAL
Alloy Steel (SS)
FINISH
NEXT ASSY
USED ON
APPLICATION
DO NOT SCALE DRAWING
NAME
DATE
DRAWN
CHECKED
ENG APPR.
MFG APPR.
Q.A.
COMMENTS:
Preliminary
PROPRIETARY AND CONFIDENTIAL
THE INFORMATION CONTAINED IN THIS DRAWING IS THE SOLE PROPERTY OF <INSERT COMPANY NAME HERE>. ANY REPRODUCTION IN PART OR AS A WHOLE WITHOUT THE WRITTEN PERMISSION OF <INSERT COMPANY NAME HERE> IS PROHIBITED.
TITLE:
grounded steerering lens
SIZE
A
DWG. NO.
MRT012
REV
SCALE: 1:1
WEIGHT: 0.62
SHEET 1 OF 1

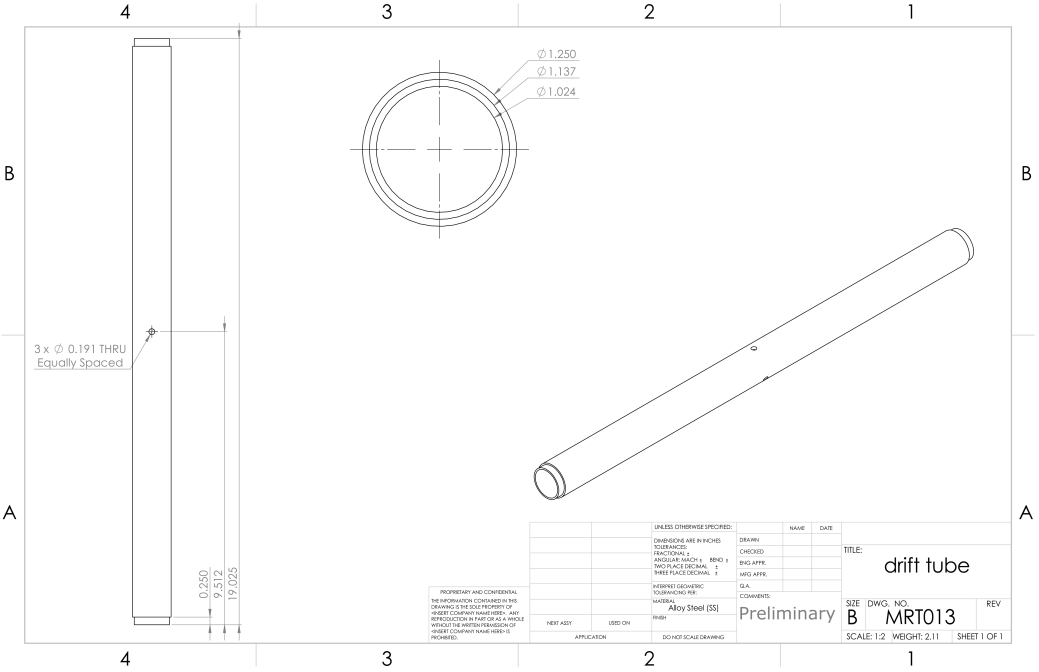
∅1.250
∅1.137
∅1.024
3 x ∅ 0.191 THRU
Equally Spaced
0.250
9.512
19.025
UNLESS OTHERWISE SPECIFIED:
DIMENSIONS ARE IN INCHES
TOLERANCES:
FRACTIONAL ±
ANGULAR: MACH ± BEND ±
TWO PLACE DECIMAL ±
THREE PLACE DECIMAL ±
INTERPRET GEOMETRIC TOLERANCING PER:
MATERIAL
Alloy Steel (SS)
FINISH
NEXT ASSY
USED ON
APPLICATION
DO NOT SCALE DRAWING
NAME
DATE
DRAWN
CHECKED
ENG APPR.
MFG APPR.
Q.A.
COMMENTS:
Preliminary
PROPRIETARY AND CONFIDENTIAL
THE INFORMATION CONTAINED IN THIS DRAWING IS THE SOLE PROPERTY OF <INSERT COMPANY NAME HERE>. ANY REPRODUCTION IN PART OR AS A WHOLE WITHOUT THE WRITTEN PERMISSION OF <INSERT COMPANY NAME HERE> IS PROHIBITED.
TITLE:
drift tube
SIZE
B
DWG. NO.
MRT013
REV
SCALE: 1:2
WEIGHT: 2.11
SHEET 1 OF 1

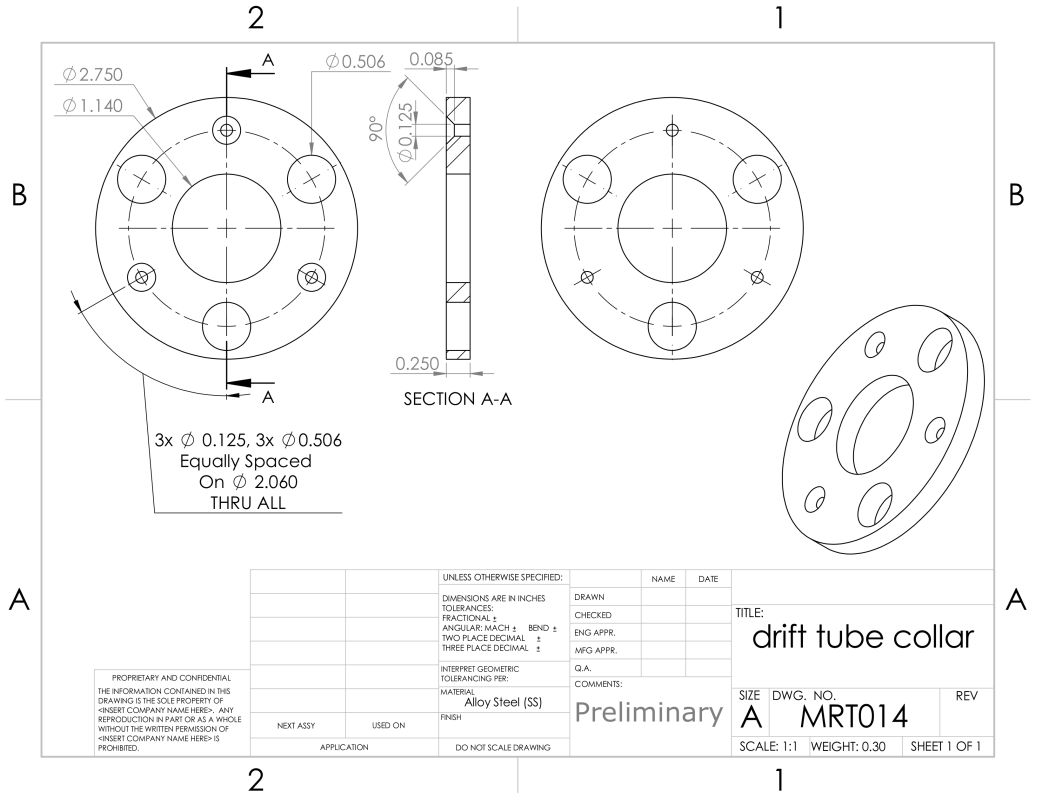
∅2.750
∅1.140
∅0.506
0.085
90°
∅0.125
0.250
SECTION A-A
3x ∅ 0.125, 3x ∅0.506
Equally Spaced
On ∅ 2.060
THRU ALL
UNLESS OTHERWISE SPECIFIED:
DIMENSIONS ARE IN INCHES
TOLERANCES:
FRACTIONAL ±
ANGULAR: MACH ± BEND ±
TWO PLACE DECIMAL ±
THREE PLACE DECIMAL ±
INTERPRET GEOMETRIC TOLERANCING PER:
MATERIAL
Alloy Steel (SS)
FINISH
NEXT ASSY
USED ON
APPLICATION
DO NOT SCALE DRAWING
NAME
DATE
DRAWN
CHECKED
ENG APPR.
MFG APPR.
Q.A.
COMMENTS:
Preliminary
PROPRIETARY AND CONFIDENTIAL
THE INFORMATION CONTAINED IN THIS DRAWING IS THE SOLE PROPERTY OF <INSERT COMPANY NAME HERE>. ANY REPRODUCTION IN PART OR AS A WHOLE WITHOUT THE WRITTEN PERMISSION OF <INSERT COMPANY NAME HERE> IS PROHIBITED.
TITLE:
drift tube collar
SIZE
A
DWG. NO.
MRT014
REV
SCALE: 1:1
WEIGHT: 0.30
SHEET 1 OF 1

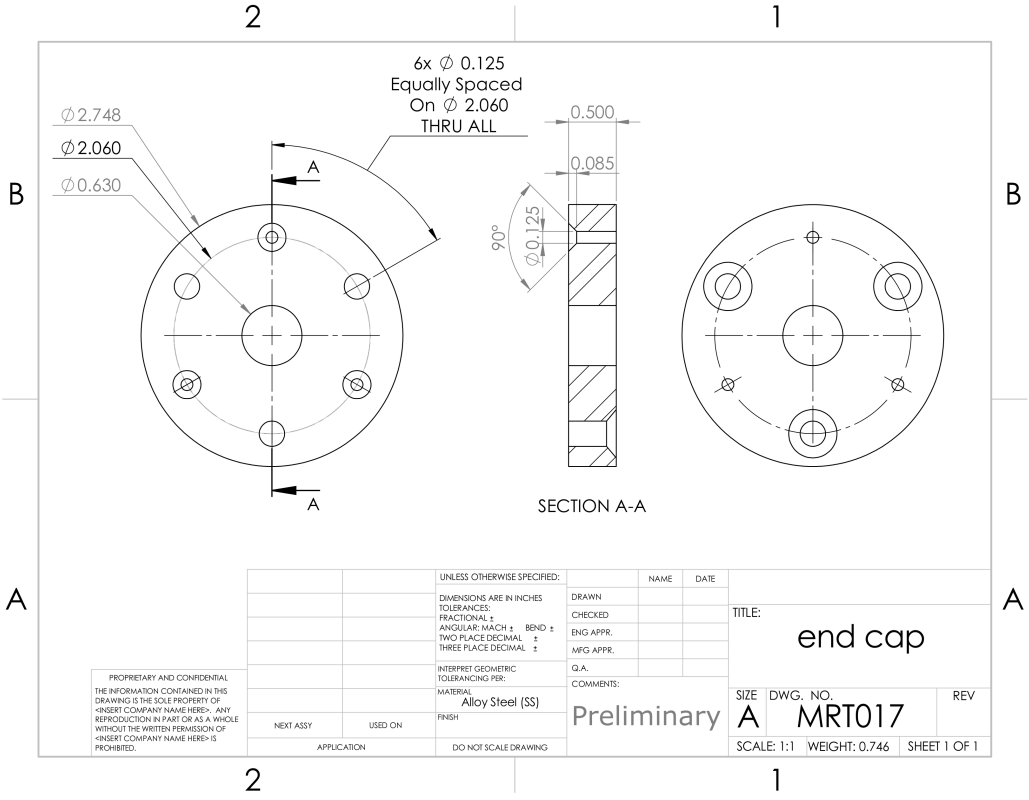
6x ∅ 0.125
Equally Spaced
On ∅ 2.060
THRU ALL
∅2.748
∅2.060
∅0.630
A
A
0.500
0.085
90°
∅0.125
SECTION A-A
UNLESS OTHERWISE SPECIFIED:
DIMENSIONS ARE IN INCHES
TOLERANCES:
FRACTIONAL ±
ANGULAR: MACH ± BEND ±
TWO PLACE DECIMAL ±
THREE PLACE DECIMAL ±
INTERPRET GEOMETRIC TOLERANCING PER:
MATERIAL
Alloy Steel (SS)
FINISH
NEXT ASSY
USED ON
APPLICATION
DO NOT SCALE DRAWING
NAME
DATE
DRAWN
CHECKED
ENG APPR.
MFG APPR.
Q.A.
COMMENTS:
Preliminary
PROPRIETARY AND CONFIDENTIAL
THE INFORMATION CONTAINED IN THIS DRAWING IS THE SOLE PROPERTY OF <INSERT COMPANY NAME HERE>. ANY REPRODUCTION IN PART OR AS A WHOLE WITHOUT THE WRITTEN PERMISSION OF <INSERT COMPANY NAME HERE> IS PROHIBITED.
TITLE:
end cap
SIZE
A
DWG. NO.
MRT017
REV
SCALE: 1:1
WEIGHT: 0.746
SHEET 1 OF 1

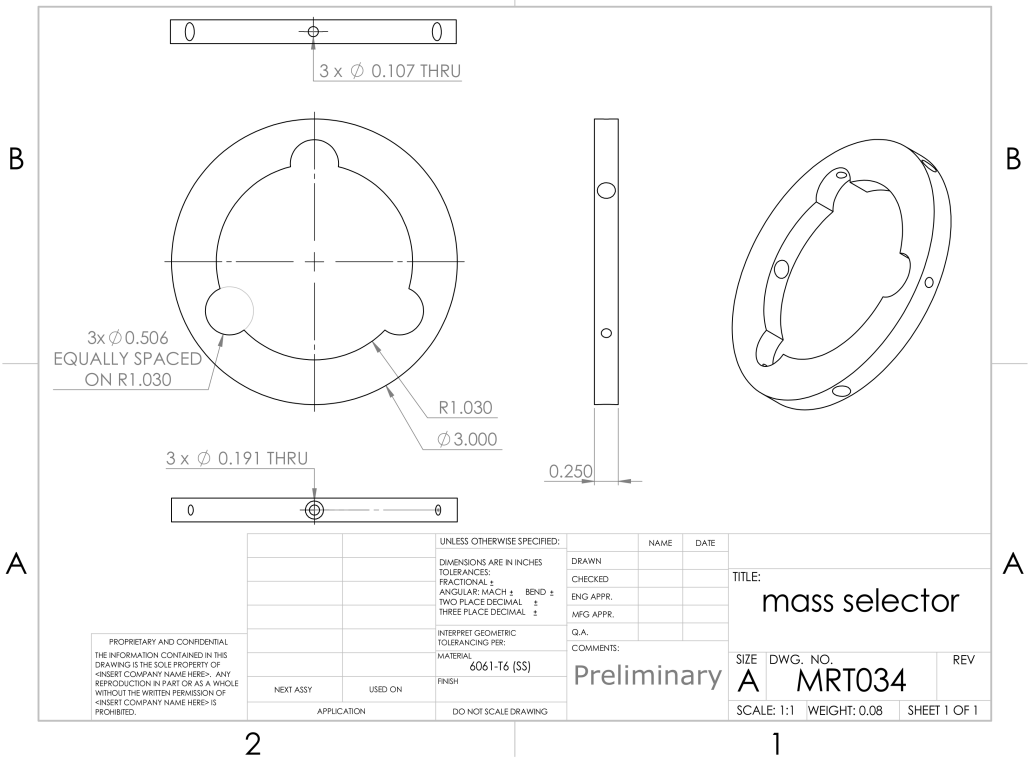
3 x ∅ 0.107 THRU
3x∅0.506
EQUALLY SPACED
ON R1.030
R1.030
∅3.000
3 x ∅ 0.191 THRU
0.250
UNLESS OTHERWISE SPECIFIED:
DIMENSIONS ARE IN INCHES
TOLERANCES:
FRACTIONAL ±
ANGULAR: MACH ± BEND ±
TWO PLACE DECIMAL ±
THREE PLACE DECIMAL ±
INTERPRET GEOMETRIC TOLERANCING PER:
MATERIAL
6061-T6 (SS)
FINISH
NEXT ASSY
USED ON
APPLICATION
DO NOT SCALE DRAWING
NAME
DATE
DRAWN
CHECKED
ENG APPR.
MFG APPR.
Q.A.
COMMENTS:
Preliminary
PROPRIETARY AND CONFIDENTIAL
THE INFORMATION CONTAINED IN THIS DRAWING IS THE SOLE PROPERTY OF <INSERT COMPANY NAME HERE>. ANY REPRODUCTION IN PART OR AS A WHOLE WITHOUT THE WRITTEN PERMISSION OF <INSERT COMPANY NAME HERE> IS PROHIBITED.
TITLE:
mass selector
SIZE
A
DWG. NO.
MRT034
REV
SCALE: 1:1
WEIGHT: 0.08
SHEET 1 OF 1

A.2 Ion Optics

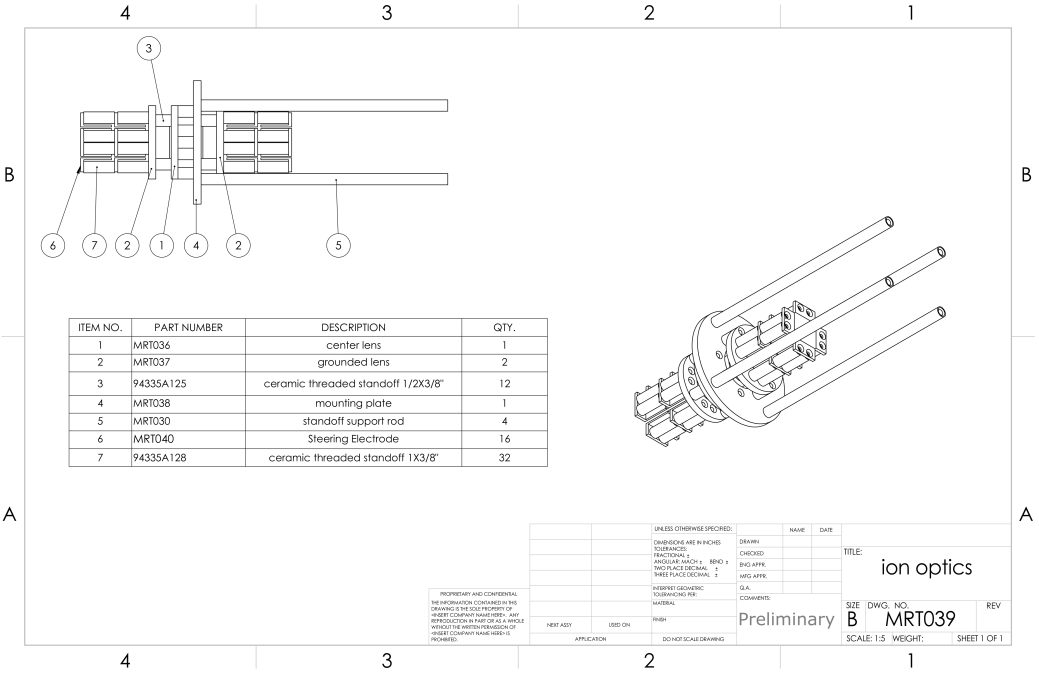

ITEM NO.	PART NUMBER	DESCRIPTION	QTY.
1	MRT036	center lens	1
2	MRT037	grounded lens	2
3	94335A125	ceramic threaded standoff 1/2X3/8"	12
4	MRT038	mounting plate	1
5	MRT030	standoff support rod	4
6	MRT040	Steering Electrode	16
7	94335A128	ceramic threaded standoff 1X3/8"	32

UNLESS OTHERWISE SPECIFIED:
DIMENSIONS ARE IN INCHES
TOLERANCES:
FRACTIONAL ±
ANGULAR: MACH ± BEND ±
TWO PLACE DECIMAL ±
THREE PLACE DECIMAL ±
INTERPRET GEOMETRIC TOLERANCING PER:
MATERIAL
FINISH
NEXT ASSY | USED ON
APPLICATION | DO NOT SCALE DRAWING

NAME | DATE
DRAWN
CHECKED
ENG APPR.
MFG APPR.
Q.A.
COMMENTS:
Preliminary

TITLE: ion optics
SIZE B | DWG. NO. MRT039 | REV
SCALE: 1:5 | WEIGHT: | SHEET 1 OF 1

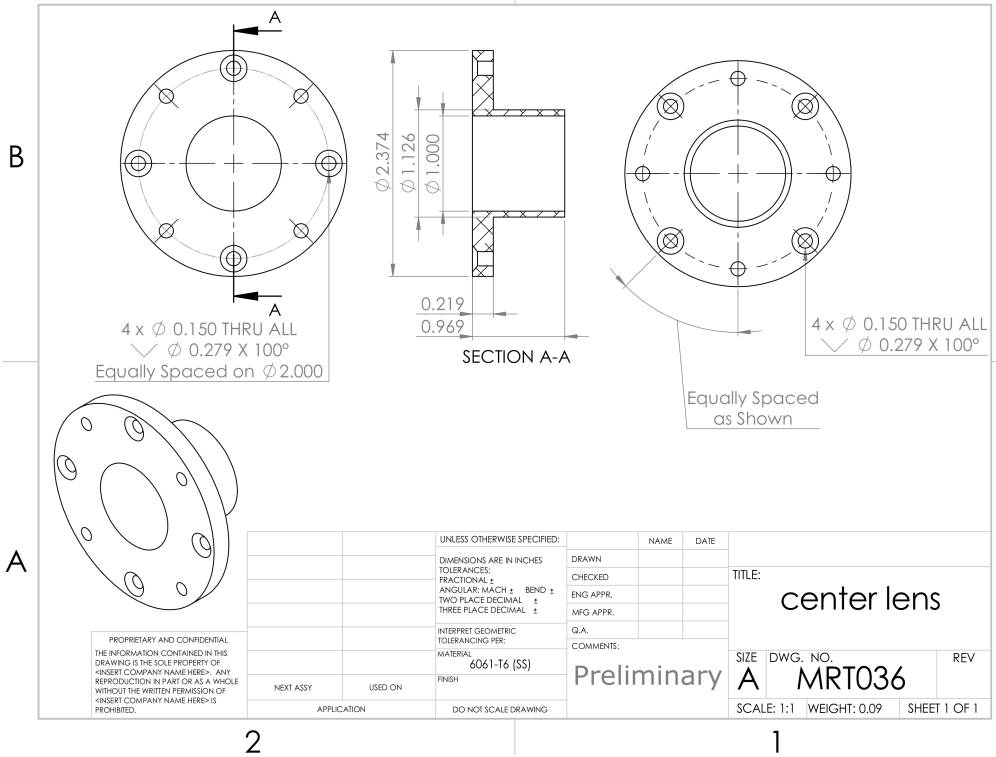

UNLESS OTHERWISE SPECIFIED:
DIMENSIONS ARE IN INCHES
TOLERANCES:
FRACTIONAL ±
ANGULAR: MACH ± BEND ±
TWO PLACE DECIMAL ±
THREE PLACE DECIMAL ±
INTERPRET GEOMETRIC TOLERANCING PER:
MATERIAL 6061-T6 (SS)
FINISH
NEXT ASSY | USED ON
APPLICATION | DO NOT SCALE DRAWING

NAME | DATE
DRAWN
CHECKED
ENG APPR.
MFG APPR.
Q.A.
COMMENTS:
Preliminary

TITLE: center lens
SIZE A | DWG. NO. MRT036 | REV
SCALE: 1:1 | WEIGHT: 0.09 | SHEET 1 OF 1

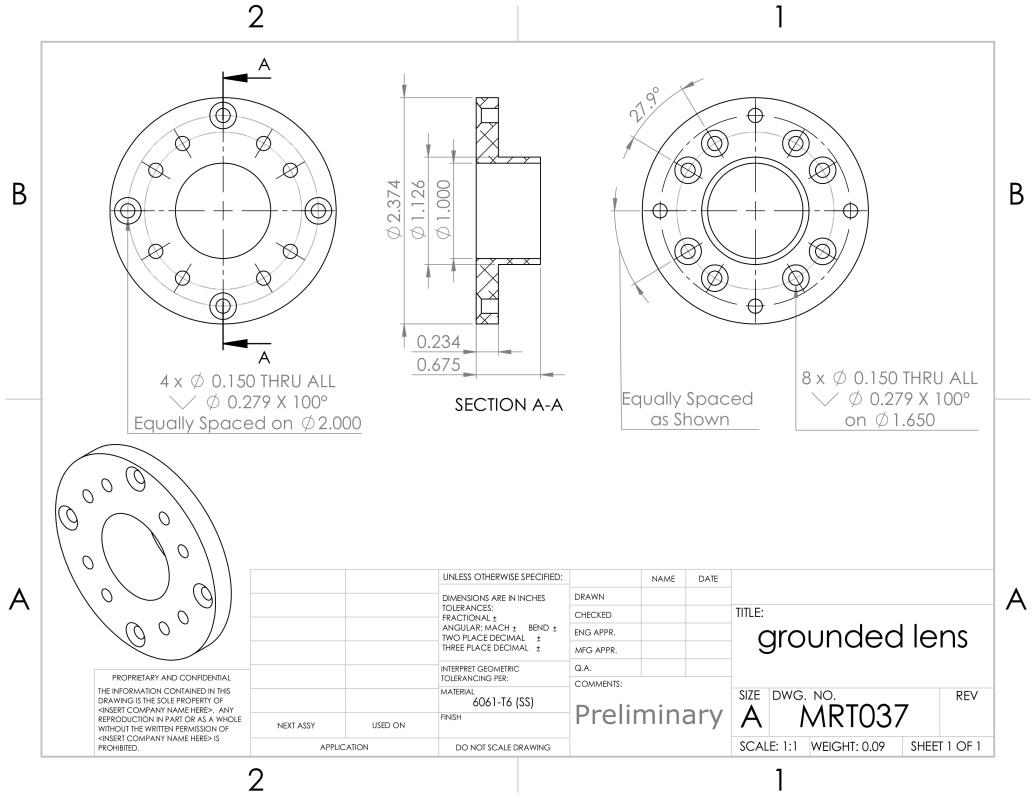
A
A
4 x ∅ 0.150 THRU ALL
∅ 0.279 X 100°
Equally Spaced on ∅2.000
∅2.374
∅1.126
∅1.000
0.234
0.675
SECTION A-A
27.9°
Equally Spaced
as Shown
8 x ∅ 0.150 THRU ALL
∅ 0.279 X 100°
on ∅1.650
PROPRIETARY AND CONFIDENTIAL
THE INFORMATION CONTAINED IN THIS DRAWING IS THE SOLE PROPERTY OF <INSERT COMPANY NAME HERE>. ANY REPRODUCTION IN PART OR AS A WHOLE WITHOUT THE WRITTEN PERMISSION OF <INSERT COMPANY NAME HERE> IS PROHIBITED.
UNLESS OTHERWISE SPECIFIED:
DIMENSIONS ARE IN INCHES
TOLERANCES:
FRACTIONAL ±
ANGULAR: MACH ± BEND ±
TWO PLACE DECIMAL ±
THREE PLACE DECIMAL ±
INTERPRET GEOMETRIC TOLERANCING PER:
MATERIAL
6061-T6 (SS)
FINISH
NEXT ASSY
USED ON
APPLICATION
DO NOT SCALE DRAWING
NAME
DATE
DRAWN
CHECKED
ENG APPR.
MFG APPR.
Q.A.
COMMENTS:
Preliminary
TITLE:
grounded lens
SIZE
A
DWG. NO.
MRT037
REV
SCALE: 1:1
WEIGHT: 0.09
SHEET 1 OF 1

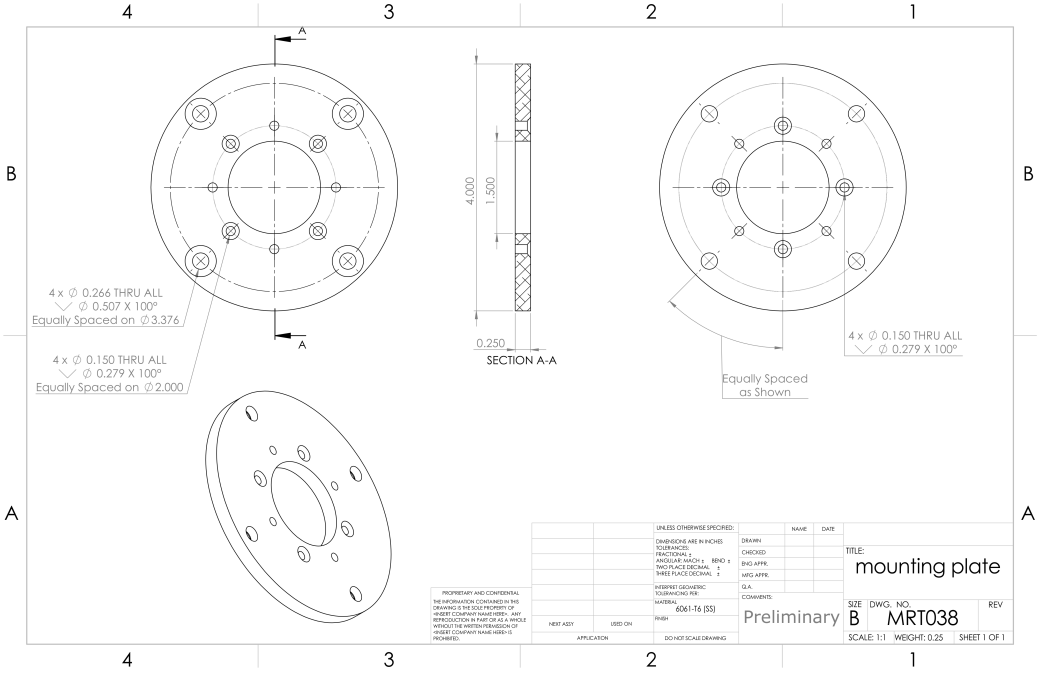
A
A
4 x ∅ 0.266 THRU ALL
∅ 0.507 X 100°
Equally Spaced on ∅3.376
4 x ∅ 0.150 THRU ALL
∅ 0.279 X 100°
Equally Spaced on ∅2.000
4.000
1.500
0.250
SECTION A-A
Equally Spaced
as Shown
4 x ∅ 0.150 THRU ALL
∅ 0.279 X 100°
PROPRIETARY AND CONFIDENTIAL
THE INFORMATION CONTAINED IN THIS DRAWING IS THE SOLE PROPERTY OF <INSERT COMPANY NAME HERE>. ANY REPRODUCTION IN PART OR AS A WHOLE WITHOUT THE WRITTEN PERMISSION OF <INSERT COMPANY NAME HERE> IS PROHIBITED.
UNLESS OTHERWISE SPECIFIED:
DIMENSIONS ARE IN INCHES
TOLERANCES:
FRACTIONAL ±
ANGULAR: MACH ± BEND ±
TWO PLACE DECIMAL ±
THREE PLACE DECIMAL ±
INTERPRET GEOMETRIC TOLERANCING PER:
MATERIAL
6061-T6 (SS)
FINISH
NEXT ASSY
USED ON
APPLICATION
DO NOT SCALE DRAWING
NAME
DATE
DRAWN
CHECKED
ENG APPR.
MFG APPR.
Q.A.
COMMENTS:
Preliminary
TITLE:
mounting plate
SIZE
B
DWG. NO.
MRT038
REV
SCALE: 1:1
WEIGHT: 0.25
SHEET 1 OF 1

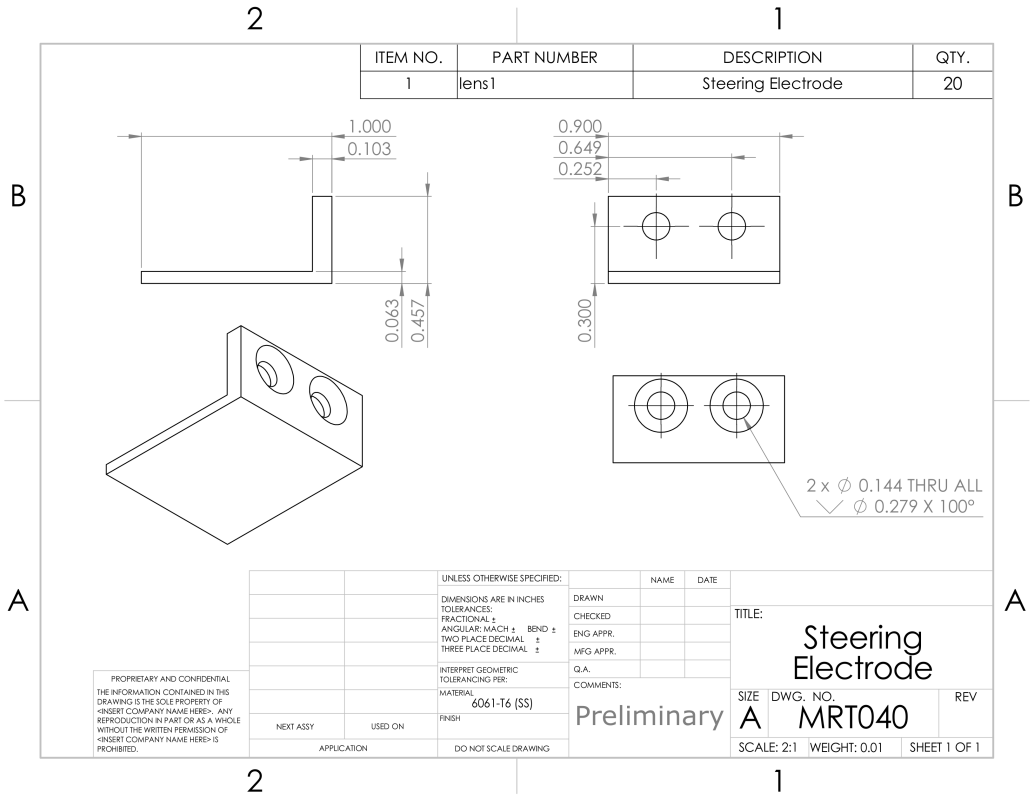
2
1
ITEM NO. PART NUMBER DESCRIPTION QTY.
1 lens1 Steering Electrode 20
1.000
0.103
0.063
0.457
0.900
0.649
0.252
0.300
2 x ∅ 0.144 THRU ALL
∅ 0.279 X 100°
B
A
UNLESS OTHERWISE SPECIFIED:
DIMENSIONS ARE IN INCHES
TOLERANCES:
FRACTIONAL ±
ANGULAR: MACH ± BEND ±
TWO PLACE DECIMAL ±
THREE PLACE DECIMAL ±
INTERPRET GEOMETRIC TOLERANCING PER:
MATERIAL 6061-T6 (SS)
FINISH
NEXT ASSY USED ON
APPLICATION DO NOT SCALE DRAWING
NAME DATE
DRAWN
CHECKED
ENG APPR.
MFG APPR.
Q.A.
COMMENTS:
Preliminary
TITLE:
Steering Electrode
SIZE A DWG. NO. MRT040 REV
SCALE: 2:1 WEIGHT: 0.01 SHEET 1 OF 1
PROPRIETARY AND CONFIDENTIAL
THE INFORMATION CONTAINED IN THIS DRAWING IS THE SOLE PROPERTY OF <INSERT COMPANY NAME HERE>. ANY REPRODUCTION IN PART OR AS A WHOLE WITHOUT THE WRITTEN PERMISSION OF <INSERT COMPANY NAME HERE> IS PROHIBITED.